The Rotating Drum Heat Exchanger for Latent Heat Thermal Energy Storage

A thesis accepted by the Faculty of Energy-, Process- and Bio-Engineering of the University of Stuttgart to fulfill the requirements for the degree of Doctor of Engineering Sciences (Dr.-Ing.)

by

Jonas Tombrink

born in Waldshut-Tiengen

Main examiner: Prof. Dr. rer. nat. habil. André Thess

Co-examiner: Prof. Dr. Ruth Herrero-Martín

Chairperson: Prof. Dr. techn. Günter Scheffknecht

Date of oral exam: 21st March 2023

Institute for Building Energetics, Thermotechnology and Energy Storage
(IGTE) at the University of Stuttgart

2023

Declaration

I hereby certify that this dissertation is entirely my own work except where otherwise indicated. Passages and ideas from other sources have been clearly indicated.

Stuttgart, ________________ ____________________________

Jonas Tombrink

Preface and Acknowledgement

Initially I would like to express my sincere thanks to Prof. André Thess, for the supervision of this thesis, the scientific discussions and also for encouraging me to keep a commercialization of the heat exchanger in mind. Special thank also go to Prof. Ruth Herrero-Martín, who agreed to be the co-examiner, and Prof. Günter Scheffknecht, who took over the chair of the examination. A special thanks goes to my direct supervisor Dan Bauer, not only for the idea of the Rotating Drum Heat Exchanger and the provision of the topic, but also for guiding me through the challenging task of researching and writing scientific publications. He protected me from too much administrative work so I could focus on the scientific work.

My time as a PhD-candidate at the DLR was always enriched by a motivating and friendly atmosphere with my colleagues. There has always been a well-balanced mix of in-depth scientific discussions, but also motivating and friendly conversations. Sometimes we even philosophized into the night. The numerous weeks we had to spend in the home office due to the Covid-19 pandemic showed me how much I valued the daily contact in the office. Also, the collaboration with students was always an enrichment of the daily work and also the scientific findings. Special thanks go to Florian Geiger, Henning Budde, Erik Jung, Leonhard Kölz, Simon Gronau and also Larissa Dietz, who later become a supporting member of our group. Special thanks go to Michael Fiss and Manuel Moosmann for solving various minor and major technical issues related to the experimental test rig. I would like thank my former colleague Henning Jockenhöfer not only for introducing me to the topic, but also for his first considerations and also preliminary experimental work on the Rotating Drum Heat Exchanger. Many thanks also to my office colleague Andrea Gutierrez for the friendly atmosphere, for the inspiring discussions and also for enduring my loud swearing at challenging times during simulation work. Furthermore, I would like to thank all further members and also former members of the whole TSP group, namely Maike Johnson, Wolf-Dieter Steinmann, Thilo Weller and Julian Vogel. It has always been a nice collaboration, inspiring discussions and I could always rely on you.

Last but not least, I would like to thank all my friends, not only for their motivating support, but also for the distraction from daily grind, which is still mystical in parts for some of them. Special thanks go to my parents Helga and Uwe and my brothers Tobias and Fabian, who not only never got tired of asking about the progress of this thesis, but also supported me and had confidence in me.

Contents

Abstract

Since the industrial revolution, the evaporation of water has been the most common method for providing industrially usable energy. As of today, important primary energy sources for the evaporation are limited and globally unevenly distributed fossil fuels, whose combustion releases greenhouse gases. For a transition in the energy system to the use of fluctuating renewable energies, such as wind and solar, suitable energy storages can be used to meet a demand-based energy supply. With regenerator type latent heat thermal energy storages, thermal energy can be stored at a constant temperature level by utilizing the phase change enthalpy of a phase change material (PCM). Since the evaporation of a liquid is also an isothermal process, a low and constant temperature difference can be realized when transferring heat from a PCM to an evaporating liquid; this can be used for increased exergetic efficiency. During the evaporation/discharging process of a latent heat thermal energy storage, a solid layer of PCM solidifies on the heat transfer surface, which reduces the heat transfer, as many PCMs have a low thermal conductivity.

In the novel Rotating Drum Heat Exchanger studied in this thesis, a rotating drum is partially immersed in liquid PCM. While a liquid evaporates on the inner side of the drum, PCM solidifies on the outer side. The solidified PCM is removed by a stationary scraper with each rotation. Therefore, the average layer thickness of the solidifying PCM and thus the heat transfer can be controlled by the rotational speed. Furthermore, the solidified PCM can be stored separately from the liquid material, resulting in complete separation of power and capacity of a storage system based on the Rotating Drum Heat Exchanger. An experimental test rig developed as part of this work serves as proof of concept of the Rotating Drum Heat Exchanger, using the low-temperature PCM decanoic acid and water as the heat transfer fluid. Thereby, a surface specific heat transfer density of up to 6.8 $\mathrm{kW \cdot m^{-2}}$ could be measured at a temperature difference of 5 K between the melting point of the PCM and the temperature of the heat transfer fluid. The experimentally examined heat transfer is used to validate a developed numerical model, which reproduces the experimental heat transfer with an accuracy of 8 % on average. To obtain a freely scalable design, the so-called multiple-channel drum is developed for generating steam in the multi-megawatt range. Therein, nitrate salts are proposed as the PCM, similar to the material used in state-of-the-art two-tank molten salt storages, which utilize only the sensible heat storable in the liquid phase. The Rotating Drum Heat Exchanger is able to transfer both the latent as well as the sensible heat of the storage material. The thermal capacity of the material can thereby be increased by up to 60 % compared to the state-of-the-art, which might result in cost savings for the storage system.

Kurzzusammenfassung in deutscher Sprache

Seit der industriellen Revolution ist das Verdampfen von Wasser die gängigste Methode zur Bereitstellung industriell nutzbarer Energie. Eine wichtige Primärenergiequelle dafür sind auch heute noch fossile Brennstoffe, welche nur begrenzte zur Verfügung stehen, weltweit ungleich verteilt sind und deren Verbrennung Treibhausgase freisetzt. Bei der Umstellung des Energiesystems zur Nutzung fluktuierender erneuerbarer Energie, können Energiespeicher eine bedarfsgerechte Energieversorgung gewährleisten. Mit Latentwärmespeichern kann thermische Energie durch Ausnutzung der Phasenwechselenthalpie eines Phasenwechselmaterials (PCM) bei konstanter Temperatur ein- und ausgespeichert werden. Da auch der Verdampfungsprozess isotherm ist, kann bei der Wärmeübertragung von einem PCM auf eine verdampfende Flüssigkeit eine niedrige und konstante Temperaturdifferenz eingestellt werden, wodurch der exergetische Wirkungsgrad erhöht wird. Während der Verdampfung bzw. des Entladens eines Latentwärmespeichers bildet sich eine wärmedämmende feste PCM-Schicht auf der Wärmeübertragerfläche, welche den Wärmedurchgang beeinträchtigt.

Bei dem untersuchten neuartigen Rotating Drum Heat Exchanger ist eine rotierende Trommel teilweise in flüssiges PCM getaucht. Während im Inneren eine Flüssigkeit verdampft, verfestigt sich PCM auf deren Außenseite. Das erstarrte PCM wird bei jeder Umdrehung durch einen stationären Schaber entfernt. Somit kann die Schichtdicke des festen PCM und damit die Leistung über die Drehzahl gesteuert werden. Die Möglichkeit das erstarrte PCM getrennt vom flüssigen PCM zu lagern resultiert in einer Trennung von Leistung und Kapazität. Ein aufgebauter Versuchsstand dient als konzeptioneller Beweis des Rotating Drum Heat Exchangers, wobei ein Niedertemperatur-PCM und flüssiges Wasser als Wärmeträgerflüssigkeit verwendet werden. Dabei kann eine Wärmestromdichte von bis zu 6.8 $kW \cdot m^{-2}$ bei einer Temperaturdifferenz von 5 K zwischen dem Schmelzpunkt des PCM und der Temperatur der Wärmeträgerflüssigkeit gemessen werden. Die experimentellen Daten werden zur Validierung eines neuen numerischen Modells verwendet, das den Wärmedurchgang mit einer Genauigkeit von durchschnittlich 8 % reproduziert. Für eine freie Skalierbarkeit zur Dampferzeugung im Multi-Megawatt-Bereich wird die sogenannte Mehrkanaltrommel entwickelt. Dabei werden Nitratsalze als PCM vorgeschlagen, ähnlich dem Material in modernen Flüssigsalzspeichern. Während diese Speicher nur die in der flüssigen Phase speicherbare sensible Wärme nutzen, kann der Rotating Drum Heat Exchanger sowohl die latente als auch die sensible Wärme des Speichermaterials übertragen. Somit kann die thermische Kapazität des Materials um bis zu 60 % erhöht werden, was zu Kosteneinsparungen im Vergleich zum Stand der Technik führen kann.

Nomenclatur

Latin

s	(specific-)entropy, $[s] = \mathrm{J{\cdot}kg^{-1}{\cdot}K^{-1}}$
T	temperature, $[T] = \mathrm{K}$

Greek

η	efficency, $[\eta] = \%$

Sub-/Superscripts

amb	ambient
C	cold
H	hot
m	melting

Abbreviations

CAES	compressed air energy storage
CHEST	compressed heat energy storage
COP	coefficient of performance
ORC	organic rankine cycles
CSP	concentrated solar power
HTF	heat transfer fluid
PCM	phase change material
PSH	pumped storage hydroelectric

1 Introduction

Renewable energy from solar and wind has the potential of an almost unlimited access to energy without dependence on unevenly distributed, CO_2-emmiting and limited fossil fuels. Over the past decade, the global weighted-average levelized cost of electricity of newly commissioned solar photovoltaic projects has fallen by 85 % to 57 USD·MWh^{-1}, while the cost of onshore wind farms has fallen by 56 % to 39 USD·MWh^{-1}. It is expected that these prices continue to decline and that electricity from wind and solar become the cheapest source of electricity available [1]. In order to fully exploit the economic and ecological potential of energy from wind and sun, the inherently intermittent nature of these sources must be overcome to create a reliable and demand orientated energy source. This can be met by suitable energy storages.

Technologies for large-scale electricity storage that have been put into operation to date are pumped storage hydroelectric plants (PSH) and compressed air energy storage (CAES) – both technologies require geographic and geological conditions and are therefore not freely scalable. In recent years, electrochemical energy storage has come into increased focus, particularly with regards to electric vehicles and home applications in combination with photovoltaic systems. In this context, various types of lithium-ion batteries are most common and state-of-the-art. Besides storing electricity, energy can also be stored in form of thermal energy. Almost half of the world's final energy demand is required in the form of thermal energy, mainly for industrial processes and residential heating [2]. Storing energy in the form of thermal energy needed later may offer cost advantages compared to electricity storage. In addition, storing energy in the form of thermal energy may also offer advantages in terms of critical resources and the carbon-footprint of the production process of the storage [3-5]. In addition to the direct use of thermal energy according to demand, the stored thermal energy can also be converted into electricity by a suitable thermodynamic cycle, e.g. a Rankine-Cycle. In the case of a thermal storage for the generation of electricity, which is also charged by electricity, a so-called Carnot-Battery is obtained.

Within this thesis, a novel heat exchanger for the transfer of both latent as well as sensible heat, which is predestined for the generation of process steam and the use in Carnot-Batteries, is developed and investigated in detail. Therefore, the state-of-the-art of high temperature sensible and latent heat storages is presented in the following sections followed by the specific requirements of the heat exchanger for the use in Carnot-Batteries and for the generation of process steam. This leads to the development of the Rotating Drum Heat Exchanger, which is described in Section 2.

1.1 High temperature thermal energy storage

Thermal energy can be stored today according to three main principles. Sensible thermal energy storages utilize the thermal energy that can be stored by changing the temperature of a storage material. In this process, the storage material does not change its state of aggregation. Thermal energy can be stored in any state of aggregation, but since the volumetric heat storage capacity in the gaseous state is usually low, the solid or liquid state is usually used. Latent heat thermal energy storages utilize the phase change enthalpy of a phase change material (PCM), usually from the liquid to the solid state. Thermochemical energy storages utilize a chemical reaction to store thermal energy. Identical or similar storage material can be used in sensible thermal energy storages and latent heat thermal energy storages. With the Rotating Drum Heat Exchanger, the advantages of both principles can be combined. Therefore, the following chapter discusses the state-of-the-art and current research on sensible molten-salt and latent heat thermal energy storages.

1.1.1 Molten Salt thermal energy storage

The simplest form of thermal energy storage is the use of water as storage material in a temperature range between 0 °C and 100 °C. Therefore, hot water storages are widely used in low-temperature applications such as space heating. The boiling point of water at ambient pressure at 100 °C limits the maximum temperature of hat water storages in non-pressurized systems. By using thermal oils as storage materials, the maximum operating temperature can be increased up to 400 °C. The use of molten salts allows a further increase of the maximum operating temperature.

The state-of-the-art of large-scale high-temperature sensible heat thermal energy storages are two-tank systems using Solar Salt as storage material. Thereby, a hot and a cold storage tank are connected via a heat exchanger. During the charging process, cold storage material is pumped from the cold storage tank to a heat exchanger, heated up and further pumped into the hot storage tank. In the discharging process, the hot storage material is used to heat up or evaporate a medium in the heat exchanger and afterwards pumped back into the cold storage tank. Solar Salt is a non-eutectic mixture of 60 wt% of sodium nitrate and 40 wt% of potassium nitrate. The choice of this composition is a result of optimization in terms of cost, melting temperature and heat capacity [6]. Commercial two-tank molten salt storage systems typically operate in a temperature range between 290 °C and 560 °C. While the lower temperature limit results from the solidification temperature of the Solar Salt at about 250 °C, the upper temperature limit results from the decomposition temperature of the storage material. The temperature difference of 250 K between the cold and hot storage tank and the specific heat capacity of the Solar Salt results in a volumetric heat storage density of about 200 $kW \cdot m^{-3}$.

Current research on two-tank molten salt storages focus on extending the operating temperature limits towards an increased temperature difference. Increasing the temperature difference leads to a higher storage density of the storage material and thus to cost savings due to less demand of storage material and smaller storage tanks. The focus of research to lower the minimum temperature limit is to find and characterize alternative salt mixtures, e.g. ternary and quaternary mixtures with a lower melting point [7]. To increase the maximum temperature limit, research is being conducted to gain a detailed understanding of the decomposition mechanisms of Solar Salt with the aim of finding methods to prevent the decomposition [8, 9]. Alternative storage materials with a higher decomposition temperature are also under investigation, such as carbonate and chloride salts [10, 11].

Besides current research on improving the storage material, there is extensive research on so-called thermocline single-tank storages. Here, a single tank is completely filled with a storage material. While hot material is withdrawn at the top of the storage, cold material is put back at the bottom. By inserting an inexpensive porous filler material e.g. basalt rocks, storage material can be substituted [12, 13]. At the time of writing this thesis, no commercially used large scale molten salt thermocline storage is known to the author.

Molten salt storages were originally developed for concentrated solar power (CSP) plants. Here, solar radiation is used by mirrors to generate steam, which drives an electrical generator via a steam turbine. By using a high temperature thermal energy storage, which is charged with thermal energy at times when the sun is shining, steam and thus electricity can also be produced in times of no solar radiation, e.g. during the nighttime. Due to the drop in the price of photovoltaic modules in the last decade, hybrid plants using electricity from renewable sources for direct resistive charging of molten-salt storages have also been proposed [14, 15].

1.1.2 Latent heat thermal energy storage

By utilizing the phase change enthalpy of a PCM, thermal energy can be charged and discharged in latent heat thermal energy storages at a constant temperature slightly above or below the phase change temperature of the PCM. In theory, any type of phase change can be used for the storage of thermal energy, including solid-solid transitions of the material and phase changes including the gas phase. Due to the usually minor change in the specific volume of the material and the relatively large phase change enthalpy, the phase change from the solid to the liquid state is commonly used in latent heat thermal energy storages. However, the inclusion of the solid state of the material requires increased technical effort regarding heat and mass transfer.

Intensive research has been done on latent heat thermal energy storages in the last decades and PCM storages are becoming increasingly commercialized [16]. The selection of a suitable PCM is thereby of particular importance, since the melting temperature of the PCM directly affects the application use of the storage system. In addition to a suitable phase change temperature, the material should have an appropriate phase change enthalpy, be non-toxic and non-corrosive, and be available in large quantities in an economically and ecologically acceptable manner. In the temperature range between 200 °C and 350 °C, nitrate salts have proven to be suitable PCMs. In particular, $NaNO_3$, KNO_3 and their eutectic mixture are economically available on a large scale and have suitable properties [17, 18].

Several studies and also standard literatures claim in general an increased storage density of latent heat thermal energy storages compared to sensible heat thermal energy storage. A closer look at the figures of these thermal energy storages reveals a more differentiated behavior: Latent heat thermal energy storages have a significant storage density within a small temperature difference around the melting point of the storage material. With an additional increase or decrease of the temperature of the storage material above or below the melting point, the PCM can be used as sensible storage material simultaneously. This increases the storage density of the material, since the phase change enthalpy as well as specific heat capacity of the material can by utilized. The resulting thermal energy storage is a combination of a sensible heat and a latent heat thermal energy storage.

Traditional application scenarios of latent heat thermal energy storages are applications where thermal energy has to be stored and released again within a small temperature range. In low-temperature applications, intensive research is being conducted on the use of latent heat thermal energy storages in the residential sector. Since the range of human comfort temperature is relatively small, latent heat thermal energy storages might lead to a gain in comfort or energy savings in case PCM are introduced into building envelopes [19, 20]. The isothermal melting and solidification characteristics of PCM fit well with the isothermal condensation and evaporation temperature of water or other liquids. Therefore, in the high temperature range, latent heat thermal energy storages can be used as steam storages. Since the temperature differences between the condensing water and the melting PCM during the charging process and the evaporating water and the solidifying PCM during the discharging process can be kept constant, the exegetic losses can be reduced compared to sensible storages. The effective storage of steam is also a key element for the success of direct steam generating concentrated solar power plants [21-24].

For the technical use of phase change thermal energy storages, the main challenge remains the same in most cases: the thermal conductivity of suitable PCMs is comparatively low, especially their solid phase. This limits the heat transfer especially during the discharging process, since in this case the PCM solidifies at the heat exchanger surface, which reduces the heat transfer. To overcome this, so-called active and passive concepts have been suggested in the literature.

Passive concepts of latent heat thermal energy storages

For the enhancement of the thermal performance, several so-called passive approaches have been identified and published in the literature [25]. The techniques of the passive storages can be mainly divided into two different groups: improving the effective thermal conductivity of the PCM used and increasing the heat transfer surface [26]. The effective thermal conductivity of the PCM can be increased by incorporating nanoparticles [27, 28], micro-encapsulation [29, 30] or compression of the PCM to a composite [31]. The heat transfer surface can be increased by macro-encapsulation of the PCM [32-34] or by integrating a heat transfer structure into the PCM. The heat transfer structure can be made of irregular shape, e.g. foams of metal [35, 36] or of regular shape, e.g. fins [37, 38]. While the heat transfer can be adjusted constructively by the techniques presented above and a decent heat transfer can be realized, there is always a fixed ratio between the thermal power and the capacity of the storage in these passive concepts. Thus, if the thermal capacity of the storage is increased, the heat transferring surface also has to be increased, which increases the thermal power of the storage. For example, at state-of-the-art latent heat thermal energy storages with alumina fins, the ratio between the thermal power and capacity is controlled by the size of the heat transfer surface of the fins and the amount of PCM that solidifies on the fins. Since an entire latent heat thermal energy storage with fins consists of multiple fins, the size of the fins used has to be adjusted to match the required ratio of the entire storage. In other words: When the capacity of an existing storage is increased by an identical second storage, the maximum charging and discharging power of the storage is also doubled. There has been intensive research on the passive concepts presented above, and there are already industrially used high temperature latent heat thermal energy storages on a large-scale [39].

There is a high commercial potential for the use of short-term passive latent heat thermal energy storages to improve the energy efficiency of today's industrial systems, e.g. to provide backup capacities and to balance batch processes and peak demand.

Active concepts of latent heat thermal energy storages

As an alternative to the presented passive techniques, so-called active concepts have been proposed in the past. These concepts are characterized in an active movement of the solid PCM, which enables the separation of the power and capacity of latent heat thermal energy storages using an active heat exchanger. The movement of the solidified PCM can be achieved in different ways:

- Modification of the PCM to achieve a pumpable slurry after the solidification

The PCM can be modified in different ways to prevent the total solidification of a liquid. Instead, the fluid becomes a slurry that is still pumpable after the discharge process and thus the transfer of latent heat. This modification can be done by micro-encapsulation of the PCM and using of a carrier fluid for the transportation [40, 41]. Another way to obtain a slurry is to mix a suitable PCM directly with a carrier fluid. With a suitable composition, the PCM is either suspended or emulsified in the carrier liquid [42, 43]. Since all of the PCM has to be modified, which might increase the costs of the material, PCM slurries are mainly used as isothermal heat transfer fluid (HTF).

- Transport of macro-encapsulated PCM

Macro-encapsulation of PCM enables the transport of both liquid and solid PCM by moving the entire container with the PCM. In the PCM-Flux concept, rectangular containers are moved linearly over a locally fixed heat exchanger. To increase the heat transfer between the moving container and the stationary heat exchanger, an intermediate fluid can be used. [44]

- Direct contact heat exchanger

In direct contact heat exchangers for latent heat thermal energy storages, an HTF is in direct contact with the PCM without physical separation like a heat exchanger wall from each other. Here, the combination of the HTF and the PCM is crucial since the components have to be separated after the heat exchange. A challenge with this type of heat exchanger is maintaining channels in the solidifying PCM to keep the HTF in motion. The HTF, which is usually in a liquid state, can also serve as an intermediate fluid to heat or cool a secondary fluid. Direct contact heat exchangers for latent heat thermal energy storages can be considered as hybrid versions of passive and active latent heat thermal energy storages. While there is usually no need for an active movement of the solid PCM, there is also no direct connection of the heat transfer surface to the PCM. [45-49]

- Scraped heat exchangers

At scraped heat exchangers, the solidified PCM is removed from the heat exchanger surface by a scraper. This allows the separation of the solidified PCM from the liquid PCM and increases the heat transfer due to the removal of the isolating solid layer of PCM. The design of the scraper can be diverse. A first collection and discussion of different designs can be found in [48] and [49], published in 1979 and 1980, respectively. However, no experimental data from these concepts have been published. In [50], the Screw Heat Exchanger Concept is described and experimental details and results are available in further publications. Here, two parallel screws, known from plastic extrusion, are used as heat exchanger. The screws are scraped towards each other to remove the solid PCM while they are capable to transport the solid PCM simultaneously. A concept and experimental data of a horizontal plate heat exchanger whose surface is periodically scraped by a linear moving scraper is presented in [51]. A scraped heat exchanger can also be placed in a vertical cylindrical tank, whose inner surface is scraped by a rotating scraper. Thereby, the shell of the cylinder is cooled during the discharge process. Two experimental setups of a scraped vertical cylinder are known [52, 53].

At the time of writing this thesis, no commercially used active concept for the purpose of heat storage is known to the author.

1.2 Application scenarios

The availability of thermal energy storages with specific properties are essential for the success of so-called Carnot-Batteries. In addition, process steam generation can be decarbonized by suitable thermal energy storages. The principles of Carnot-Batteries and the required properties of suitable thermal energy storages are discussed in the following section, followed by a discussion of the process steam supply.

1.2.1 Carnot Battery

According to the first law of thermodynamics, different types of energy can be converted into each other. Accordingly, thermal energy storages can be used as electrical energy storages if a suitable thermodynamic cycle is used to convert the stored thermal energy into mechanical and finally into electrical energy. The maximum efficiency of the conversion of thermal energy into mechanical energy is limited by the second law of thermodynamics, the so-called Carnot-Efficiency. The Carnot-Efficiency can be calculated by the absolute temperature of a hot reservoir T_H and a cold reservoir T_C by

$$\eta_{Carnot} = 1 - \frac{T_C}{T_H}.$$

Assuming a temperature of the hot reservoir of $T_H = 306$ °C, which corresponds to the melting temperature of $NaNO_3$, and a typical ambient temperature of $T_C = 15$ °C, which is assumed to be the temperature of the cold reservoir, the maximum possible efficiency is 50 %. Thereby, an ideal Carnot-Cycle is implied and the calculated efficiency is therefore only a theoretical maximum value.

Since the Carnot-Cycle is an ideal and reversible cycle, the process can be reversed. Thus, mechanical energy is used while thermal energy is transferred from the cold reservoir to a hot reservoir. In this case, an ideal Coefficient of Performance (COP) can be calculated by

$$COP_{Carnot} = \frac{T_H}{T_H - T_C} \ ,$$

which results for the same temperatures as above as $COP_{Carnot} = 2$. The number shows how much parts of thermal energy can be lifted from the cold temperature reservoir to the hot temperature reservoir by introducing one part of mechanical energy into the system.

Assuming an ideal thermal energy storage charged by a reverse Carnot-Cycle and discharged by a nominal Carnot-Cycle, the roundtrip-efficiency of the ideal energy storage system is calculated by

$$\eta_{Roundtrip} = \eta_{Carnot} * COP_{Carnot} \ ,$$

which is always 100 % in case of equal temperatures during the charging and discharging process.

When using a thermal energy storage as hot reservoir, the storage needs to be charged with thermal energy. To do this, thermal energy has to be transferred to the storage medium, which is only possible at a temperature above the storage temperature. The same restriction applies to the discharge process. Here, the thermal energy has to be discharged with an additional temperature difference. Therefore, in real systems, the temperature transferred from the hot reservoir T_H during the discharge process is lower, while the temperature transferred to the hot reservoir T_H during the charging process is higher.

The influence of the required temperature difference is shown in Figure 1, also assuming a temperature of the hot reservoir of T_H = 306 °C, which corresponds to the melting temperature of $NaNO_3$, and an ambient temperature of T_C = 15 °C as cold reservoir. Here, the required temperature difference is assumed to be equal and constant during the charging and discharging process. An additional temperature difference at the cold reservoir required in real systems is neglected. Figure 2 virtualizes the thermodynamic process of an ideal Carnot-Battery based on the Carnot-Process. While the ideal Carnot-Process is only of theoretical nature, real Carnot-Batteries based on thermal energy storage today are mainly based on the Rankine- and the Brayton-Cycle. Thereby, both cycles have specific advantages and disadvantages, while the achievable roundtrip efficiency of both are similar at about 60 - 70 % [54]. Brayton-Cycle based Carnot-Batteries operate at higher temperatures of up to 1000 °C and with a working fluid that is gaseous at all times. As thermal energy storages, sensible heat storages such as regenerators or molten salt storages are

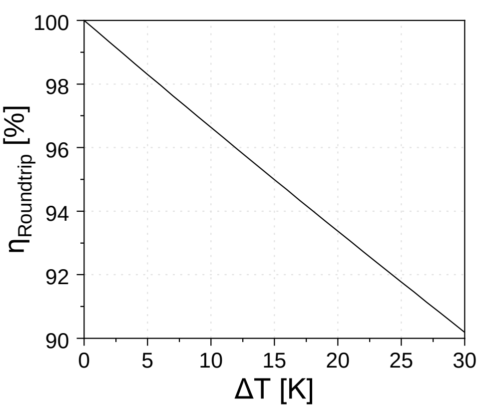

Figure 1: Roundtrip efficiency of an ideal Carnot-Battery based on the Carnot-Cycle as a function of the temperature differences to the hot reservoir. Assuming T_H = 306 °C and T_C = 15 °C

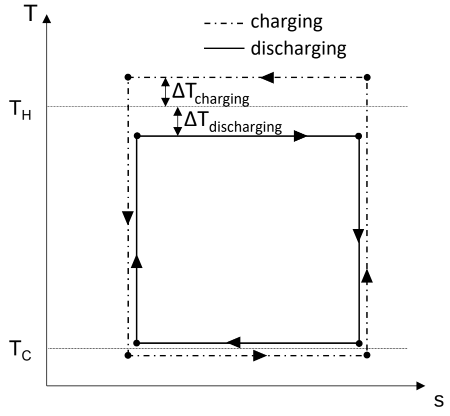

Figure 2: T-s-Diagram of an ideal Carnot-Cycle based Carnot-Battery and visualization of the influence of the temperature differences to the hot reservoir

suggested [55, 56]. Due to the higher storage temperatures, the exegetic losses during the heat transfer have only a minor effect on the roundtrip efficiency. On the other hand, the high temperatures increase the efficiency losses due to losses of thermal energy through the insulation of the storage tanks. In Carnot-Batteries based on the Rankine-Cycle, the working fluid undergoes a phase change from the liquid to the gaseous state and vice versa. This allows lower working temperatures in the range from below 100 °C up to 500 °C while maintaining a reasonable power density of the thermodynamic cycle. The lower temperatures allow the integration of low-temperature heat or the additional provision of residential or industrial heat [57, 58]. In general, Rankine-Cycle based batteries can be divided into subcritical and transcritical systems. Transcritical systems often use CO_2 as working fluid and a sensible storage for the hot reservoir, since the temperature is gliding during the phase change of a supercritical fluid. Thereby, a latent heat ice storage is often suggested as low temperature reservoir [59, 60].

In subcritical Rankine-Cycles, the working fluid undergoes an isothermal phase change during evaporation and condensation. In the so-called CHEST-Concept (Compressed Heat Energy STorage), mainly water is used as working fluid. While the discharge process is similar to the well-known Rankine-Cycle of thermal power plants, the charging process is separated into two compression cycles, one using ammonia and one using water as working fluid. A latent heat thermal energy storage using NaNO3 with a melting temperature of 306 °C is proposed as thermal energy storage [61]. When using refrigerants as working fluids, the temperature of the hot reservoir can be lowered to the range of 100 °C – 150 °C. This allows the use of more conventional components as known from heat pumps and Organic Rankine Cycles (ORCs) [57, 62]. The isothermal characteristic of the evaporating process of the working fluid predestines the use of latent heat thermal energy storages in these subcritical Rankine-based Carnot-Batteries. In Figure 3, the T-s-Diagram of a Rankine-Cycle bases Carnot-Battery is shown. As one can see, minimizing the temperature differences during the charging process as well as during the discharging process with respect to the temperature of the thermal energy storage is crucial for an optimized roundtrip efficiency. The roundtrip efficiency can further be increased by combining sensible and latent heat thermal energy storages [57, 63, 64].

Carnot-Batteries are mostly proposed for a storage duration of 10 – 100 h, which is similar to today's pumped hydro storages [65, 66]. They are therefore to be placed between the short-term electrochemical storages (e.g. Lithium Batteries) and long-term chemical storages (e.g. Hydrogen). Beside the systems described above, numerous other configurations of Carnot-Batteries have been published, especially in the last decade. Thereby, different working fluids, concepts of thermal energy storages

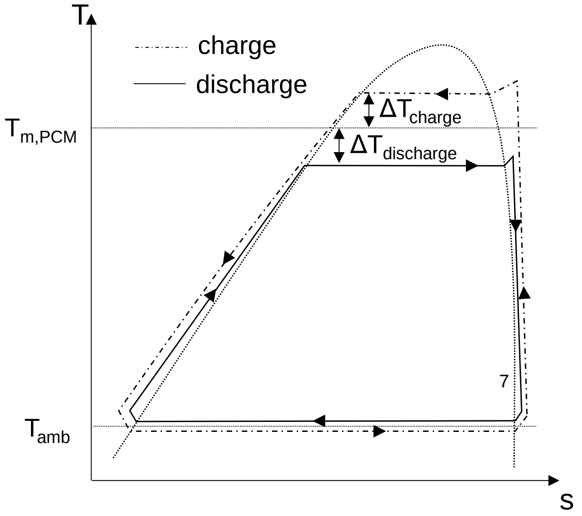

Figure 3: T-s-Diagram of a Rankine-Cycle based Carnot-Battery using a latent heat thermal energy storage

including ice storages and the integration of additional thermal energy at different temperature limits are calculated and discussed in detail. A recent review of Carnot-Batteries can be found in [54]. A review of Rankine-based systems is given in [58]. In the recent years, about a dozen demonstration plants of Carnot-Batteries, which include a thermal energy storage and heat pump, have been experimentally demonstrated by both commercial and research institutions. Thereby, the electrical power is in the range of several KW up to a few MW. A recent review of the commercial use of Carnot-Batteries can be found in [67].

For the commercial success of Carnot-Batteries, suitable thermal energy storages are crucial. Due to the considerable effort required in terms of machinery, Carnot-Batteries will be economically favorable in the MW to GW range. A required storage duration of 10 – 100 h results in large storage capacities of the thermal energy storages from several hundred MWh up to few GWh. For subcritical Rankine-based Carnot-Batteries, a small temperature difference to a constant temperature level of the thermal energy storage is crucial for a high roundtrip efficiency. This predestines the use of active latent heat thermal energy storages.

1.2.2 Process steam generation

For industrial processes, process steam is an important energy carrier for the supply of thermal energy of numerous processes. Process steam accounts for about 5 % of the final energy consumption, which is about 125 TWh per year in Germany and 650 TWh in Europe [68-71]. For comparison, the total electricity generation in 2019 was 600 TWh in Germany and around 3200 TWh in Europe [72]. An electrification of the entire process steam generation in Germany would require about the same amount of electricity as the electrification of the entire passenger car fleet. In 2013, the total installed capacity of steam generators for process steam generation in Europe was around 770 GW [69]. For the number of steam generators installed, figures between 70 000 and 100 000 can be found [69, 73]. Fossil gas is thereby the most common source of energy.

Depending on the required process steam parameters and the ration between the required electricity and process steam, mainly three different technologies are used in large scale process steam generator units nowadays:

- Direct process steam generation in steam boilers with the required steam parameters. In this process, no electricity is generated and the energy used is completely converted into thermal energy in form of steam.
- Generation of steam with higher steam parameters in steam boilers and expansion of the steam in backpressure turbines to the required steam parameters. In this case, the share of electricity generated is in the range of up to 30 %.
- Use of a gas turbine combined with a heat recovery steam generator for the generation of steam. The generated steam can either be used directly as process steam or can be expanded in a steam turbine. By doing so, up to 50 % of the used energy can be transformed into electricity.

The choice of a certain technology and thus the ratio between steam and electricity generation is usually made in order to achieve the highest possible degree of self-sufficiency. Additional integration of fluctuating renewable energies into the existing energy system of such factories often brings the ratio between electricity and process steam apart. This might prevent the additional integration of renewable energies. The generation of process steam and electricity can be decoupled in time by a suitable thermal energy storage. This would allow further integration of low-cost but fluctuating renewable energies in the existing process steam infrastructure.

With thermal energy storages, the process steam generation can also be almost completely decarbonized by using only locally generated, cheap but fluctuating renewable energy from wind and solar. In this case, a thermal energy storage with a capacity to cover 24-hour demand would be sufficient to achieve up to 90 % availability of the storage system, depending of the geographical location [74, 75].

The decarbonization of process steam by renewable sources of electricity competes economically with the direct combustion of natural gas. While the overall cost of electricity from solar and wind continuous to decrease, the fluctuating exchange prices of liberalized energy markets can also lead to cost savings. Thus, the exchange prices for electricity are favorable during periods of high availability of renewable energies and low electricity demand, but expensive during periods of low availability and high demand. For a success of the use of renewable energy for the generation of process steam, cheap and reliable thermal energy storages have to be available in addition to cheap electricity. An increased storage density might lead to cost savings and would also limit the ground area required for the installation of the storage system in an industrial environment.

2 The Rotating Drum Heat Exchanger

The Rotating Drum Heat Exchangers combines the advantages of latent heat and sensible heat thermal energy storages. The idea of the Rotating Drum Heat Exchanger is mainly guided by two aspects:

- Separation of power and capacity
- Thin solid layer thicknesses for maximized heat transfer

The power and capacity of two-tank molten salt storages are inherently separate. This allows the capacity to be chosen completely independently of the power of the heat exchanger, and vice versa. Increasing the size of the two storage tanks increases the capacity, increasing the surface of the heat exchanger increases the power. Compared to this, the power and capacity of state-of-the-art passive latent heat thermal energy storages are always connected to each other. If the amount of PCM used is increasing, the heat transfer surface has to be also increased. This limits potential cost savings due to scaling effects.

The second aspect arises from the basic heat transfer mechanism of latent heat thermal energy storages. Assume a heat transfer network with a phase change from the liquid to the solid state of a PCM on one side of a metal heat exchanger and an evaporating fluid at the other side of the heat exchanger. With a typical value for the thermal conductivity of cost-effective PCM of $\lambda_{PCM} = 0.5\ W \cdot m^{-1} \cdot K^{-1}$, an assumed heat exchanger thickness of $s = 5\ mm$, a thermal conductivity of the heat exchanger material of $\lambda_{HX} = 58\ W \cdot m^{-1} \cdot K^{-1}$ and a surface coefficient of heat transfer of the evaporating fluid of $h = 8000\ W \cdot m^{-2} \cdot K^{-1}$, the heat transfer resistance of the solid PCM dominates the heat transfer as of a thickness of $d = 0.1\ mm$. In Figure 4, the heat transfer resistances at different PCM layer thicknesses are virtualized and compered.

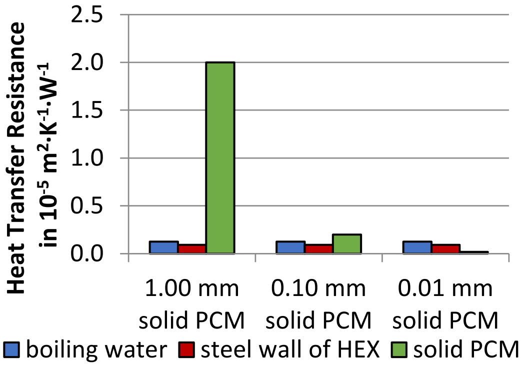

Figure 4: Typical values for the thermal resistance at a heat exchanger with solidifying PCM at one side of the heat exchanger and evaporating fluid at the other side (presented in the 1st publication)

At the Rotating Drum Heat Exchanger, a thin layer of solidified PCM is scraped off the heat exchanger surface and can thus be stored separately from the liquid PCM. Thereby, a hollow drum is mounted horizontally and partially immersed in liquid PCM. While the PCM solidifies on the outer surface of the drum shell, a fluid evaporates on the inner surface of the drum. The solidified PCM is removed from the drums shell with every rotation by a fixed scraper. The average layer thickness, and thus the heat transfer, can be controlled by the rotational speed of the drum. Figure 5 shows an illustration of the concept of the Rotating Drum Heat Exchanger. The Rotating Drum Heat Exchanger is the main component of an entire thermal energy storage system, which is illustrated in Figure 6. In addition to the Rotating Drum, the storage system consists of a hot and a liquid storage tank and an electrical or thermal heater for the charging process. Several pumps and, if necessary, a conveyer for the solid PCM provide the transport of the storage material.

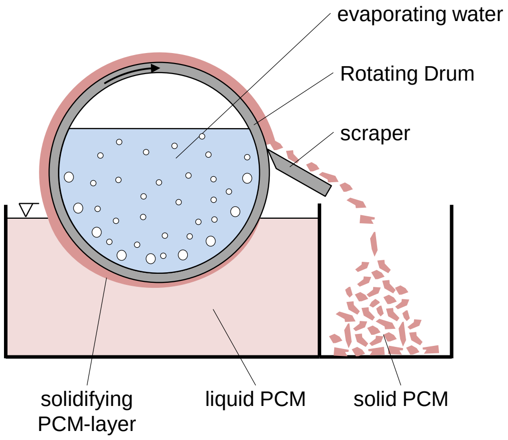

Figure 5: Concept of the Rotating Drum Heat Exchanger (presented in the 3rd publication)

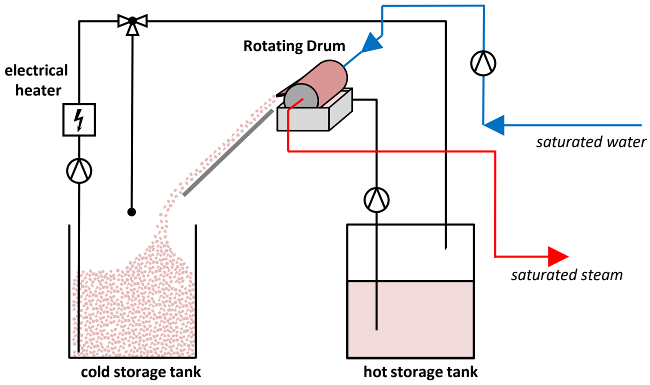

Figure 6: Basic thermal energy storage system based on the Rotating Drum Heat Exchanger (adopted from the 3rd publication)

2.1 Motivation - Advantages compared to state-of-the-art

The main advantage compared to state-of-the-art latent heat thermal energy storages is the mentioned separation of the thermal power and the thermal capacity. Passive latent heat thermal energy storages are predestined for the almost isothermal storage of steam with a duration of several minutes up to a few hours. Therefore, these storages can be widely used to compensate for load fluctuations and to bridge the steam supply in case of a failure of the main supply until a backup-boiler is started up. With the separation of power and capacity, the use of latent heat thermal energy storages can be extended into the range of storage with a capacity of several hours up to a few days – a range for which two-tank molten salt storages are typically used. A capacity of several hours up to a few days allows to compensate of the day and night rhythm of solar radiation as well as shading by clouds and the availability of wind energy up to a certain limit.

While two-tank molten salt storages are used commercially in CSP-plants, the technology faces a critical disadvantage: In case of solidification, the entire thermal energy storage can be destroyed. This is particularity critical with regard to possible black-outs, meaning periods when no electricity is available. Maintenance work and monitoring of system components are also made more difficult by this fact. In storage system based on the Rotating Drum Heat Exchanger, the storage material can be completely solidified by a controlled shutdown of the system.

The volumetric heat storage capacity of state-of-the-art molten salt storages is about 200 $kW \cdot m^{-3}$, which can be calculated from the specific heat capacity of solar salt and its minimum density at 560 °C [6]. Thereby, only the specific heat storage capacity of the liquid phase of the storage material is used. The Rotating Drum Heat Exchanger enables the transfer of sensible heat stored in both, the liquid phase and the solid state of the storage material in addition to the latent heat of the phase change of the storage material. As a result, the volumetric heat storage capacity can be significantly increased up to 330 $kWh\cdot m^{-3}$. The increased storage capacity reduces the amount of storage material required for a certain storage capacity, which leads to economic and ecological advantages. In addition, the size of the hot and the cold storage tank can be reduced, which also leads to lower investment costs for the storage system.

2.2 Objectives of the Research

The research questions of the present thesis arise from the concept of the Rotating Drum Heat Exchanger described in the previous section. Four main topics can be identified that leads to a specific research question, which are discussed in the following.

2.2.1 Proof of concept

Scraped active heat exchangers involving a phase change have already been published, and experimental details as well as a proof of concept for these designs are available, as described in Section 1.1.2. A initial experimental test rig of the Rotating Drum Heat Exchanger has been built before this work as part of a bachelor's thesis [76]. While a heat transfer was measured and a phase change of a PCM was observed, there were difficulties in the detailed examination of the heat transfer and the reliability of the test rig. Based on this, the present thesis answers the question: **Is the concept of the Rotating Drum Heat Exchanger suitable for the continuous transfer of heat released by the liquid to solid phase change of a phase change material?**

2.2.2 Experimental quantification of the heat transfer potential

For the quantification of the technical potential of the Rotating Drum Heat Exchanger and for comparison with other heat exchanger technologies, the transferred heat flow has to be quantified in as much detail as possible. The dependence of the heat transfer on the temperature differences have to be quantified as well. An experimental quantification of the heat transfer also allows the identification of further effects that have an influence on the heat transfer. The following research question can be formulated from this: **How much thermal energy can be transferred with the Rotating Drum Heat Exchanger and which physical effects have which influence on the heat transfer?**

2.2.3 Development of a calculation tool for the heat transfer

The availability of a validated calculation tool for the heat transfer and operating behaviour is of crucial interest for the application of the Rotating Drum Heat Exchanger. A calculation tool enables the design and sizing of a Rotating Drum Heat Exchanger for various applications. A central research question is therefore: **Can physical and mathematical models enable the calculation of the transferred heat at the Rotating Drum Heat Exchanger with which deviation?**

2.2.4 Industrial application of the Rotating Drum Heat Exchanger

For the application of the technology of the Rotating Drum Heat Exchanger in industrial processes, several criteria have to be satisfied. Thus, the power of the heat exchanger has to be increased to an industrial level while the size of the heat exchanger has to be convenient. The temperature and pressure level must also be raised to a reasonable level. Thus, the question arises: **How can the technology of the Rotating Drum Heat Exchanger be used to improve the industrial state-of-the-art?**

3 Publications

This thesis is based on the work published in the following journal contributions:

I. Experimental investigation

Jonas Tombrink, Henning Jockenhofer, Dan Bauer (2021): Experimental investigation of a rotating drum heat exchanger for latent heat storage. *Applied Thermal Engineering*, 183, 116221. https://doi.org/10.1016/j.applthermaleng.2020.116221.

Contribution declaration: main author, conduction of the experimental work and data evaluation

II. Simulation of the heat exchanger

Jonas Tombrink, Dan Bauer (2021): Simulation of a rotating drum heat exchanger for latent heat storage using a quasistationary analytical approach and a numerical transient finite difference scheme. *Applied Thermal Engineering*, 194, 117029. https://doi.org/10.1016/j.applthermaleng.2021.117029

Contribution declaration: main author, numerical model implementation and data evaluation

III. Upscaling and Application

Jonas Tombrink, Dan Bauer (2022): Demand-based process steam from renewable energy: Implementation and sizing of a latent heat thermal energy storage system based on the Rotating Drum Heat Exchanger. *Applied Energy*, 321, 119325. https://doi.org/10.1016/j.apenergy.2022.119325

Contribution declaration: main author, numerical model implementation and data evaluation

Classification of the scientific contributions of the three publications to the overall topic:

Within **Paper I,** the concept of the Rotating Drum Heat Exchanger is introduced, its feasibility to transfer thermal energy released during the phase change of a PCM towards an HTF is proven and the heat transfer is characterized experimentally in detail for different operation conditions. For this purpose, an experimental test rig is designed using the low temperature PCM decanoic acid and liquid water as HTF, whose details are published in **Paper I**. The heat transfer as well as the thickness of the solid PCM layer are determined for different operation modes, different rotational speeds and different temperature differences.

Based on these experimental results, a numerical simulation is developed and described in **Paper II** to further characterize of the heat transfer potential of the Rotating Drum Heat Exchanger. Therefore, models and calculation approaches for the physical phenomena involved into the heat transfer are identified. The model is reduced to a transient 1-dimensional scheme and the governing equations are discretized by using an implicit moving mesh method. The developed simulation is verified with analytical solutions and validated with the experimental data from **Paper I**. The simulation presented in **Paper II** enables a detailed characterization of the heat transfer also for operation conditions that cannot be investigated with the experimental test rig, as well as a full sensitivity study of the physical parameters.

The use of the Rotating Drum Heat Exchanger on an industrial scale with a thermal power in the MW range is investigated and discussed in **Paper III.** Therefore, the design of the Rotating Drum Heat Exchanger is adopted for high-pressure and large-scale application. By adopting the validated simulation developed in **Paper II** and extrapolating the temperature into the range of process steam, the operating behavior of a large-scale Rotating Drum Heat Exchanger is simulated. The large-scale design is discussed also for the co-generation of (process-)steam and electricity.

The three journal publications within this dissertation therefore cover the whole investigation and development of the Rotating Drum Heat Exchanger from the lab-scale test rig to the usage of the technology on an industrial scale.

Further parts of the research presented in this dissertation have been published in the following contributions to international conferences:

Jonas Tombrink, Erik Jung, Dan Bauer (2021): The additional heat flux due to adhesion at a partially immersed rotating drum heat exchanger for latent heat storage. 8th European Thermal Sciences Conference (EUROTHERM 2021), Sep. 20-23, 2021, virtual conference, (originally scheduled Sep 6-10, 2020 in Lisbon, Portugal)

Conference proceedings published in *Journal of Physics: Conferences Series*, 2113, 012097. https://doi.org/10.1088/1742-6596/2116/1/012097

Jonas Tombrink, Dan Bauer (2021): Demand orientated steam generation from latent heat by using a rotating drum. 15th International Conference on Energy Storage (ENERSTOCK 2021), June 9-11, 2021, virtual conference, (originally scheduled in Ljubljana, Slovenia)

Jonas Tombrink, Henning Jockenhöfer, Dan Bauer (2020): The rotating drum as an efficient and fully controllable heat exchanger for latent heat thermal energy storage. 14th International Renewable Energy Storage Conference 2020 (IRES 2020), May 25-26, 2020, virtual conference, (originally scheduled Mar. 10-12, 2020, Düsseldorf, Germany)

Jonas Tombrink, Henning Jockenhöfer, Dan Bauer (2019): Examination of the heat transfer potential of an active latent heat storage concept. Eurotherm Seminar nº112 – Advances in Thermal Energy Storage, May 15-17, 2019, Lleida, Spain

3.1 Paper I: Experimental Investigation

This article was published in *Applied Thermal Engineering*, 183, 116221, Copyright Elsevier (2020) https://doi.org/10.1016/j.applthermaleng.2020.116221

Applied Thermal Engineering 183 (2021) 116221

Contents lists available at ScienceDirect

Applied Thermal Engineering

journal homepage: www.elsevier.com/locate/apthermeng

Experimental investigation of a rotating drum heat exchanger for latent heat storage

Jonas Tombrink *, Henning Jockenhöfer, Dan Bauer

German Aerospace Center (DLR), Institute of Engineering Thermodynamics, Pfaffenwaldring 38-40, 70569 Stuttgart, Germany

ARTICLE INFO

Keywords:
Active latent heat thermal energy storage
Rotating drum
Scraped heat exchanger
Phase change material
Solidification
Adhesion

ABSTRACT

With latent heat thermal energy storages, thermal energy can be stored at a constant temperature level with high storage density using the enthalpy of the solid-liquid phase change of a material. During the discharge process of a latent heat thermal energy storage, phase change material (PCM) solidifies at the heat transfer surface and increases the thermal resistance. This decreases the transferred thermal power with time and the state of charge. The rotating drum heat exchanger, experimentally investigated in detail for the first time in this paper, overcomes this limitation by removing the PCM layer. While a heat transfer fluid passes through the inside of the rotating drum, which is partially immersed in liquid PCM, the PCM solidifies at the outer side. The solidified layer is removed at each rotation by a fixed scraper. Thus, the layer thickness and the thermal power are kept constant over time. The solidified PCM can be stored separately from the liquid phase, resulting in a complete independence of thermal power and storage capacity. A commissioned experimental test rig using a low temperature PCM is used for the investigation of the heat transfer potential, the layer thicknesses, the mechanical energy needed for the removal of the solidified layer and as a proof of concept. The experimental data show a consistent heat transfer which is increasing for higher rotational speeds. With the presented test rig, the heat transfer density is up to 6.8 kW·m^{-2} based on the total drums shell surface of the rotating drum at a temperature difference of 5 K between the melting point of the PCM and the temperature of the heat transfer. Adhering liquid PCM increases the total heat transfer by up to 60% as the liquid PCM solidifies also after the surface left the liquid PCM. While the measured solidified layer decreases to below 0.05 mm with higher rotational speeds, the adhering layer is slightly increasing. The results show the high potential of the rotating drum heat exchanger concept for the generation of steam out of a high temperature PCM.

1. Introduction

For the transition of the energy system from limitedly available and carbon dioxide emitting fossil fuel consumption towards the usage of fluctuating renewable energy, the demand of energy needs to be decoupled from its production. This can be achieved by using suitable energy storage systems. Renewable energy from solar and wind will be available primarily in form of electricity. However, the pure demand of thermal energy in industrial applications for process heat in the temperature range of 100–400 °C in the EU28 member states amounts to around 2200 PJ per year, which is around 5% of the total final energy consumption throughout all sectors [1]. Storing the energy in form of the required thermal energy offers advantages regarding the limited availability of critical resources for electrochemical energy storages and cost savings. Apart from that, there is the possibility to convert electricity from stored thermal energy by using a suitable thermodynamic cycle [2].

Latent heat thermal energy storages (LHTES) utilize the phase change enthalpy, usually between liquid and solid state, of the storage material (phase change material, PCM). Their essential characteristic is the isothermal temperature level during the melting (charging) and solidification (discharging) process. In applications that include isothermal processes, the required temperature difference for the heat transfer can be kept constant or minimized for an increased exergetic efficiency of the storage system. This includes the supply of process steam with specific requirements for industrial applications as well as the supply of organic- or water steam for electricity production. The exergetic efficiency is further maximized by an isothermal charging process e.g. by a condensing fluid (Fig. 1). By overheating the liquid PCM above its melting point or subcooling the solid PCM below its solidification temperature, the sensible heat of the PCM can be used for

---

* Corresponding author.
E-mail address: jonas.tombrink@dlr.de (J. Tombrink).

https://doi.org/10.1016/j.applthermaleng.2020.116221
Received 28 July 2020; Received in revised form 12 October 2020; Accepted 14 October 2020

Nomenclature

Latin	
c_p	heat capacity at constant pressure, $[c_p] = \text{J}\cdot\text{kg}^{-1}\cdot\text{K}^{-1}$
$\dot{m}$	mass flow, $[\dot{m}] = \text{kg}\cdot\text{s}^{-1}$
n	rotational speed, $[n] = \text{min}^{-1}$
P	(electrical-) power, $[P] = (\text{W})$
p	pressure, $[p] = \text{Pa}$
Q	heat flow, $[Q] = \text{W}$
s	thickness, $[s] = \text{m}$
T	temperature, $[T] = \text{K}$
t	time, $[t] = \text{s}$
x	length, $[x] = \text{m}$
Greek	
α	heat transfer coefficient, $[\alpha] = \text{W}\cdot\text{m}^{-2}\cdot\text{K}^{-1}$
Δh	heat of fusion of the PCM, $[\Delta h] = \text{J}\cdot\text{kg}^{-1}$
ΔT	temperature difference, $[\Delta T] = \text{K}$
η	dynamic viscosity, $[\eta] = \text{Pa}\cdot\text{s}$
Θ	immerging angle, $[\Theta] = {}^\circ$
λ	thermal conductivity, $[\lambda] = \text{W}\cdot\text{m}^{-1}\cdot\text{K}^{-1}$
ϱ	density, $[\varrho] = \text{kg}\cdot\text{m}^{-3}$
Subscripts/Abbreviations	
char	charge
dischar	discharge
HTF	Heat Transfer Fluid
LHTES	Latent Heat Thermal Energy Storage
l	liquid
m	melting
PCM	Phase Change Material
s	solid

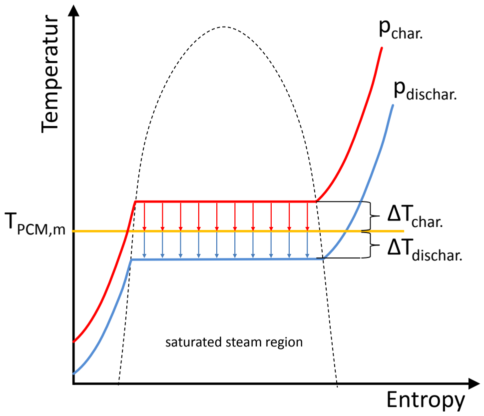

Fig. 1. Constant temperature difference during charging and discharging of a PCM-Storage.

energy storage as well. This increases the storage density and decreases the specific costs of the storage material simultaneously. For the generation of steam in a temperature range between 150 °C and 350 °C, nitrate salts are well suited. Especially sodium nitrate is cost attractive and has an abundant availabillity [3]. However, these materials have a limited thermal conductivity. During the discharge process, liquid PCM is solidifing at the cooled heat exchanger surface and a solidified PCM layer is growing. The phase change enthalpy released during the phase change is emitted at the boundary between solid and liquid PCM as shown in Fig. 2. Thus, the thermal energy has to be transferred through the growing solidified layer. This causes a decline of the heat transfer capability during the discharge process with time and state of discharge. During the charging process of a LHTES the solidified PCM layer is melted at the heat exchanger surface. The heat transfer from the liquid PCM to the heat exchanger surface is increased by natural convection [4,5] and can be further increased by forced convection. Therefore, most activities to improve LHTES are focusing on the discharge process as is the case in this work.

To overcome the discharge limitation, extensive reaserch has been conducted on so called passive LHTES. Among others, the mainly used basic principles are to increase the effective heat transfer surface or to increase the effective thermal conductivity of the PCM. The effective heat transfer can be increased by integrating a heat transfer structure in the PCM [6–9] or a macro-encapsulation of the PCM [10]. The effective thermal conductivity can be increased by modifying the PCMs thermal properties e.g. by incorporating of nanoparticles [11,12], micro-encapsulation [13,14] or compression of the PCM to a composite [15]. However, the thermal power and thermal capacity of conventional passive LHTES with fixed heat exchangers and non-moving PCM is defined by its design at a certain ratio. Thus, if the capacity is enlarged, the heat transfer structure has to be incresed as well. This limits possible cost savings due to scaling effects especially for large long-time storages. Another possibility to overcome the limited heat transfer potential of available low cost PCMs is the use of active LHTES. Here, an active motion transports the PCM. This results in a constant heat transfer as the solidified layer thickness is kept constant in average. Beside the rotating drum firstly introduced in [16] and discussed in detail in this paper, further concepts of active LHTES have been published. Among others, these are mainly:

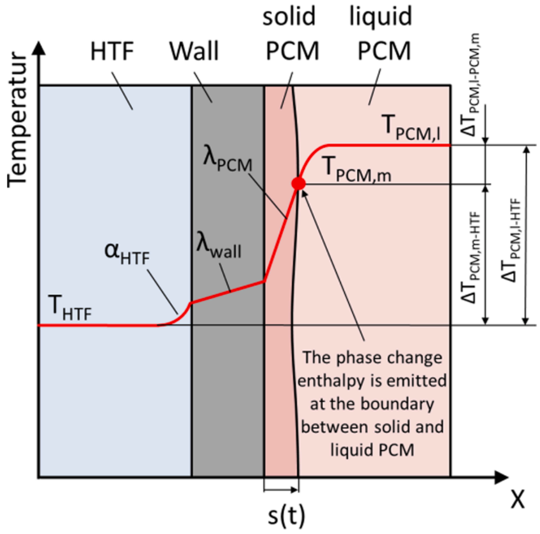

Fig. 2. Temperature profile of a heat exchanger between a HTF and solidifying PCM.

- The Screw-Heat-Exchanger concept, in which two parallel screws, known from the plastic extrusion, are transporting the PCM and serve as heat exchanger [17].
- In the PCM-Flux concept, PCM is moved in a container linearly over a locally fixed heat exchanger [18].
- In [19], a plate heat exchanger is presented, whose heat transfer surface is periodically scraped off by a linearly moving scraper.

- A vertically rotating, scraped rotating drum with PCM around the drum in a closed enclosure is presented in [20].

All of these concepts have been demonstrated experimentally on an experimental scale. However, all of them have in common, that there is a layer thickness of solid PCM given at the heat exchanger surface, which dominates the heat transfer. Further concepts of scraped surface heat exchangers are mainly optimized for the process of freezing or for the increase of the convective heat transfer without solidification [21–24]. Within Fig. 3, the thermal resistances of a typical heat transfer problem of latent heat storages are given. The solidified PCM layer clearly dominates the heat transfer resistance if it is thicker than 0.1 m. Only with a further reduction of the solidified PCM layer thickness the thermal resistances of the steel wall and the evaporating water become dominant.

The novel concept of the rotating drum heat exchanger is designed from scratch to minimize the layer thickness of the solid PCM and thus maximize the surface specific heat transfer of the heat exchanger. Furthermore, a separation of the solidified PCM from the liquid PCM is a key element for the separation of power and capacity. The basic concept of the rotating drum heat exchanger is shown in Fig. 4. A rotating drum is partially immersed into liquid PCM. An evaporating fluid extracts thermal energy while passing the inside surface of the heat transfer wall. Simultaneously, liquid PCM releases its phase change enthalpy during solidification at the outer surface of the wall. To maintain a minimum thickness of the solidified PCM layer, a fixed scraper removes the layer with each rotation. The scraped PCM can be stored separately from the liquid PCM. This leads to a complete separation of the thermal power that can be transferred and the thermal energy that can be stored with the thermal energy storage system. The separation leads to cost savings for medium and long-term storages with high storage capacities, since the heat exchanger as the main part of the storage system can be chosen independently in its size. The transferred thermal energy can be controlled by the rotational speed. This leads to a flexible system for the provision of changing steam requirements. The overall specific thermal energy density of the storage material can be increased by extending the temperature range used above and below its phase change temperature. Thus, the energy density is composed of the latent heat of the phase change and the sensible heat stored in both the liquid and the solid phase of the storage material. The maximum temperature of the liquid PCM is limited by the decomposing temperature of the PCM or the material specific maximum operating temperature of the rotating drum and its components.

Within this paper, the concept of the rotating drum heat exchanger for latent heat storage is examined experimentally in detail for the first time. Therefore, an experimental test rig using a low-temperature PCM is commissioned. The use of a low-temperature PCM allows a more detailed investigation of the various effects while the basic physical properties of the heat transfer remain unchanged compared to a high temperature system. The methodology of the experimental investigation is described in the following section. The main objective of the research is a proof of concept and to identify the technologies potential regarding the heat transfer. Furthermore, the influence of different effects such as adhesion and different temperature differences are examined.

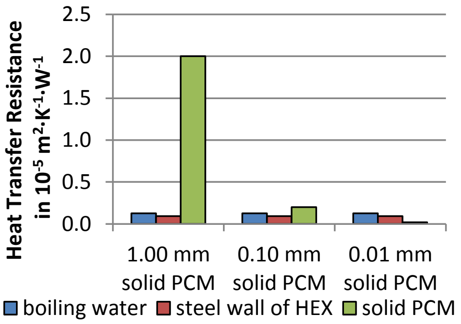

Fig. 3. Typical values for the thermal resistances of the heat transfer network shown in Fig. 2 for boiling water ($\alpha = 8000$ W·m^{-2}·K^{-1}), boiler steel wall ($\lambda = 54$ W·m^{-1}·K^{-1}, s = 5 mm) and sodium nitrate as PCM ($\lambda = 0.5$ W·m^{-1}·K^{-1}).

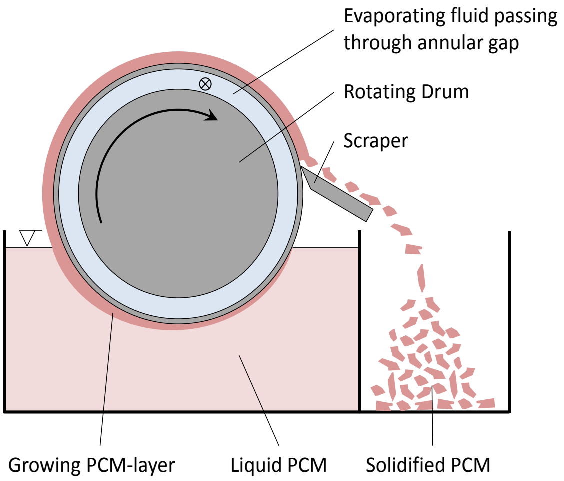

Fig. 4. Principle of the rotating drum heat exchanger.

2. Experimental details

The experiments aim is a proof of the concept and an examination of its heat transfer potential. Furthermore, the layer thickness, the adhering liquid PCM and the mechanical energy required to remove the solidified PCM are determined. The experimental test rig is introduced in the following section. Liquid water is used as HTF and the low temperature PCM decanoic acid is used for a detailed examination of the heat transfer.

2.1. Overall design of the experimental test rig

The main part of the experimental test rig is a rotating steel drum which serves as the heat exchanger. The design and the geometrical properties of the rotating drum are given in Fig. 5. It is made out of pressure vessel steel P235GH with a thermal conductivity of 54 W·m^{-1}·K^{-1}. The rotating drum is integrated into a test rig whose piping and instrumentation diagram is shown in Fig. 6. A water circuit flows through the rotating drum with a high mass flow rate ($\dot{m}_1$) of 1.2 kg·s^{-1}. The mass flow of flow of water is provided by a submersible pump. This decreases the temperature difference of the water between the inlet (T_1) and the outlet (T_2) of the drum to below 1 K to reach an almost

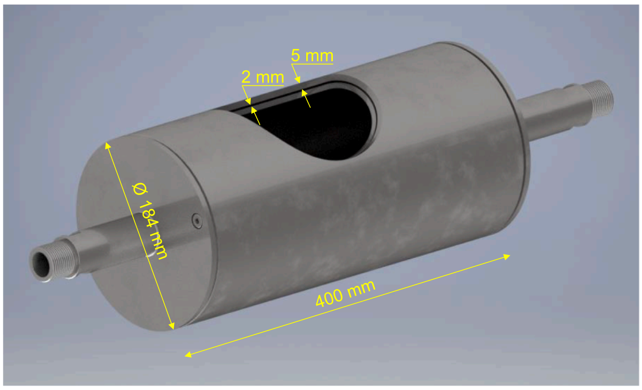

Fig. 5. Geometrical properties of the rotating drum.

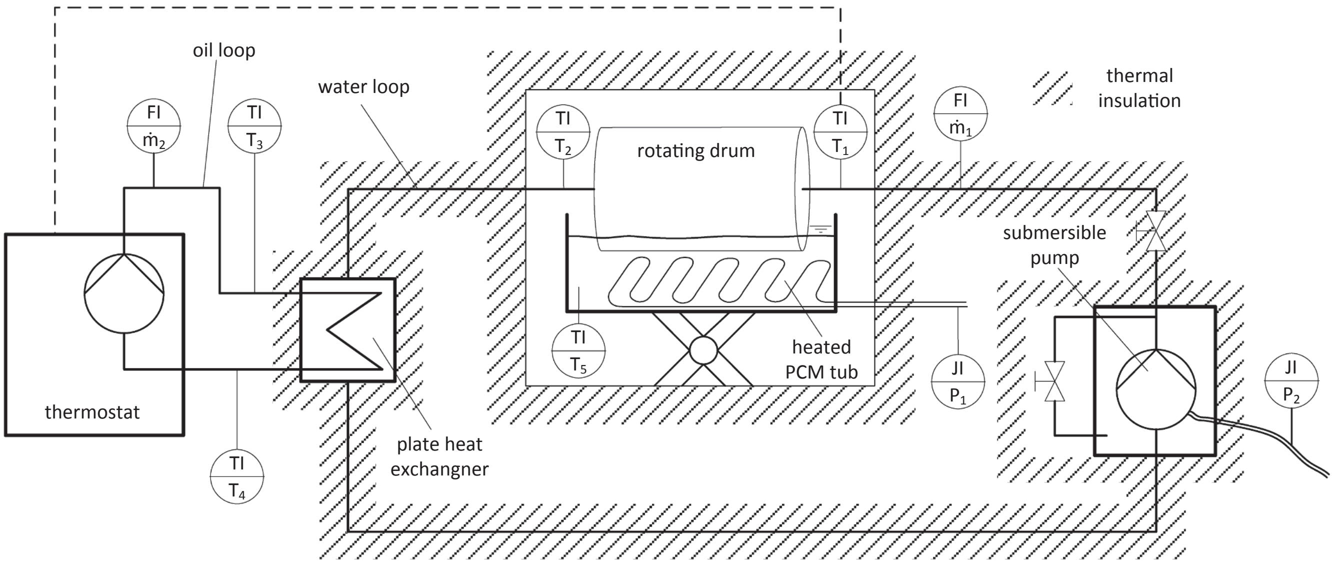

Fig. 6. Piping and instrumentation diagram of the test rig.

isothermal process along the rotating drum. Furthermore, the annular gap inside the rotating drum increases the flow velocity of the water to 1.1 m·s^{-1} which results in an increased convective heat transfer between the steel drum and the water. The convective heat transfer coefficient can be estimated to 4176 W·m^{-2}·K^{-1} according to [25]. The water circuit is cooled by a thermal oil circuit with a plate heat exchanger. The thermal oil circuit is cooled by a commercial thermostat which is controlled by the drums inlet temperature (T_1). The PCM is located in a tub below the rotating drum. The PCM is melted and heated by electrical heating elements inside the tub by direct contact. The tub can be lifted by a laboratory lift mounted below the tub to immerse the drum into the PCM. The rotating drum is connected to the water circuit via rotary unions supported by rotating bearings. It is driven by a stepper motor and a belt drive. The rotational speed is continuously adjustable in the range of 0–30 min^{-1}. The scraper is made of a 0.5 mm stainless steel sheet, which is tangentially pressed against the drums surface by its internal elasticity. The solidified and scraped PCM falls back into the liquid PCM tub and is re-melted by the electrical heater. This keeps the level of the PCM constant during operation. The entire water circuit is thermally insulated as well as the PCM tub and the rotating drum. Fig. 7 shows a picture of the rotating drum for different rotational speeds. Fig. 8 shows the entire test rig.

2.2. Phase change material

The use of unpressurised water as HTF requires a PCM with a phase change temperature in the range of 0–100 °C. In the temperature range between 20 and 75 °C, fatty acids have been prooven as suitable phase change materials [26–28]. For the solidification, the temperature of the water in the water circuit is cooled up to 10 K below the melting temperature of the PCM. To reduce its heat losses a melting point of 10 K above the ambient temperature of 22 °C is preferable. Decanoic acid, also referred to as capric acid, is selected as the PCM. The melting point is 31.5 °C [29]. It is available in high purity, non-toxic and suitable as PCM for low temperature applications [27,28]. Table 1 shows the material properties of decanoic acid.

Fig. 8. Photo of the experimental test rig.

2.3. Measurement of the heat transfer

A small to zero temperature difference between the inlet (T_1) and the

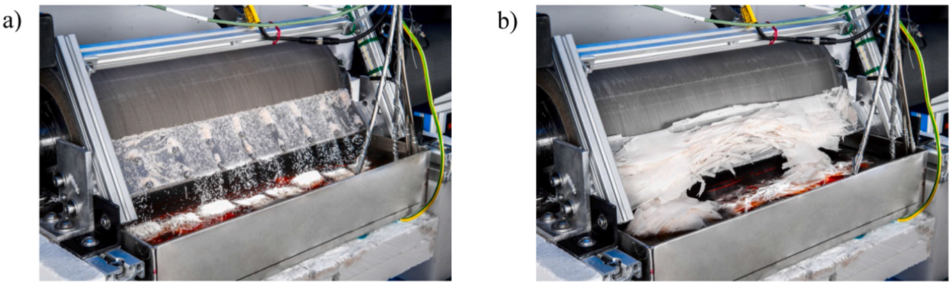

Fig. 7. Picture of the rotating drum during operation (a), a) at 6 min^{-1}, b) at 12 min$^{-1.}$

Table 1
Thermophysical properties of decanoic acid.

Description	Variable	Value	Unit	Remark	Source
Melting point	$T_{PCM,m}$	31.5	°C		[29]
Phase change enthalpy	Δh_{PCM}	153	$kJ\cdot kg^{-1}$		[29]
Thermal conductivity, liquid	$\lambda_{PCM,l}$	0.149	$W\cdot m^{-1}\cdot K^{-1}$	(at 40 °C)	[29]
Thermal conductivity, solid	$\lambda_{PCM,s}$	0.204	$W\cdot m^{-1}\cdot K^{-1}$	(at 20 °C)	[28]
Density, liquid	$\varrho_{PCM,l}$	886.3	$kg\cdot m^{-3}$	(at 37.8 °C)	[30]
Density, solid	$\varrho_{PCM,s}$	850	$kg\cdot m^{-3}$	(at 25 °C)	[28]
Viscosity	$\eta_{PCM,l}$	0.00633	$Pa\cdot s$	(at 37.8 °C)	[31]
Heat capacity, liquid	$c_{p,PCM,l}$	2.0883	$kJ\cdot kg^{-1}\cdot K^{-1}$	(at 35–65 °C)	[32]
Heat capacity, solid	$c_{p,PCM,s}$	2.0967	$kJ\cdot kg^{-1}\cdot K^{-1}$	(at 0–24 °C)	[32]

outlet (T_2) temperature of the rotating drum is aspired for a homogeneous heat transfer at the drum surface. By doing so, it is not possible to measure the transferred heat of the rotating drum directly by measuring the temperature difference between the inlet (T_1) and the outlet (T_2). Therefore, the heat transfer of the rotating drum is calculated by the energy balance of the entire water circuit.

The energy transferred by the plate heat exchanger to the water circuit can be determined with the specific heat capacity of the thermal oil $c_{p,l,oil}$, by measuring the temperature difference between inlet (T_3) and outlet (T_4) of the plate heat exchanger and the mass flow ($\dot{m}_2$) of the thermal oil, pumped through the oil circuit. The mass flow ($\dot{m}_2$) of the oil circuit is adjustable between 0.055 $kg\cdot s^{-1}$ and 0.18 $kg\cdot s^{-1}$, which is low compared to the mass flow in the water circuit ($\dot{m}_1$). This leads to an increased temperature difference between the inlet (T_3) and the outlet (T_4) of the thermal oil at the plate heat exchanger. The temperature difference of the thermal oil depends on the mass flow ($\dot{m}_2$) as well as the thermal power of the rotating drum and is in the range of 3 K up to 10 K. Since the efficiency of the used pump is unknown, a submersible pump is used. Thus, the total amount of electrical energy is dissipated to the water circuit, measured with an electrical power meter (P_2). As a result of this, the heat transferred at a steady state at the rotating drum surface is the difference between the heat extracted by the plate heat exchanger and the heat dissipated by the pump as given in Eq. (1):

$$\dot{Q}_{RD} = \dot{m}_2\cdot c_{p,Oil,l}\left(\overline{T_{3,4}}\right)\cdot(T_4 - T_3) - P_2 \tag{1}$$

The electrical energy P_1 needed to re-melt and heat the PCM in the tub is also measured by a power meter. For an ideal system with no heat losses to the ambient air and neglecting the mechanical energy transferred into the system by the stepper motor, it must apply

$$\dot{Q}_{RD} = P_1.$$

The figures in Section 3.1 showP_1. The heat losses and the mechanical energy needed for scrapping off the solidified PCM are discussed in Section 3.3 by comparing $\dot{Q}_{RD}$ and P_1.

2.4. Measurement of the layer thickness of the solid PCM

The layer thickness of the solidified PCM after the surface emerges from the liquid PCM is measured by a triangular laser distance measurement device (Type IL-S025 produced by KEYENCE). It is located shortly before the solidified layer is scraped off by the scraper and the surface is re-emerged into the liquid PCM again as shown in Fig. 9 a and b. The laser device is always measuring the distance to the PCM surface only. The layer thickness can be determined by comparing the measured distance with solidified PCM and the measured distance to the bare surface of the drum.

2.5. Experimental methodology

In the beginning of each experiment, the PCM is melted by the electrical heaters and heated to $T_{PCM,l}$. The electrical heaters are controlled by thermocouples inside the PCM. Since there is no temperature change during the phase change, the temperature of the liquid PCM $T_{PCM,l}$ has to be above the melting point because the thermocouples cannot detect the phase state of the PCM at the melting temperature. The HTF inlet temperature of the rotating drum T_1 is set to a certain value and the rotation of the drum is started. Afterwards, the immersion depth is adjusted to 24 mm, considering the displacement of liquid PCM. This corresponds to an immersion angle Θ of 85°, which is equivalent to 24% of the total shell surface of the drum. The total immerged drum shell surface is therefore 0.054 m^2. The nomenclature of the experiments consists of three figures, the total temperature difference between the liquid PCM and the HTF ($\Delta T_{PCM,l\text{-}HTF}$), the temperature difference of the solidification between the melting point of the PCM and the HTF ($\Delta T_{PCM,m\text{-}HTF}$) and the temperature difference between the liquid PCM and the melting point of the PCM ($\Delta T_{PCM,l\text{-}PCM,m}$). The temperature configuration is illustrated in Fig. 2 as well. Each temperature configuration was examined for different rotational speeds between 0.25 min^{-1} and 25 min^{-1}. As the thermal power of the thermostat used is limited to 2.2 kW and the submersible pump dissipates 0.5 kW into the HTF circuit, the maximum power that can be measured at the rotating drum is 1.7 kW. The experiments are conducted for all three operation modes shown and discussed in Section 2.6. Table 2 shows the measured temperature configurations and the nomenclature of the experiments. For a temperature of the HTF above the melting temperature of the PCM, no solidification occurs. Therefore, the temperatures differences to the PCM melting temperature $\Delta T_{PCM,m\text{-}HTF}$ and $\Delta T_{PCM,l\text{-}PCM,m}$ of the first five temperature settings given in Table 2 are not relevant. The data are measured after reaching a stationary HTF in- and outlet temperature and are recorded every second. The given data in Section 3 shows the average values during the stationary operation.

2.6. Operational modes

For a detailed investigation of the influence of the different physical effect on the heat transfer, three different operation modes are defined as shown in Fig. 9. When the drum surface emerges from the PCM bath, liquid PCM adheres to the solidified PCM layer. This adhering liquid PCM solidifies after the surface has left the liquid PCM and thus enlarges the active heat exchanger surface. With operation mode (a), the total heat transfer is measured including the additional heat transfer due to the solidification of the adhering PCM after the surface emerges from the liquid PCM. In operation mode (b), the adhering liquid is removed by a rubber lip mounted shortly after the surface emerges from the liquid PCM. Thus, the additional heat transfer from adhesion can be investigated by comparing the measured heat transfer of operation mode (a) and (b). The PCM, which solidifies at the heat exchanger surface, is cooled down below its melting point after the heat exchanger surface has left the liquid PCM. To investigate the amount of sensible heat transferred during this period, the entire PCM layer is removed shortly after the surface emerges from the liquid PCM in operation mode (c). This is done by reversing the direction of rotation and position of the scraper. As mentioned, the immerged drum shell surface is 0.054 m^2, which corresponds to the total active heat transfer surface during the operation mode (b) without adhesion. During the operation mode (c), the scraper can't be mounted directly at the emerging point of the drum due to constructive constraints. Therefore, adhering liquid PCM increases the active heat transfer surface to 0.067 m^2. For the measurements operation mode (a) with adhesion, the total drum shell surface is 0.19 m^2 from the point of immersion to the scraper. Here, the active heat exchanger surface is not exactly defined, as the adhering liquid PCM is completely

Table 2
Measurement matrix of the temperature configurations and the nomenclature of the conducted experiments.

$T_{PCM,m}$	T_{HTF}	$T_{PCM,l}$	$\Delta T_{PCM,l\text{-}HTF} =$ $T_{PCM,l}-T_{HTF}$	$\Delta T_{PCM,m\text{-}HTF} =$ $T_{PCM,m}-T_{HTF}$	$\Delta T_{PCM,l\text{-}PCM,m} =$ $T_{PCM,l}-T_{PCM,m}$	Nomenclature = $\Delta T_{PCM,l\text{-}HTF}/\Delta T_{HTF\text{-}PCM,m}/\Delta T_{PCM,l\text{-}PCM,m}$
31.5 °C	34 °C	34 °C	0 K	–	–	**0 K/-/-**
		39 °C	5 K	–	–	**5 K/-/-**
		44 °C	10 K	–	–	**10 K/-/-**
		49 °C	15 K	–	–	**15 K/-/-**
		54 °C	20 K	–	–	**20 K/-/-**
	26.5 °C	36.5 °C	10 K	5 K	5 K	**10 K/5K/5K**
		41.5 °C	15 K	5 K	10 K	**15 K/5K/10 K**
		46.5 °C	20 K	5 K	15 K	**20 K/5K/15 K**
		51.5 °C	30 K	5 K	25 K	**30 K/5K/25 K**
	21.5 °C	36.5 °C	15 K	10 K	5 K	**15 K/10 K/5K**
		41.5 °C	20 K	10 K	10 K	**20 K/10 K/10 K**

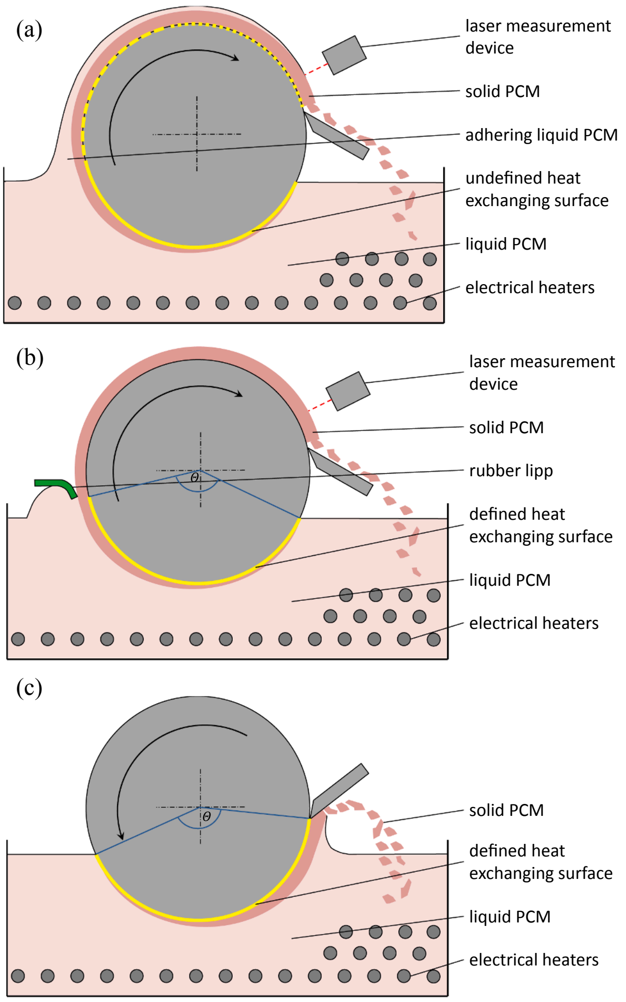

Fig. 9. Examined mode of operation (a) scraping off the solidified layer and adhering layer shortly before re-immerge into liquid PCM (b) scraping off the solidified layer shortly before re-immerge, but removing the adhering liquid layer by a rubber lip shortly after the surface emerged the liquid PCM (c) scraping off the solidified layer shortly after the surface has emerged from the liquid PCM.

solidified for low rotational speeds bevor it reaches the scraper. The total shells surface of the rotating drum is 0.23 m^2.

2.7. Uncertainty analysis

The directly applicable uncertainty of the power meter used to measure the heat transfer of the rotating drum is given as ±2%. The laser sensor which is used for the determination of the layer thickness has a linearity of 0.1% and a repeatability of 1 µm. As both values are very low, no error bars are given in the figures in Section 3. One has to consider that the overall uncertainty is depending of external reasons which are not able to quantify directly. First of all, the temperature of the liquid PCM is measured by several thermocouples within the liquid PCM with an uncertainty of 1.5 K. Furthermore, the immersion depth of the rotating drum is variating by ±4 mm. As a result of this, the immersed shell surface is variating by ±2%. The repeatability for the heat transfer has been measured within pre-experiments where the heat transfer has been measured up to four times with the same configuration. The standard deviation calculated according to [33] is ±54 W for the measured different rotational speeds between 0.25 min^{-1} and 15 min^{-1}.

3. Experimental results and discussion

The experimental data are shown and discussed in the following section. For the heat transfer at the rotating drum, the electrically measured data P_1 for heating the liquid PCM in the tub are presented. The heat transfer $\dot{Q}_{RD}$ is used for determining the heat losses and the mechanical power required for scraping the PCM off the drum. This is discussed in Section 3.3.

3.1. Heat transfer at the rotating drum

The influence of the temperature configuration and the operational mode on the heat transfer will be discussed within this section. While the data of operation mode (b) and (c) are measured in the range from 0 min^{-1} to 25 min^{-1}, the data of operation mode (a) are only measured for lower rotational speeds due to the limited thermal power of the thermostat used, as described in Section 2.5.

3.1.1. Convective heat transfer without solidification

By rotating the drum in liquid PCM with a HTF temperature $T_{PCM,l}$ above the melting temperature of the PCM, no solidification occurs. The measured data are given in Fig. 10 for different rotational speeds and different temperature differences between the liquid PCM and the HTF. No data has been measured by using the rubber lip operation mode (b), as the heat transfer phenomena is the same as the operation mode (c). The progression of the heat transfer is almost linear. With higher rotational speeds the increase of the heat transfer flattens out slightly. So, the average increase of the data without adhesion is 27 W/min^{-1} in the range from 0 min^{-1} to 5 min^{-1} and 13 W/min^{-1} in the range from 20 min^{-1} to 25 min^{-1}. The heat transfer of the measurements with adhesion is higher than the heat transfer of the measurements without adhesion. While the measured heat transfer with adhesion exceeds the data without adhesion in average by 12% at 2 min^{-1}, the increase is 10% at a rotational speed of 10 min^{-1}. With no rotation, the shown heat transfer bases on natural convection of the liquid PCM. For no temperature

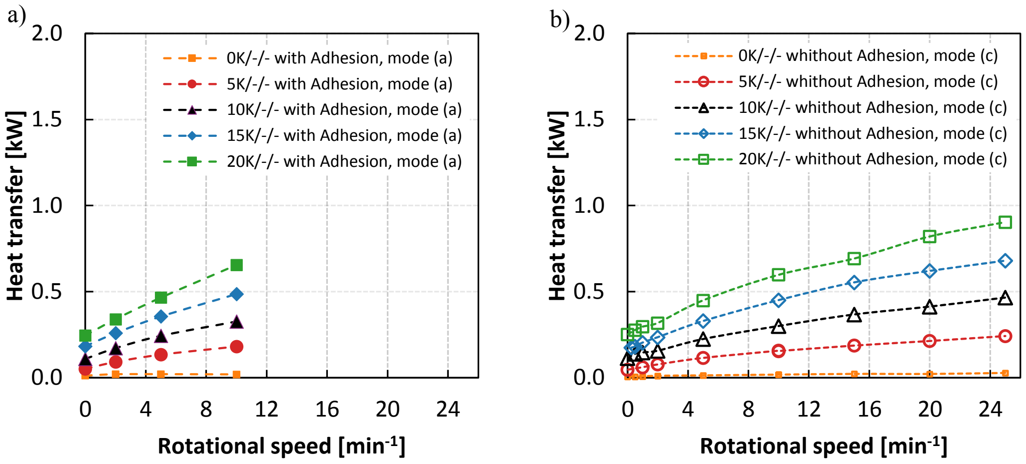

Fig. 10. Measured heat transfer at the rotating drum for pure convective heat transfer without solidification a) with Adhesion, b) without Adhesion.

difference between the liquid PCM and the HTF, the measured heat flow increases from 7 W at 0 min^{-1} to 29 W at 25 min^{-1}. This is explained by increasing heat losses to the ambient due to an increased circulation of the air inside the insulation.

3.1.2. Influence of the temperature difference $\Delta T_{PCM,m\text{-}HTF}$

By decreasing the HTF temperature in the water circuit below the PCMs melting temperature, liquid PCM solidifies at the drums surface. In Fig. 11 the measured heat transferred to the rotating drum is given for a common total temperature difference between the HTF and the liquid PCM temperature $\Delta T_{PCM,l\text{-}HTF}$ of 20 K. Thereby, the temperature difference between the HTF temperature and the melting temperature of the PCM $\Delta T_{PCM,m\text{-}HTF}$ is varied. The measurement of the heat transfer with solidification starts at a rotational speed of 0.25 min^{-1} as there are no stationary data available for no rotation. The heat transfer is increasing by an increase of $\Delta T_{PCM,m\text{-}HTF}$. So, doubling $\Delta T_{PCM,m\text{-}HTF}$ from 5 K to 10 K increases the heat transfer by 31% in average. Compared to the measurements without solidification, the average increase of the heat transfer is 46% for a $\Delta T_{PCM,m\text{-}HTF}$ of 5 K and 77% for a $\Delta T_{PCM,m\text{-}HTF}$ of 10 K while the increase is higher for increasing rotational speeds. The increase of the heat transfer when increasing the rotational speed flattens out at higher rotational speeds. So, the average increase is 195 W/min^{-1} with adhesion and 180 W/min^{-1} without adhesion in the range between 0.25 min^{-1} to 2 min^{-1} compared to 96 W/min^{-1} with adhesion and 63 W/min^{-1} without adhesion when increasing the rotational speed from 5 min^{-1} to 8 min^{-1}. At rotational speeds below 0.5 min^{-1}, the pure convective heat transfer exceeds the heat transfer during solidification for these rotational speeds. This is a consequence of the reduced heat transfer through to the solidified PCM layer in comparison to purely convective heat transfer at the bare surface.

3.1.3. Influence of the PCM temperature difference $\Delta T_{PCM,l\text{-}PCM,m}$

By increasing the temperature difference of the liquid PCM temperature and the melting temperature of the PCM $\Delta T_{PCM,l\text{-}PCM,m}$ at a constant temperature difference between the HTF and the melting temperature of the PCM $\Delta T_{PCM,m\text{-}HTF}$, the transferred heat is increased as shown in Fig. 12. The average increase of the heat transfer is 7% for an increase of $\Delta T_{PCM,l\text{-}PCM,m}$ from 10 K to 15 K and 28% for an increase of $\Delta T_{PCM,l\text{-}PCM,m}$ from 15 K to 25 K. Thus, an increase of $\Delta T_{PCM,l\text{-}PCM,m}$ increases the heat transfer at the rotating drum significantly less than an increase of $\Delta T_{HTF\text{-}PCM,m}$. By an increasing rotational speed, the progression of the heat transfer flattens out as well. Thus, the average increase is 157 W/min^{-1} with adhesion and 139 W/min^{-1} without adhesion in the range between 0.25 min^{-1} to 2 min^{-1} compared to 51 W/min^{-1} with adhesion and 37 W/min^{-1} without adhesion when increasing the rotational speed from 10 min^{-1} to 13 min^{-1}.

3.1.4. Influence of the adhesion and the solidified PCM layer

The heat transfer at the rotating drum varies with the mode of operation (see Fig. 9) as shown in Fig. 13. The heat transfer is lowest

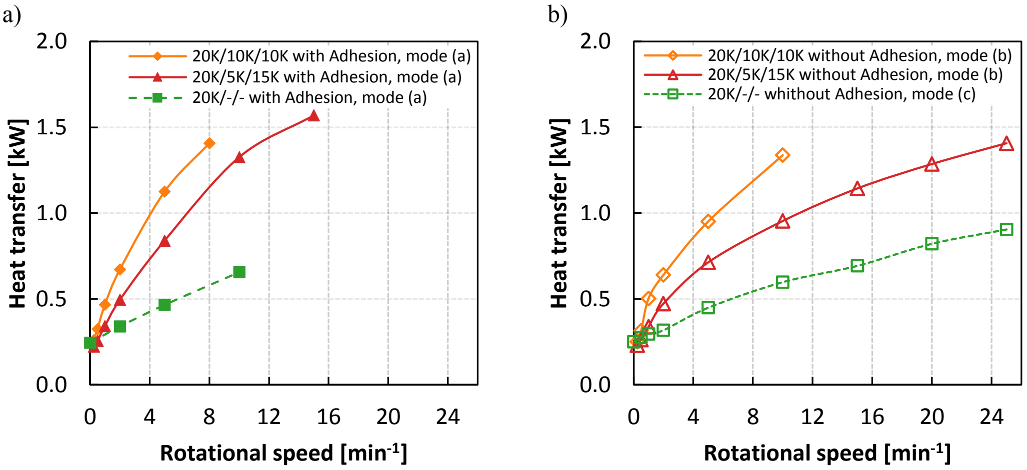

Fig. 11. Measured heat transfer at the rotating drum at a common total temperature difference of 20 K and a variation of the temperature difference between the HTF and the PCM melting point a) with Adhesion, b) without Adhesion.

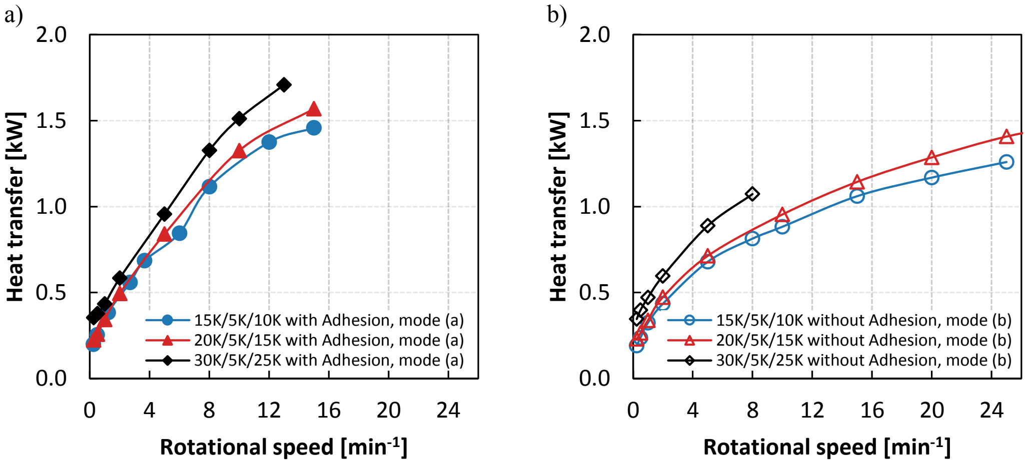

Fig. 12. Measured heat transfer at the rotating drum at a common temperature difference between the HTF and the melting temperature of the PCM $\Delta T_{PCM,m\text{-}HTF}$ and a variation of the temperature difference between the HTF and the PCM melting point $\Delta T_{PCM,l\text{-}PCM,m}$ a) with Adhesion, b) without Adhesion.

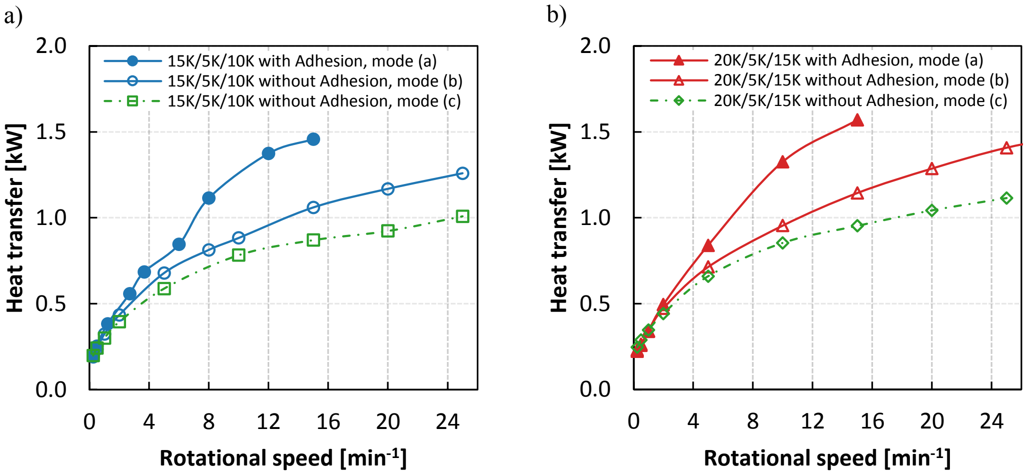

Fig. 13. Measured heat transfer at the rotating drum for common temperature difference configuration of a) 15 K/5K/10 K and b) 20 K/5K/15 K and a variation of the operation mode (see Fig. 9).

when scraping off the adhering and solidified layer shortly after the drums surface emerges from the liquid PCM (operation mode (c)). The heat transfer is increased by 30% in average when removing the adhering liquid layer shortly after the drums surface emerges from the liquid PCM, but scraping off the solidified PCM layer just before the surface re-immerses into the PCM (operation mode (b)). This increase is consistent for all rotational speeds. It can be explained in the way that the solidified layer is cooled below its melting point after the solid PCM has left the liquid PCM. Thus, the additional heat flow is the sensible heat within the solidified PCM layer. The adhering layer increases the heat transfer further by 45% in average. This is because the active solidification surface of the rotating drum is enlarged as liquid PCM solidifies also after the surface has emerged the liquid PCM. Within the range of 0.25 $\min^{-1}$ and 10 $\min^{-1}$, this increase of the additional heat transfer due to adhesion is increasing with higher rotational speeds. A further increase of the rotational speeds results in a consistent increase of 60% in average for the rage between 10 $\min^{-1}$ and 15 $\min^{-1}$. This is because the adhering liquid PCM is not totally solidified when it reaches the scraper for rotational speeds of 10 $\min^{-1}$ and above.

3.2. Layer thickness of PCM at the rotating drum

The layer thickness of the solidified PCM layer is measured with and without the influence of the adhesion (operation modes (a) and (b) in Fig. 9). The additional layer thickness due to the adhesion can be determined by the difference of these both measurements. The experimental results are shown in Fig. 14. The layer thickness varies with the temperature difference of both $\Delta T_{HTF\text{-}PCM,m}$ and $\Delta T_{PCM,l\text{–}PCM,m}$. By increasing $\Delta T_{PCM,m\text{-}HTF}$ from 5 K to 10 K at a constant total temperature difference $\Delta T_{PCM,l\text{-}HTF}$ of 20 K, the average total layer thicknesses is increased by a factor of 1.5 while the average layer thickness without adhesion is increased by a factor of 2.7 in average. In the same way, the calculated adhering layer remains almost constant and is decreased by only 15% in average. By increasing $\Delta T_{PCM,l\text{-}PCM,m}$ at constant $\Delta T_{PCM,m\text{-}HTF}$, the solidified PCM layers are decreased. So, the layer thickness without adhesion is decreased by 33% in average when increasing $\Delta T_{PCM,l\text{-}PCM,m}$ from 10 K to 15 K and 40% in average when increasing $\Delta T_{PCM,l\text{-}PCM,m}$ from 15 K to 25 K. The total layer thickness decreases at low rotational speeds more than at high rotational speeds. The average decrease is 24% and 41% for a change of $\Delta T_{PCM,l\text{-}PCM,m}$ from 10 K to 15 K and 15 K to 25 K at a rotational speed between 0.25 $\min^{-1}$ and 10 $\min^{-1}$ while the average decrease is only 4% and 7% at a rotational speed between 12 $\min^{-1}$ and 25 $\min^{-1}$. The calculated adhering layer remains nearly unchanged over the whole range of the rotational speed for the same change in temperature. The average change is below 0.01 mm. The measured total layer thicknesses at a $\Delta T_{PCM,m\text{-}HTF}$ of 5 K have a local

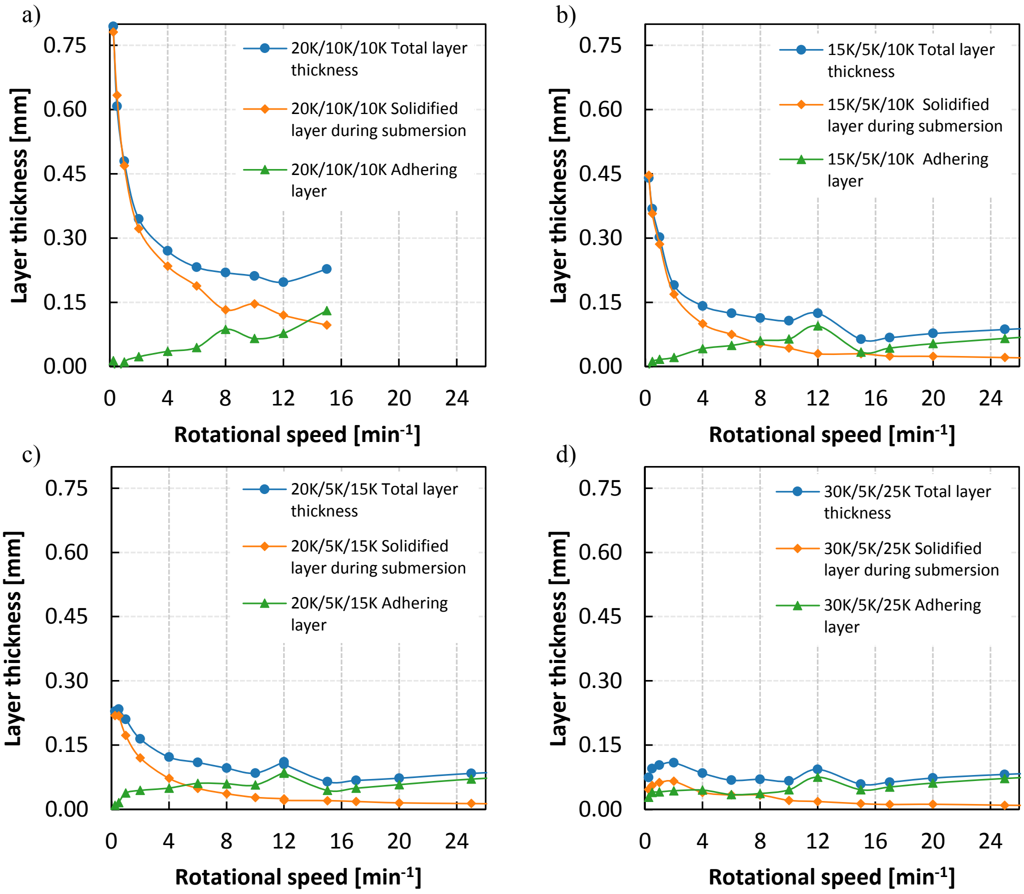

Fig. 14. Measured total layer thicknesses, measured layer thicknesses during submersion and resulting calculated adhering layer thicknesses at the rotating drum surface for different temperature configurations.

maximum at 12 min^{-1}. For rotational speeds of 12 min^{-1} and above, adhering liquid PCM is removed by the scraper together with the solidified PCM. At rotational speeds of 15 min^{-1} and more, the laser measuring device does not measure clear data. While it can be assumed that the solidified layer under the adherent liquid PCM decreases at higher rotational speeds, it can be assumed that the adherent liquid layer increases.

3.3. *Mechanical power to remove the solidified PCM*

By comparing the measured electrical power to re-melt and heat the PCM tub P_1 and the thermal power measured at the plate heat exchanger $\dot{Q}_{RD}$, the heat losses and the mechanical power needed to remove the solidified PCM from the drums surface can be estimated. The difference of these both values is given in Fig. 15 exemplarily for six measurements.

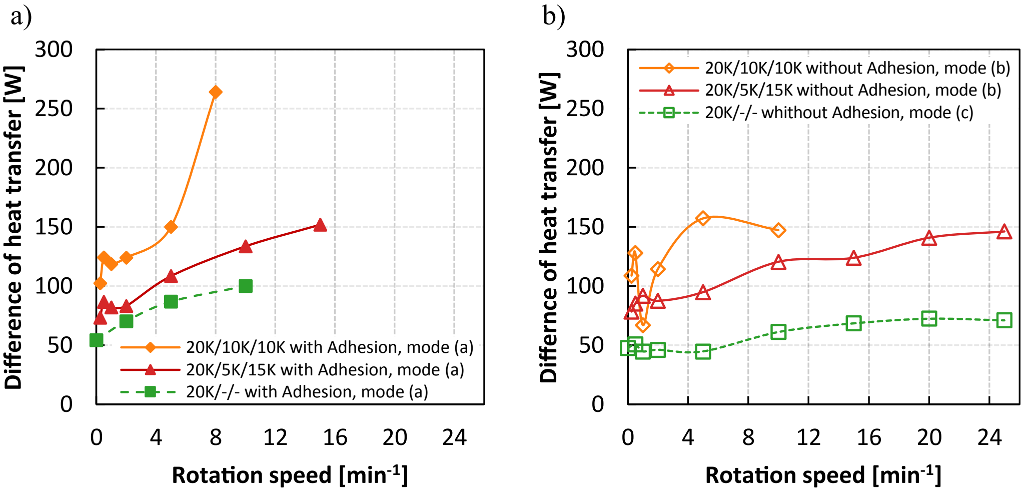

Fig. 15. Difference between the measured electrical power P_1 and the thermal power determinate at the plate heat exchanger $\dot{Q}_{RD}$.

As the mechanical energy has to be extracted from the water circuit, the values of $\dot{Q}_{RD}$ exceeds the values of P_1. The lowest measured values refer to the measurement without solidification at standstill and amount to 50 W. As there is no mechanical energy dissipated into the system, this is the heat loss to the ambient. Thereby, the losses can be differed into losses at the rotating drum insulation and at the water circuit. The losses at the rotating drum can be determined with the data given in Fig. 10 for no temperature difference $\Delta T_{PCM,l\text{-}HTF}$ between the HTF and the liquid PCM. The losses are increasing with the rotational speed from 7 W at 0 min^{-1} to 29 W at 25 min^{-1}. The additional losses have to be at the water circuit. With an increase of the rotational speed, the difference of the measured values given in Fig. 15 increases also for no solidification. This increase is due to friction at the bare surface and the scraper and within the rotary bearings. Its maximum of 48 W can be found at 10 min^{-1} for the measurement with adhesion. When solidification occurs, the difference of the values to the heat loss of 50 W refers to both, the friction and the mechanical power needed for scraping off the solidified PCM. The average additional power is 44 W for a temperature configuration of 20 K/5K/15 K and 79 W for a temperature configuration of 20 K/10 K/10 K. For the measurements with adhesion, the increase is 17% higher in average compared to the measurements without adhesion. The mechanical power due to friction and scraping off the solidified PCM increases with higher rotational speeds. The maximum mechanical power is 100 W for a temperature configuration of 20 K/5K/15 K and 215 W for a temperature configuration of 20 K/10 K/10 K. When comparing the mechanical power due to friction and for scraping off the PCM from the drum surface with the thermal power, the value decreases with higher rotational speeds. Thus, the average mechanical power is 8% of the thermal power at 5 min^{-1} and decreases below 5% at 15 min^{-1}. Be aware that the experimental test rig is not optimized for low mechanical power consumption.

3.4. Heat transfer density at the rotating drum surface

By relating the measured heat transfer to a specific surface, the heat transfer potential can be compared with other heat exchange technologies. Since the active heat transfer surface is not clearly defined at the rotating drum, the measured heat transfer is related to the submerged drum shell surface and the total drum shell surface. The results are given Fig. 16.When relating the measured heat transfer with adhesion to the submerged surface only, a heat transfer density of up to 28.8 $kW\cdot m^{-2}$ at a rotational speed of 15 min^{-1} is determined. Since the heat transfer surface is expanded by the adhesion to the surface outside the liquid PCM as well, the heat transfer density related to the total drum surface is more expressive. This results in a heat transfer density of up to 6.8 $kW\cdot m^{-2}$. When removing the liquid adhering layer with the rubber lip, the heat transfer density is 21 $kW\cdot m^{-2}$ at 15 min^{-1} and 25.8 $kW\cdot m^{-2}$ at 25 min^{-1} when relating the measured heat transfer to the submerged drum shell surface. When relating the measured heat transfer to the total drum shell surface, the heat transfer densities are 4.9 $kW\cdot m^{-2}$ and 6.1 $kW\cdot m^{-2}$. These values are for the specific experimental test rig. An optimized system will reach higher surface specific heat transfer rates as mentioned in Section 4.

4. Conclusion and outlook

In order to increase the predictability of steam generated from fluctuating renewable energy for industrial processes as well as for power plants, LHTES are particularly suitable due to the isothermal phase change during melting and solidification. The deliverable thermal power of all state-of-the-art passive LHTES is decreasing during the discharge process due to a growing insulation layer out of solidified PCM at the heat exchanger surface. Furthermore, passive LHTES have a fixed ratio between power and capacity as the amount of PCM is fixed to the size of the heat transfer structure. The introduced and experimentally demonstrated rotating drum heat exchanger for LHTES overcomes this limitation by a continuously scraped heat exchanger surface. The novelty compared to already known active LHTES concepts is the consistent minimization of the thickness of the solidified PCM layer. This increases the heat transfer to a maximum. By changing the rotational speed, the thermal power output can be controlled. Thus, a specific characteristic curve of the thermal power output of the system in dependence of the rotational speed can be given. The commissioned experimental test rig using the low temperature PCM decanoic acid and water as HTF serves as a proof-of-concept. The scraper, made out of a metal sheet pressed against the drums surface, works smoothly.

The measured transferred heat is constant at consistent rotational speeds and temperature differences and can be increased by increasing the rotational speed. The measured heat transfer at the presented test rig is up to 1.6 kW for a total temperature difference between the HTF and the liquid PCM $\Delta T_{PCM,l\text{-}HTF}$ of 20 K. Compared to the heat transfer at pure forced convection without solidification, the heat transfer is up to 142% higher when solidification occurs at a constant total temperature difference $\Delta T_{PCM,l\text{-}HTF}$ and constant rotational speed. During solidification, a rise of the temperature difference between the HTF and the melting point of the PCM $\Delta T_{PCM,m\text{-}HTF}$ by 5 K increases the transferred heat by 31% in average while a rise of the temperature difference between the melting point of the PCM and the temperature of the liquid PCM $\Delta T_{PCM,l\text{-}PCM,m}$ increases the heat transfer by only 11% in average. When the surface of the rotating drum emerges from the liquid PCM, liquid PCM adheres at the solidified layer. This increases the total heat transfer by up to 60% as the liquid PCM solidifies after the surface emerged. The total measured layer thicknesses, composed out of a solidified part and an adhering part, decrease with higher rotational

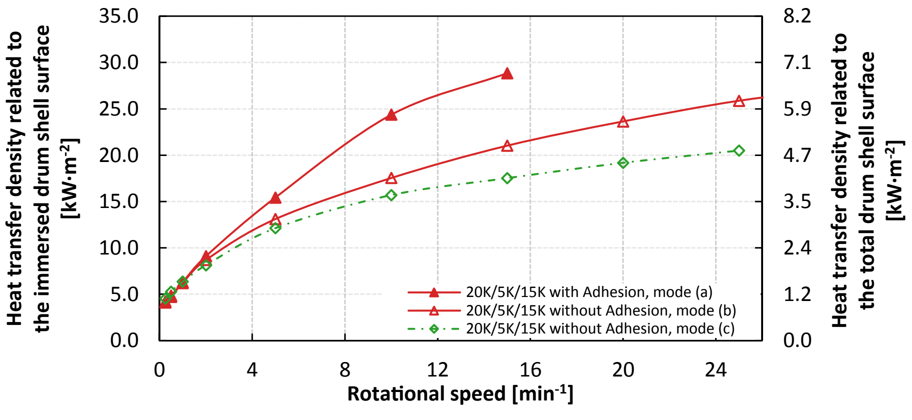

Fig. 16. Heat transfer densities related to the immersed drum shell surface (left axis) and the total drum shell surface (right axis) at the rotating drum for a temperature configuration of 20 K/15 K/5K and a variation of the operation modes.

speeds. Thus, total layer thicknesses of below 0.05 mm can be achieved.

In a next step, an analytical and numerical scheme to investigate the un-steady effects and the adhesion will complement the experimental results. The authors are working on several models right now and will publish the results soon. The theoretical models will be validated with the presented experimental results. When using sodium nitrate as PCM and a temperature difference between the melting point of the PCM and evaporating water as heat transfer fluid of 50 K, first calculations with the model show heat transfer densities of above 100 kW·m^{-2} based on the total drum surface. Furthermore, the authors are planning an experimental test of the rotating drum heat exchanger with a thermal power of 100 kW. It will be integrated into an entire heat storage system using a high temperature PCM for the generation of steam.

Funding

This research did not receive any specific grant from funding agencies in the public, commercial, or not-for-profit sectors.

CRediT authorship contribution statement

Jonas Tombrink: Conceptualization, Methodology, Investigation, Validation, Visualization, Writing - original draft. **Henning Jockenhöfer:** Conceptualization, Writing - review & editing. **Dan Bauer:** Conceptualization, Funding acquisition, Supervision, Writing - review & editing.

Declaration of Competing Interest

The authors declare that they have no known competing financial interests or personal relationships that could have appeared to influence the work reported in this paper.

References

[1] T. Naegler, S. Simon, M. Klein, H.C. Gils, Quantification of the European industrial heat demand by branch and temperature level, Int. J. Energ. Res. 39 (2015) 2019–2030, https://doi.org/10.1002/er.3436.

[2] H. Jockenhöfer, W.-D. Steinmann, D. Bauer, Detailed numerical investigation of a pumped thermal energy storage with low temperature heat integration, Energy 145 (2018) 665–676, https://doi.org/10.1016/j.energy.2017.12.087.

[3] T. Bauer, D. Laing, R. Tamme, Characterization of Sodium Nitrate as Phase Change Material, Int. J. Thermophys. 33 (2012) 91–104, https://doi.org/10.1007/s10765-011-1113-9.

[4] J. Vogel, J. Felbinger, M. Johnson, Natural convection in high temperature flat plate latent heat thermal energy, Appl. Energ. 184 (2016) 184–196, https://doi.org/10.1016/j.apenergy.2016.10.001.

[5] S.Q. Zhang, L. Pu, L.L. Xu, R. Liu, Y.Z. Li, Melting performance analysis of phase change materials in different finned thermal energy storage, Appl. Therm. Eng. 176 (2020), 115425, https://doi.org/10.1016/j.applthermaleng.2020.115425.

[6] Z. Ma, W.-W. Yang, F. Yuan, B. Jin, Y.-L. He, Investigation on the thermal performance of a high-temperature latent heat storage system, Appl. Therm. Eng. 122 (2017) 579–592, https://doi.org/10.1016/j.applthermaleng.2017.04.085.

[7] M. Johnson, J. Vogel, M. Hempel, B. Hachmann, A. Dengel, Design of high temperature thermal energy storage for high power levels, Sustain. Cities Soc. 35 (2017) 758–763, https://doi.org/10.1016/j.scs.2017.09.007.

[8] M. Opolot, C. Zhao, M. Liu, S. Mancin, F. Bruno, K. Hooman, Influence of cascaded graphite foams on thermal performance of high temperature phase change material storage systems, Appl. Therm. Eng. 180 (2020), 115618, https://doi.org/10.1016/j.applthermaleng.2020.115618.

[9] W. Lin, W. Zhang, Z. Ling, X. Fang, Z. Zhang, Experimental study of the thermal performance of a novel plate type heat exchanger with phase change material, Appl. Therm. Eng. 178 (2020), 115630, https://doi.org/10.1016/j.applthermaleng.2020.115630.

[10] A. Raul, M. Jain, S.K. Gaikwad, S. Saha, Modelling and experimental study of latent heat thermal energy storage with encapsulated PCMs for solar thermal applications, Appl. Therm. Eng. 143 (2018) 415–428, https://doi.org/10.1016/j.applthermaleng.2018.07.123.

[11] M.A. Kibria, M.R. Anisur, M.H. Mahfuz, R. Saidur, I.H.S.C. Metselaar, A review on thermophysical properties of nanoparticle dispersed phase change materials, Energ. Convers. Manage. 95 (2015) 69–89, https://doi.org/10.1016/j.enconman.2015.02.028.

[12] L.S. Tariq, H.M. Ali, M.A. Akram, M.M. Janjua, M. Ahmadlouydarab, Nanoparticles enhanced phase change materials (NePCMs)-a recent review, Appl. Therm. Eng. 176 (2020), 115305, https://doi.org/10.1016/j.applthermaleng.2020.115305.

[13] X. Huang, C. Zhu, Y. Lin, G. Fang, Thermal properties and applications of microencapsulated PCM for thermal energy storage: a review, Appl. Therm. Eng. 147 (2019) 841–855, https://doi.org/10.1016/j.applthermaleng.2018.11.007.

[14] J. Giro-Paloma, M.F. Martinez, L. Cabeza, A.I. Fernandez, Types, methods, techniques, and applications for microencapsulated phase change materials (MPCM): a review, Renew. Sust. Energ. Rev. 53 (2016) 1059–1075, https://doi.org/10.1016/j.rser.2015.09.040.

[15] Y. Jiang, M. Liu, Y. Sun, Review on the development of high temperature phase change material composites for solar thermal energy storage, Sol. Energ. Mat. Sol. C 203 (2019), 110164, https://doi.org/10.1016/j.solmat.2019.110164.

[16] J. Tombrink, H. Jockenhöfer, D. Bauer, Examination of the heat transfer potential of an active latent heat storage concept, Eurotherm Seminar n°112 - Advances in Thermal Energy Storage. Lleida, 2019.

[17] V. Zipf, N. Anton, W. Daniel, N. Peter, G. Stefan, P. Werner, High temperature latent heat storage with a screw heat exchanger: design of prototype, Appl. Energ. 109 (2013) 462–469, https://doi.org/10.1016/j.apenergy.2012.11.044.

[18] H. Pointner, W.-D. Steinmann, Experimental demonstration of an active latent heat storage concept, Appl. Energ. 168 (2016) 661–671, https://doi.org/10.1016/j.apenergy.2016.01.113.

[19] U. Nepustil, D. Laing-Nepustil, D. Lodemann, R. Sivabalan, V. Hausmann, High temperature latent heat storage with direct electrical charging – second generation design, Energy Proc. 99 (2016) 314–320, https://doi.org/10.1016/j.egypro.2016.10.121.

[20] N. Maruoka, T. Tsutsumi, A. Ito, M. Hayasaka, H. Nogami, Heat release characteristics of a latent heat storage heat exchanger by scraping the solidified phase change material layer, Energy 205 (2020), 118055, https://doi.org/10.1016/j.energy.2020.118055.

[21] M.B. Lakhdar, R. Cerecero, G. Alvarez, J. Guilpart, D. Flick, A. Lallemand, Heat transfer with freezing in a scraped surface heat exchanger, Appl. Therm. Eng. 25 (2005) 45–60, https://doi.org/10.1016/j.applthermaleng.2004.05.007.

[22] L. Saraceno, G. Boccardi, G.P. Celata, R. Lazzarini, R. Trinchieri, Development of two heat transfer correlations for a scraped surface heat exchanger in an ice-cream machine, Appl. Therm. Eng. 31 (2011) 4106–4112, https://doi.org/10.1016/j.applthermaleng.2011.08.022.

[23] C. Marizy, A. Le Bail, J.C. Duprat, Y. Reverdy, Modelling of a drum freezer. Application to the freezing of mashed broccoli, J. Food Eng. 37 (1998) 305–322, https://doi.org/10.1016/S0260-8774(98)00052-1.

[24] C.S. Rao, R.W. Hartel, Scraped surface heat exchangers, Crit. Rev. Food Sci. Nutr. 46 (2006) 207–219, https://doi.org/10.1080/10408390500315561.

[25] VDI Heat Atlas, Berlin Heidelberg: Springer-Verlag; 2010.

[26] H. Nazir, M. Batool, M. Ali, A. Kannan, Fatty acids based eutectic phase change system for thermal energy storage applications, Appl. Therm. Eng. 142 (2018) 466–475, https://doi.org/10.1016/j.applthermaleng.2018.07.025.

[27] Y. Yuan, N. Zhang, W. Tao, X. Cao, Y. He, Fatty acids as phase change materials: a review, Renew. Sust. Energ. Rev. 29 (2014) 482–498, https://doi.org/10.1016/j.rser.2013.08.107.

[28] S. Kahwaji, M.B. Johnson, A.C. Kheirabadi, D. Groulx, M.A. White, Fatty acids and related phase change materials for reliable thermal energy storage at moderate temperatures, Sol. Energ. Mat. Sol. C 167 (2017) 109–120, https://doi.org/10.1016/j.solmat.2017.03.038.

[29] A. Abhat, Low temperature latent heat thermal energy storage heat storage materials, Sol. Energy 30 (1983) 313–332, https://doi.org/10.1016/0038-092X(83)90186-X.

[30] H. Noureddini, B.C. Teoh, L.D. Clements, Densities of vegetable oils and fatty acids, J. Am. Oil Chem. Soc. 69 (1992) 1184–1188, https://doi.org/10.1007/BF02637677.

[31] H. Noureddini, B.C. Teoh, L.D. Clements, Viscosities of vegetable oils and fatty acids, J. Am. Oil Chem. Soc. 69 (1992) 1189–1191, https://doi.org/10.1007/BF02637678.

[32] D. Rozanna, T.G. Chuah, A. Salmiah, T.S.Y. Choong, M. Sa'ari, Fatty acids as phase change materials (PCMs) for thermal energy storage: a review, Int. J. Green Energy 1 (2004) 495–513, https://doi.org/10.1081/GE-200038722.

[33] J.R. Taylor, An Introduction to Error Analysis: The Study of Uncertainties in Physical Measurements, University Science Books, Sausalito, California, 1997.

3.2 Paper II: Simulation of the heat exchanger

This article was published in *Applied Thermal Engineering*, 194, 117029, Copyright Elsevier (2021)

https://doi.org/10.1016/j.applthermaleng.2021.117029

Applied Thermal Engineering 194 (2021) 117029

Contents lists available at ScienceDirect

Applied Thermal Engineering

journal homepage: www.elsevier.com/locate/apthermeng

Simulation of a rotating drum heat exchanger for latent heat storage using a quasistationary analytical approach and a numerical transient finite difference scheme

Jonas Tombrink *, Dan Bauer

German Aerospace Center (DLR), Institute of Engineering Thermodynamics, Pfaffenwaldring 38-40, 70569 Stuttgart, Germany

ARTICLE INFO

Keywords:
Active latent heat thermal energy storage
Rotating drum
Solidification
Time varied finite difference method
Quasistationary calculation
Phase change material

ABSTRACT

With the concept of the rotating drum heat exchanger, latent heat can be released with a high and constant surface specific heat flux. Phase change material (PCM) solidifies on the outer surface of a drum, which is steadily removed by a fixed scraper during rotation. Two novel calculation approaches for determining the heat transfer and the layer thickness for a rotating drum heat exchanger are developed and validated with existing experimental data. This includes the identification of correlations for the thickness of the adhering liquid layer after the surface emerges from the liquid PCM and the local surface coefficient of heat transfer on the outside of a partially immersed rotating drum. While a calculation approach based on the quasistationary simplification underestimates the experimentally measured heat transfer for rotational speeds above 4 min^{-1} by 31% on average, a detailed transient numerical simulation based on a time-varying finite difference scheme reproduces the experimentally measured heat transfer with an accuracy of 8% on average. By applying the transient numerical simulation to a rotating drum heat exchanger using sodium nitrate as the PCM, a surface specific heat transfer based on the entire drum surface of up to 400 $\mathrm{kW \cdot m^{-2}}$ can be assumed, showing the high potential of the rotating drum heat exchanger for industrial and power plant applications.

1. Introduction

With latent heat thermal energy storages, thermal energy can be stored with increased storage density by utilizing the phase change of a phase change material (PCM), typically from liquid to solid state. During the discharge process of latent heat thermal energy storages, a layer of solidified PCM grows on the heat exchanger wall. Since the thermal conductivity of most cost-effective PCM is low, the growing solidified layer decreases the heat transfer depending on the state of discharge. This results in a time–dependent heat transfer during the discharge process. Beside other concepts summarized in [1], the concept of the rotating drum heat exchanger overcomes this limitation by a continuously scraped surface. The principle of the rotating drum heat exchanger is shown in Fig. 1. Fig. 2 shows a picture of the experimental test rig examined in [1], which also served as prove of concept. Thereby, a rotating drum is partially immersed in liquid PCM. A heat transfer fluid (HTF) passes through the inner side of the drum and extracts thermal energy from the outer PCM. The HTF can be either a single-phase fluid but rather an evaporating fluid. If the temperature of the HTF is below the melting point of the PCM used, the liquid PCM solidifies on the outside of the drum. The solidified PCM is moved out of the liquid PCM by the rotation of the drums surface and scraped off by a stationary scraper. The scraped PCM can be stored in a separate tank to achieve a complete separation of the power and capacity of the storage system. At the point of emergence, liquid PCM adheres to the surface, which solidifies after the surface has left the liquid PCM, as shown in Fig. 3. This increases the surface area where solidification occurs. In the case of an HTF temperature above the melting temperature of the PCM, the rotating drum can also be used for the purely convective transfer of sensible heat. In this case, no solidification occurs. The concept is introduced and described in full detail in [1] and [2]. Compared to state-of-the-art two-tank molten salt storage systems commonly used in large scale Concentrated Solar Power Plants, the storage density of a storage system based on the rotating drum can be increased by the phase change enthalpy of the storage material. Thus, compared to a sensible molten salt thermal energy storage using pure sodium nitrate as storage material in the temperature range between 350 °C and 550 °C, the demand of storage material can be reduced by about 40% when utilizing the phase change enthalpy as well as the temperature range from the melting temperature at 306 °C up to 550 °C [3]. This results in a cost reduction of both the storage

---

* Corresponding author.
E-mail address: jonas.tombrink@dlr.de (J. Tombrink).

https://doi.org/10.1016/j.applthermaleng.2021.117029
Received 12 February 2021; Received in revised form 14 April 2021; Accepted 25 April 2021

Nomenclature

Latin

a	thermal diffusivity, $[a] = \mathrm{m}^2 \cdot \mathrm{s}^{-1}$
c_p	heat capacity at constant pressure, $[c_\mathrm{p}] = \mathrm{J} \cdot \mathrm{kg}^{-1} \cdot \mathrm{K}^{-1}$
d	diameter, $[d] = \mathrm{m}$
g	gravimetrical acceleration, $[g] = \mathrm{m} \cdot \mathrm{s}^{-2}$
h	surface coefficient of heat transfer, $[h] = \mathrm{W} \cdot \mathrm{m}^{-2} \cdot \mathrm{K}^{-1}$
K	coefficient of heat transfer, $[K] = \mathrm{W} \cdot \mathrm{m}^{-2} \cdot \mathrm{K}^{-1}$
k	thermal conductivity, $[k] = \mathrm{W} \cdot \mathrm{m}^{-1} \cdot \mathrm{K}^{-1}$
L	specific latent heat, $[L] = \mathrm{J} \cdot \mathrm{kg}^{-1}$
n	rotational speed, $[n] = \mathrm{s}^{-1}$
$\dot{q}$	surface–specific heat flux, $[\dot{q}] = \mathrm{W} \cdot \mathrm{m}^{-2}$
s	thickness, $[s] = \mathrm{m}$
T	thermodynamic temperature, $[T] = \mathrm{K}$
t	time, $[t] = \mathrm{s}$
u	velocity, $[u] = \mathrm{m} \cdot \mathrm{s}^{-1}$
x	(specific) length, $[x] = \mathrm{m}$

Greek

η	dynamic viscosity, $[\eta] = \mathrm{Pa} \cdot \mathrm{s}$
Θ	(immerging) angle, $[\Theta] = {}^\circ$ deg
k	thermal conductivity, $[k] = \mathrm{W} \cdot \mathrm{m}^{-1} \cdot \mathrm{K}^{-1}$
ϱ	density, $[\varrho] = \mathrm{kg} \cdot \mathrm{m}^{-3}$
σ	surface tension, $[\sigma] = \mathrm{N} \cdot \mathrm{m}^{-1}$

Mathematical Symbols

∂	partial differential
Δ	finite difference
d	differential

Dimensionless Numbers

Nu	Nusselt number, $\mathrm{Nu} = h \cdot x \cdot k^{-1}$
Re	Reynolds number, $\mathrm{Re} = \varrho \cdot v \cdot x \cdot \eta^{-1}$
Pr	Prandtl number, $\mathrm{Pr} = \eta \cdot c_p \cdot k^{-1}$
Bi	Biot number, $\mathrm{Bi} = h \cdot x \cdot k^{-1}$

Sub-/Superscripts

0	initial value
$\bar{\ }$	median
adh	adhesion
amb	ambient
HTF	Heat Transfer Fluid
h	hydraulic
i	iteration indices/inside
k	time step
l	liquid
m	melting
min	minimum
n	node/boundary
o	outer/outside
PCM	Phase Change Material
s	solid/boundary steel-PCM
x	local

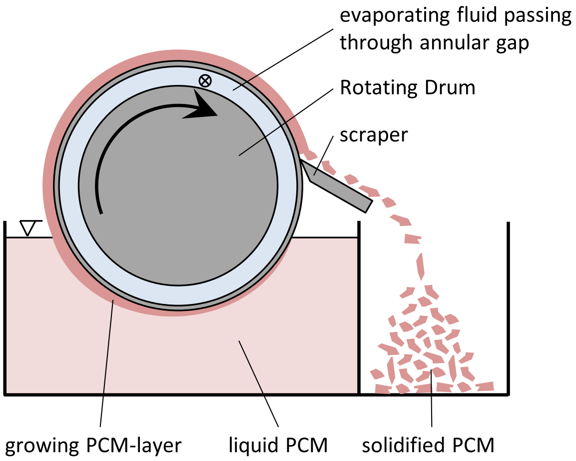

Fig. 1. Principle of the rotating drum heat exchanger.

Fig. 2. Figure of the experimental test rig examined in [1].

material as well as the storage tanks. Another essential characteristic of latent heat thermal energy storages is their isothermal temperature level during the phase change process. This enables an almost isothermal charging and discharging of thermal energy storages. This is a key element for the success of systems where the exergetic losses are crucial for the efficiency of the system, such as in a certain variant of Carnot batteries [4,5]. Furthermore, the provision of climate-neutral thermal energy for industrial processes, which is currently mainly based on fossil fuels, is becoming more in focus. Within the EU 28 states, the demand of thermal energy within the temperature range of 200 –400 °C amounts to 2200 PJ per year, which corresponds to about 5% of the final energy demand across all sectors [6]. Steam is the most important carrier of thermal energy within this temperature range [7]. With a heat storage system based on the rotating drum heat exchanger, this demand can be met on demand by fluctuating renewable energy sources, either directly in the form of heat or by electrical energy using a heat pump or resistance heating elements.

The rotating drum has been experimentally investigated using the low temperature PCM decanoic acid. The experimental results are presented in [1]. Currently, specific calculation approaches for determining the heat transfer of a rotating drum heat exchanger are quite limited within the literature. Within this research, two novel calculation approaches for the calculation of the effective heat transfer as well as the layer thickness of the solidified PCM are developed and verified by the experimental results. Both, one based on the quasistationary calculation approach and one detailed transient numerical simulation, based on the finite difference method, are compared with each other and investigated for their applicability on the rotating drum heat exchanger. The main objective of this research is to obtain a calculation tool for the discharge performance of a heat storage system based on the rotating drum. The calculation tool should be applicable for the optimization and dimensioning of a high-temperature rotating drum heat exchanger and the uncertainties in the calculation should be estimable.

2. Description of the modelling approaches

Within this section, two different calculation approaches for the rotating drum heat exchangers are introduced. Both calculation approaches contain models for the heat transfer coefficients at the outer and inner side of the rotating drum and for the thickness of the adhering liquid PCM when the surface is emerged from the liquid PCM, which are identified in the Sections 2.1–2.3. This is followed by the so called quasistationary calculation approach in Section 2.4 and the introduction of a detailed transient numerical simulation in Section 2.5.

2.1. *Heat transfer coefficients at the outer side of the rotating cylinder*

vThe heat transfer coefficient at the outer surface of the rotating drum is calculated by empirical correlations. For the heat transfer coefficient of a rotating cylinder completely surrounded by one medium, there are several correlations available in the literature e.g. in [8–11]. For a partially immerged rotating drum, no specific correlation could be identified by the authors. Nevertheless, the local surface–-specific heat transfer coefficient can be compared to a continuously moving flat surface within a quiescent medium. According to [12] the following expression can be used for laminar conditions

$$\frac{\mathrm{Nu_x}}{\sqrt{\mathrm{Re_x}\cdot\mathrm{Pr}}} = f(\mathrm{Pr}) \tag{1}$$

Further research on a continuously moving plane surface is also carried out by [13] and [14] with the same results for the laminar conditions. Here, $f(\mathrm{Pr})$ is found by a numerical solution and is 0.4174 at $\mathrm{Pr} = 0.7$ for the ambient air. For decanoic acid, used in [1] for the experimental study, the Prandtl-Number is 88.72. The value of $f(\mathrm{Pr} = 88.72)$ is found to be 0.5531 by linear interpolation of the data given in [13] between $\mathrm{Pr} = 30$ and $\mathrm{Pr} = 100$. In the same way, $f(\mathrm{Pr} = 6.4704)$ is determined to be 0.521 for sodium nitrate, later used in Section 4. The local Reynolds-Number $\mathrm{Re_x}$ and the local Nusselt-Number $\mathrm{Nu_x}$ are determined with the length x, which is the arc length from the point of immersion or emersion to the certain position, by

$$Re_x = \frac{\varrho\cdot u\cdot x}{\eta} \tag{2}$$

and

$$\mathrm{Nu_x} = \frac{h_x\cdot x}{k}. \tag{3}$$

The local surface–specific heat transfer coefficient h_x can be calculated by rearranging Equation (3). Expression (1) is also valid for a rotating cylinder, which is used in [12] for experimental validation. The critical Reynolds–Number in the given case is $5\cdot10^5$, which is not exceeded within the experimental data for the validation.

2.2. *Surface–specific heat transfer coefficient at the annular gap within the cylinder*

At the inner side of the rotating drum, a HTF passes through an annular gap, as illustrated in Fig. 1 and Fig. 3. The surface–specific heat transfer coefficient at the inner side of the outer cylinder is therefore calculated by an empirical correlation by Gnielinski given in [15]. The Reynolds-Number in this case is defined with the hydraulic diameter

$$d_h = d_o - d_i \tag{4}$$

with the inner diameter of the outer tube $\mathrm{d_o}$ and the outer diameter of the inner tube $\mathrm{d_i}$. The surface–specific heat transfer coefficient for water as HTF and the geometrical properties of the rotating drum as given in [1] can be determinate to be 4175 $\mathrm{W\cdot m^{-2}\cdot K^{-1}}$. In case of an evaporating medium, the determination of a surface–specific heat transfer coefficient is highly complex and depends on several parameters. Therefore, a generalized value of 15 000 $\mathrm{W\cdot m^{-2}\cdot K^{-1}}$ is used in this study. Details for a detailed investigation of the surface–specific heat transfer coefficient for a boiling HTF can be found in [16]. For the specific properties of water, the data given in [17] are used.

2.3. *Adhering liquid at a surface released from a tub*

The liquid PCM layer which adheres at the surface of the solidified PCM when it is removed from the tub can be considered as a classical Landau-Levich Problem. For a plate vertically withdrawn from a liquid, the layer thickness $\mathrm{s_{adh}}$ of the remaining liquid PCM can be calculated according to Landau and Levich [18] by

$$s_{\mathrm{adh}} = 0,93\cdot\left(\frac{\eta\cdot u}{\sigma}\right)^{\frac{1}{6}}\cdot\left(\frac{\eta\cdot u}{\varrho_1\cdot g}\right)^{\frac{1}{2}}. \tag{5}$$

For a rotating drum partially immersed in liquid medium, Gelperin et al. [19] suggest

$$s_{\mathrm{adh,min}} = 0,94\cdot\left(\frac{\pi\cdot d\cdot n\cdot\eta}{\sigma}\right)^{\frac{1}{6}}\left(\frac{3\cdot n\cdot d\cdot\eta}{4\cdot\varrho_1\cdot g\cdot\left(1-\frac{\Theta_{\mathrm{dwell}}}{360}\right)}\right)^{\frac{1}{2}} \tag{6}$$

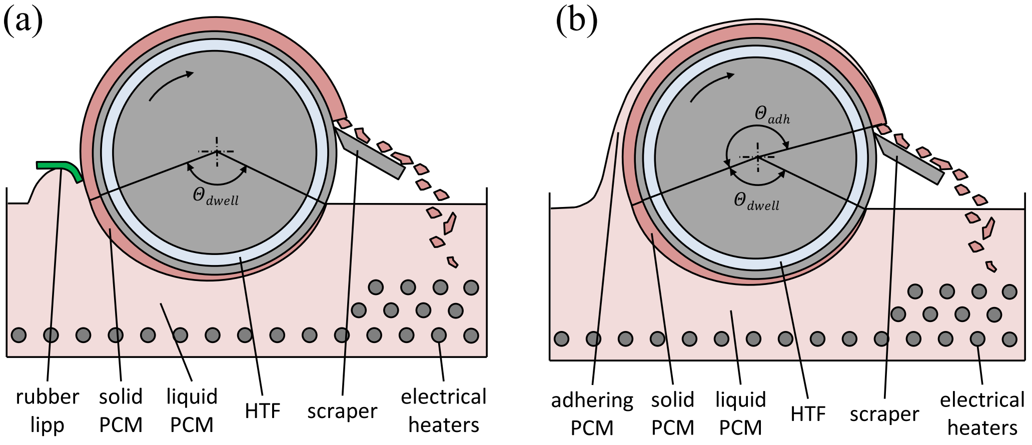

Fig. 3. Illustration of the rotating drum heat exchanger (a) without adhesion (b) with adhesion.

for the calculation of the minimum liquid layer at the uppermost part of the drum, where Θ_{dwell} is the immersion angle as shown in Fig. 3. This is validated numerically by Hasan and Naser [20]. Both equations assume backflow of liquid PCM. Thus, the solidification has to be slow compared to the backflow.

2.4. Quasistationary calculation

A first estimation of the heat transfer potential of the rotating drum can be done by the so-called quasistationary approximation, which is described in [21] and [22], among other. Thereby, the thermal capacities of the steel wall and the solidified PCM layer are neglected. Furthermore, the heat transfer from the outer surface of the rotating cylinder towards the ambient air is neglected. The surface-specific heat flux at any point of the submerged drum that has to be transferred from the point of solidification at the boundary of solid and liquid PCM through the solidified PCM and the metal heat exchanger wall to the HTF, can be determined by

$$\dot{q}_1(t) = \frac{1}{\frac{s_{\text{PCM,s}}(t)}{k_{\text{PCM,s}}} + \frac{1}{K}} \cdot \left(T_{\text{PCM,m}} - T_{\text{HTF}}\right) \tag{7}$$

with

$$\frac{1}{K} = \frac{s_{\text{wall}}}{k_{\text{wall}}} + \frac{1}{h_{\text{HTF}}}. \tag{8}$$

The surface–specific heat flux released by the phase change during solidification of the liquid PCM can be calculated by

$$\dot{q}_2(t) = L_{PCM} \cdot \varrho_{\text{PCM,s}} \cdot \frac{ds}{dt} \tag{9}$$

and the surface–specific heat flux resulting from the forced convection due to the overheating of the PCM and the moving surface is given by

$$\dot{q}_3(t) = h_{\text{x,PCM}} \cdot \left(T_{\text{PCM,l}} - T_{\text{PCM,m}}\right) \tag{10}$$

The thermal equilibrium at the solidification boundary shown in Fig. 4 is

$$\dot{q}_1(t) - \dot{q}_2(t) - \dot{q}_3(t) = 0. \tag{11}$$

By rearranging Equation (11) the thermal equilibrium at the solidification boundary results in

$$\frac{ds}{dt} = \frac{k_{\text{PCM,s}} \cdot \left(T_{\text{PCM,m}} - T_{\text{HTF}}\right)}{L_{\text{PCM}} \cdot \varrho_{\text{PCM,s}} \cdot \left(\mathrm{s(t)} + \frac{k_{\text{PCM,s}}}{K}\right)} - \frac{h_{\text{x,PCM}} \cdot \left(T_{\text{PCM,l}} - T_{\text{PCM,m}}\right)}{L_{\text{PCM}} \cdot \varrho_{\text{PCM,s}}}. \tag{12}$$

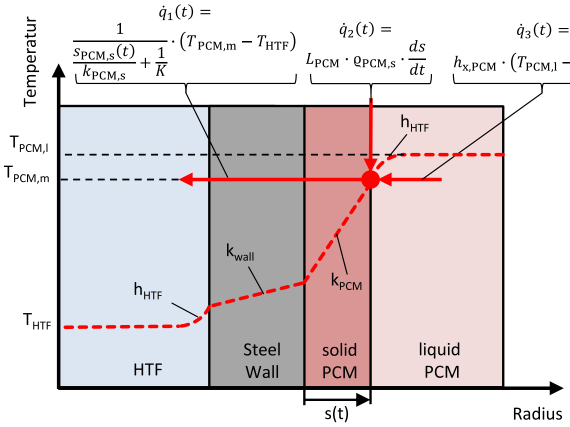

Fig. 4. Temperature profile and thermal equilibrium at the solidification point for the quasistationary calculation.

The actual total surface–specific heat flux from the point of solidification towards the HTF is

$$\dot{q}_{\text{dwell}}(t) = \dot{q}_1(t) = \dot{q}_2(t) + \dot{q}_3(t) \tag{13}$$

which results in

$$\dot{q}_{\text{dwell}}(t) = L_{\text{PCM}} \cdot \varrho_{\text{PCM,s}} \cdot \frac{ds}{dt} + h_{\text{x,PCM}} \cdot \left(T_{\text{PCM,l}} - T_{\text{PCM,m}}\right)$$

$$= \frac{1}{\frac{s(t)}{k_{\text{PCM,s}}} + \frac{1}{\mathrm{K}}} \cdot \left(T_{\text{PCM,m}} - T_{\text{HTF}}\right) \tag{14}$$

It is not possible to integrate Equation (12) analytically exactly, but it can be integrated numerically to obtain the time-dependent solidified PCM layer thickness s_{dwell}(t). In this way, the location-specific HTC $\mathrm{h_{x,PCM}}$ can be implemented as well. The mean surface-specific heat flux of the submerged surface of the drum during the dwell time t_{dwell} can be calculated according to the mean theorem

$$\bar{\dot{q}}_{\text{dwell}}\left(t_{\text{dwell}}\right) = \frac{1}{t_{\text{dwell}}} \int_0^{t_{\text{dwell}}} \dot{q}_{\text{dwell}}(t) \cdot dt \tag{15}$$

by equitation

$$\bar{\dot{q}}_{\text{dwell}}\left(t_{\text{dwell}}\right) = \frac{1}{t_{\text{dwell}}} \sum\nolimits_0^{t_{\text{dwell}}} \dot{q}_{\text{dwell}}(t) \cdot \mathrm{dt}. \tag{16}$$

The dwell time t_{dwell} of a rotating surface element is calculated from the rotational speed n and the submerged angle Θ_{dwell} as shown in Fig. 3 by

$$t_{\text{dwell}} = \frac{\Theta_{\text{dwell}}}{360^\circ} \cdot \frac{1}{n}. \tag{17}$$

The influence of the adhering liquid PCM layer, which solidifies after the surface emerges from the liquid PCM, on the heat transfer can also be estimated by the quasistationary calculation. For this purpose, the thickness of the liquid PCM layer is estimated according to Equation (6) and its temperature is assumed to be the melting temperature of the PCM. Since there is no convective heat transfer anymore, Equation (13) is reduced to

$$\frac{ds}{dt} = \frac{k_{\text{PCM,s}} \cdot \left(T_{\text{PCM,m}} - T_{\text{HTF}}\right)}{L_{\text{PCM}} \cdot \varrho_{\text{PCM,s}} \cdot \left(\mathrm{s(t)} + \frac{k_{\text{PCM,s}}}{K}\right)} \tag{18}$$

and the surface–specific heat flux can be calculated by

$$\dot{q}_{\text{adh}}(t) = L_{\text{PCM}} \cdot \varrho_{\text{PCM,s}} \cdot \frac{ds}{dt}. \tag{19}$$

The calculation is terminated when the adhesion layer calculated according to Equation (6) has completely solidified. This is given in case

$$s_{\text{adh}}(t) = s_{\text{adh,min}}. \tag{20}$$

In the case that the adhering liquid layer is not completely solidified before it is scraped off, the solidification time is calculated by

$$t_{\text{adh}} = \frac{\Theta_{\text{adh}}}{360^\circ} \cdot \frac{1}{n} \tag{21}$$

The average surface–specific heat flux density during the solidification of the adhering liquid is calculated according to Equation (15) by

$$\bar{\dot{q}}_{\text{adh}}\left(t_{\text{adh}}\right) = \frac{1}{t_{\text{adh}}} \sum\nolimits_0^{t_{\text{adh}}} \dot{q}_{\text{adh}}(t) \cdot \mathrm{dt} \tag{22}$$

The average heat transfer for the whole rotating drum is calculated by

$$\bar{\dot{q}}_{\text{total}} = \bar{\dot{q}}_{\text{dwell}}\left(t_{\text{dwell}}\right) \cdot \frac{t_{\text{dwell}}}{t_{\text{total}}} + \bar{\dot{q}}_{\text{adh}}\left(t_{\text{adh}}\right) \cdot \frac{t_{\text{adh}}}{t_{\text{total}}}. \tag{23}$$

Convective heat transfer from the ambient air to the outer surface of the rotating drum is neglected within the quasistationary calculation. No solidification occurs when the HTF temperature is above the melting point of the PCM. In this case, the surface-specific heat flux is calculated by

$$\dot{q}(t) = \frac{1}{\frac{1}{h_{\mathrm{HTF}}} + \frac{s_{\mathrm{wall}}}{k_{\mathrm{wall}}} + \frac{1}{h_{\mathrm{x,PCM}}}} \cdot \left(T_{\mathrm{PCM,l}} - T_{\mathrm{HTF}}\right) \tag{24}$$

2.5. Detailed transient numerical investigation

For a detailed simulation of the heat transfer of the rotating drum, a transient, 1-dimensional numerical scheme has been developed. For this purpose, the heat transfer is investigated by a 1–dimensional section, which is virtually rotated with the rotating drum by time-varying boundary conditions.

For the numerical calculation of a solidification problem, several solutions have been developed in the past. A good overview of several methods can be found in the work of Alexiades and Solomon [23]. For a highly detailed numerical investigation of solidification and melting processes including convection within the liquid phase, the enthalpy-porosity method for the energy equations and a discretization according to the finite-volume method is well known and widely used, e.g. in [24–28]. This method provides excellent results in acceptable simulation time for closed spaces with defined boundary conditions. In addition, a so-called mushy-zone, a region with a certain temperature range where the phase change occurs, can be implemented. Also, the Finite-Element-Method of Galerkin with a varied mesh provides accurate simulation results for solidification and melting behavior of latent heat thermal energy storages as shown e.g. in [29,30]. Compared to the Finite-Volume-Method, this method has advantages in complex structures due to the adoptable mesh.

The main aim of the numerical scheme developed in this work is to have flexible boundary conditions that can be easily changed several times during the rotation of the drum. Therefore, a Finite–Difference–Method with a varied time step has been chosen, which has been adopted from Baehr and Stephan [22]. Since the time step is varied with each iteration, the choice of the Implicit Euler Scheme for its discretization guarantees stability. The choose of a transient 1-dimensional scheme is sufficient for the simulation of the rotating drum and keeps the simulation simple and the computational times low. Natural convection is not considered in the simulation since forced convection dominates the heat transfer at the rotating drum. A mathematical verification of the numerical simulation is given in Section 2.7.

2.5.1. Governing equations

The temperature profile from the HTF inside the drum to the liquid PCM or ambient air outside the drum is shown in Fig. 5. In Table 1, the governing equations for the different sections are shown. The heat transfer from the HTF inside the drum to the steel wall of the heat exchanger at **(1)** is reproduced with a convective boundary condition by Equation (25), followed by the partial differential Equation (26) for heat conduction within the steel wall **(2)**. At the boundary between the steel wall and the solidified PCM **(3)**, the specific heat transfer within the solid PCM and the steel must be constant, reproduced by Equation (27). The heat transfer within the solid PCM **(4)** is also reproduced by the partial differential Equation (28) for heat conduction. At the point of solidification **(5)**, two different cases are considered. In the case of solidification while the surface is immerged in liquid PCM **(5a)**, the local equilibrium is reproduced by Equation (29) analogous to the quasistationary calculation. When adhering liquid PCM is considered while the surface is rotating in ambient air, the equilibrium at the solidification point **(5b)** is reproduced by Equation (30), which is composed of the heat transferred by conduction within the solidified and liquid adhering PCM and the heat of solidification. The temperature within the adhering liquid PCM **(6)** is therefore given by Equation (31), another partial differential equation for heat conduction. The heat transfer to the ambient air **(7)** is given by a convective boundary condition by Equation (32), similar to the heat transfer at the HTF inside the drum.

2.5.2. Discretization of the equations

The equations shown in Table 1 are discretized by an implicit finite difference method. A varying time step is introduced for consideration of the time-varying solidification rate.

The location-dependent change of temperature is approximated by the symmetric difference quotient of first

$$\frac{\partial T}{\partial x} = \frac{T_{i+1}^{k} - T_{i-1}^{k}}{2\Delta x_i} \tag{33}$$

and second order

$$\frac{\partial^2 T}{\partial x^2} = \frac{T_{i-1}^{k} - 2T_i^{k} + T_{i-1}^{k}}{\Delta x_i^2}. \tag{34}$$

The time-dependent change of temperature is approximated by the backward difference quotient

$$\frac{\partial T}{\partial t} = \frac{T_i^{k} - T_i^{k-1}}{\Delta t}. \tag{35}$$

Thus, the heat conduction within the steel wall (2), the solid PCM (4) and the adhering liquid (6) can be calculated by

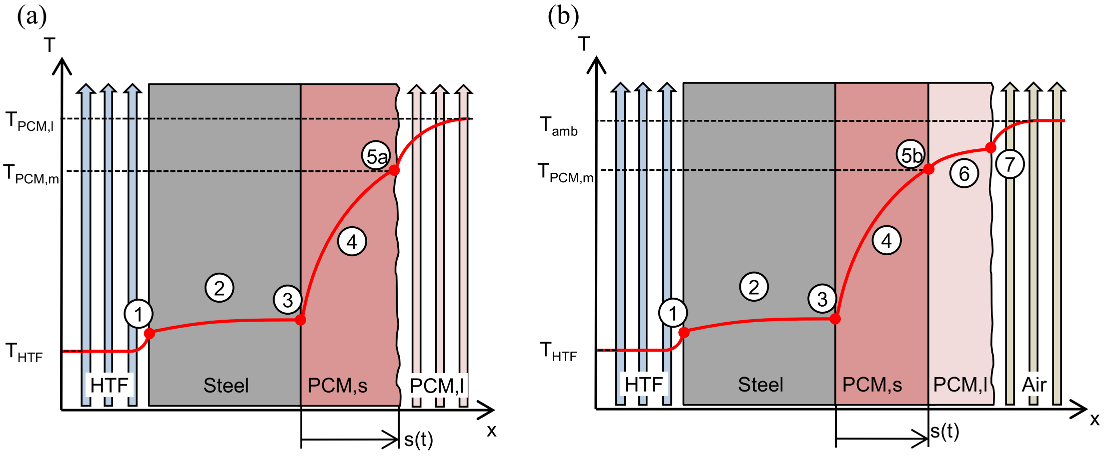

Fig. 5. Temperature profile of the heat transfer (a) during the submersion of the drum surface in liquid PCM (b) during the solidification of adhering liquid PCM while the drum surface is rotating in ambient air.

Table 1
Governing equations for the numerical transient simulation.

Location			Equation	
Convective Heat Transfer of HTF	①	$x = 0$	$-k_{\text{steel}} \cdot \left(\frac{\partial T}{\partial x}\right)_{x=0} = h_{\text{HTF}} \cdot (T_{\text{wall}} - \vartheta T_{\text{HTF}})$	(25)
Heat conduction steel	②	$0 < x < s_{\text{steel}}$	$\frac{\partial T}{\partial t} = a_{\text{steel}} \cdot \frac{\partial^2 T}{\partial x^2}$	(26)
Transfer Steel-PCM$_{\text{solid}}$	③	$x = s_{\text{steel}}$	$c_p, \text{steel} \cdot \varrho_{\text{steel}} \cdot \frac{\partial \text{T}}{\partial \text{t}} = \frac{T}{\partial x}\left(k_i \cdot \frac{\partial \text{T}}{\partial \text{x}}\right)$	(27)
Heat conduction PCM$_{\text{solid}}$	④	$s_{\text{steel}} < x < s(t)$	$\frac{\partial T}{\partial t} = a_{\text{PCM,s}} \cdot \frac{\partial^2 T}{\partial x^2}$	(28)
Point of Solidification	(5a)	$x = s(t)$	$L_{\text{PCM}} \cdot \varrho_{\text{PCM,s}} \cdot \frac{\text{ds}}{\text{dt}} + h_{\text{x,PCM}}\left(T_{\text{PCM,l}} - T_{\text{PCM,m}}\right) = k_{\text{PCM,s}} \cdot \frac{\partial \text{T}}{\partial \text{x}}$	(29)
	(5b)	$x = s(t)$	$\text{L}_{\text{PCM}} \cdot \varrho_{\text{PCM,s}} \cdot \frac{\text{ds}}{\text{dt}} + k_{\text{PCM,l}} \cdot \frac{\partial \text{T}}{\partial \text{x}} = k_{\text{PCM,s}} \cdot \frac{\partial \text{T}}{\partial \text{x}}$	(30)
Heat conduction in adhering liquid	⑥	$s(t) < x < h_{0,\min}$	$\frac{\partial T}{\partial t} = a_{\text{PCM,l}} \cdot \frac{\partial^2 T}{\partial x^2}$	(31)
Convective Heat Transfer of ambient air	⑦	$x = h_{0,\min}$	$-k_{\text{PCM,l}} \cdot \left(\frac{\partial T}{\partial x}\right)_{x=M} = h_{\text{x,amb}} \cdot \left(T_{\text{PCM,l}} - T_{\text{amb}}\right)$	(32)

$$a_i \frac{T^k_{i-1} - 2T^k_i + T^k_{i+1}}{\Delta x_i^2} = \frac{T^k_i - T^{k-1}_i}{\Delta t}. \tag{36}$$

By introducing

$$r_i = a_i \frac{\Delta t}{\Delta x_i^2} \tag{37}$$

one gets

$$T_i^{k-1} = -r_i \cdot T^k_{i-1} + (1 + 2r_i) \cdot T^k_i - r_i \cdot T^k_{i+1}. \tag{38}$$

Since the geometric thickness of the steel wall is large in compared to the geometric thickness of the solid and adhering PCM layer, the location-depended step Δx_1 within the steel wall can be larger compared to the step-size within the solid and liquid PCM layer Δx_2 to reduce computation time and increase accuracy. Therefore, in the last node of the steel wall $i = s$, Equation (27) is applied and discretized by

$$c_{\text{p,Steel}} \cdot \varrho_{\text{steel}} \cdot \frac{T^k_i - T^{k-1}_i}{\Delta t} = k_{\text{PCM,s}} \cdot \frac{T^k_{i+1} - T^k_i}{\Delta x_2} - k_{\text{Steel}} \cdot \frac{T^k_i - T^k_{i-1}}{\Delta x_1} \tag{39}$$

what results in

$$T_s^{k-1} = -R \cdot \frac{k_{i+1}}{\Delta x_1 \cdot \Delta x_2} \cdot T^k_{i+1} + \left(R\left(\frac{k_{i+1}}{\Delta x_1 \cdot \Delta x_2} + \frac{k_i}{\Delta x_1^2}\right) + 1\right) T^k_i - R \cdot \frac{k_i}{\Delta x_1^2} \cdot T^k_{i-1} \tag{40}$$

with

$$R = \frac{\Delta t}{\varrho_{\text{Steel}} \cdot c_{\text{p,Steel}}}. \tag{41}$$

Defining the node $i = 1$ as the first node of the steel wall, the convective boundary condition (1) can be discretized by

$$T^k_0 = T^k_2 - \frac{2 \cdot h_{\text{HTF}} \cdot \Delta x_1}{k_{\text{steel}}} (T_1 - T_{\text{HTF}}) \tag{42}$$

When combining (38) and (42), one gets for the first node at $i = 1$

$$T_1^{k-1} + 2 \cdot r_i \cdot Bi_1 \cdot T_{\text{HTF}} = (1 + 2 \cdot r_i \cdot (1 + Bi_1)) \cdot T^k_1 - 2 \cdot r_i \cdot T^k_2 \tag{43}$$

with

$$Bi_1 = \frac{h_{\text{HTF}} \cdot \Delta x_1}{k_{\text{steel}}} \tag{44}$$

In case of adhering PCM one gets for the last node $i = M$ of the adhering liquid PCM layer accordingly

$$T_M^{k-1} + 2 \cdot r_i \cdot Bi_2 \cdot T^k_{\text{amb}} = (1 + 2r_i \cdot (1 + Bi_2)) \cdot T^k_1 - 2 \cdot r_i \cdot T^k_2 \tag{45}$$

with

$$Bi_2 = \frac{h_{\text{x,amb}} \cdot \Delta x_2}{k_{\text{PCM,s}}}. \tag{46}$$

The point of solidification at node $i = n$ is assumed to be an isothermal wall with the temperature of the melting point of the PCM. Therefore, Equation (38) for the node $i = \text{n-1}$ is adapted to

$$T^{k-1}_{n-1} + r_i T^k_n = -r_i \cdot T^k_{n-2} + (1 + 2r_i) \cdot T^k_{n-1} \tag{47}$$

and in case of adhering liquid PCM the node $i = n + 1$ is adapted accordingly to

$$T^{k-1}_{n+1} + r_i T^k_n = -r_i \cdot T^k_{n+2} + (1 + 2r_i) \cdot T^k_{n+1} \tag{48}$$

with

$$T^k_n = T^{k-1}_n = T_m. \tag{49}$$

To reproduce the solidification, the isothermal boundary condition at $i = n$ is moving within the mesh with every iteration step. The time of an iteration step Δt is calculated from Equation (29) in case of solidification within the liquid PCM by

$$\Delta t = \frac{h_{\text{PCM}} \cdot \varrho \cdot \Delta \text{x}}{k_{\text{PCM,s}} \cdot \frac{T^{k-1}_n - T^{k-1}_{n-1}}{\Delta x_2} - h_{\text{x,PCM}} \cdot \left(T_{\text{PCM,l}} - T_{\text{PCM,m}}\right)} \tag{50}$$

and in case of adhering liquid PCM by

$$\Delta t = \frac{h_{\text{PCM}} \cdot \varrho \cdot \Delta \text{x}}{k_{\text{PCM,s}} \cdot \frac{T^{k-1}_n - T^{k-1}_{n-1}}{\Delta x_2} - k_{\text{PCM,l}} \cdot \frac{T^{k-1}_{n+1} - T^{k-1}_n}{\Delta x_2}}. \tag{51}$$

Equations (38), (40), (43), (45), (47) and (48) results in a system of linear dependent equations. They can be summarized by

$$\overset{\text{ì¿}}{\boldsymbol{M}}^{\mathbf{k}} \cdot \overrightarrow{\boldsymbol{T}}^{\boldsymbol{k}} = \overrightarrow{\boldsymbol{T}}^{\boldsymbol{k}-1} + \overrightarrow{\boldsymbol{b}}$$

with the vectors of the temperature in the previous $\overrightarrow{\boldsymbol{T}}^{\boldsymbol{k}-1}$ and current $\overrightarrow{\boldsymbol{T}}^{\boldsymbol{k}}$ time step, the boundary conditions within vector $\overrightarrow{\boldsymbol{b}}$ and a sparse band matrix $\overset{\text{ì¿}}{\boldsymbol{M}}^{\mathbf{k}}$. The Matlab® routine mldivide is used for solving the linear system.

2.6. *Material properties*

For the validation of the introduced models the experimental data published in [1] are used. Therefore, the material properties of decanoic acid are required which are given in Table 2. An analysis of the sensitivity of the materials properties, discussed in Section 3.5, shows that the density of the solid phase, the phase change enthalpy, the thermal conductivity of the PCM and the viscosity of the liquid PCM have an important influence of

Table 2
Thermophysical properties of decanoic acid.

Description	Variable	Value	Unit	Remark	Source
Melting point	$T_{PCM,m}$	31.5	°C		[31]
Phase change enthalpy	L_{PCM}	164.1	$kJ\cdot kg^{-1}$		measured
Thermal conductivity, liquid	$k_{PCM,l}$	0.149	$W\cdot m^{-1}\cdot K^{-1}$	(at 40 °C)	[31]
Thermal conductivity, solid	$k_{PCM,s}$	0.1763	$W\cdot m^{-1}\cdot K^{-1}$	(at 17.5 °C)	measured
Density, liquid	$\varrho_{PCM,l}$	886.3	$kg\cdot m^{-3}$	(at 37.8 °C)	[32]
Density, solid	$\varrho_{PCM,s}$	916	$kg\cdot m^{-3}$	(at 21 °C)	measured
Viscosity	$\eta_{PCM,l}$	0.0073	Pa·s	(at 34 °C)	measured
Heat capacity, liquid	$c_{p,PCM,l}$	2.0883	$kJ\cdot kg^{-1}\cdot K^{-1}$	(at 35–65 °C)	[33]
Heat capacity, solid	$c_{p,PCM,s}$	2.0967	$kJ\cdot kg^{-1}\cdot K^{-1}$	(at 0–24 °C)	[33]
Surface tension	$\sigma_{PCM,l}$	0.0277	$N\cdot m^{-1}$	(at 31.9 °C)	[34]

both, the transferred heat as well as the thickness of the solidified PCM layer. Therefore, these properties are measured within this research. The phase change enthalpy is measured by differential scanning colometry, the thermal conductivity is measured by a parallel-plate thermal conductivity apparatus, the density is determined by measuring the displacement of water and the viscosity is measured by a rheometer. The results are given in Table 2 as well. For the calculation and discussion of a high temperature heat exchanger for latent heat storage using sodium nitrate as PCM, the material properties given in Table 3 are used. As the material properties closely to their melting temperature influences the calculation the most, the temperature dependence of the materials is neglected and values close to the melting point are selected.

2.7. Verification of the models

There is no analytically exact solution for the calculation of the given solidification problem. Therefore, the mathematical problem is reduced to certain boundary conditions for verification. The analytical solution of Stefan, first presented in [39] and described in detail in [22], can be used to verify the numerical scheme and the quasistationary calculation when reducing the problem to solidification of a liquid PCM at melting temperature on an isothermal wall with a temperature below the melting temperature. The Neumann-Solution described in [40] is used for the verification of the solidification process of the adherent liquid after the surface is removed from the PCM-tub. Again, convective heat transfer inside the drum and heat conduction inside the steel wall are neglected to assume an isothermal solidification wall. The time-dependent heat transferred at the isothermal wall and the thickness of the solidified PCM layer are given in Fig. 6. The assumed temperature difference between the isothermal wall and the melting temperature of the PCM is 10 K for decanoic acid and 100 K for sodium nitrate in the Stefan-Solution. For the Neumann-Solution, an additional temperature difference between the melting point and the liquid PCM of 10 K for decanoic acid and 100 K for sodium nitrate is assumed, resulting in a total temperature difference of 20 K and 200 K, respectively. The difference in solidified layer thickness and transferred heat between the numerical solutions and the exact solutions is less than 0.05%, which verifies the numerical simulation. The quasistationary solution overestimates both the layer thickness and the heat transfer, and the deviations of the calculated layer thickness and heat transfer are equal in percentage. The deviation is 2% for the calculation with decanoic acid and 11% for the calculation with sodium nitrate. In the case of complete heat transfer from the inner HTF to the liquid PCM with a temperature above the melting point of the PCM and a constant outer convective heat transfer coefficient, the thickness of the solidified PCM layer and the heat flux takes constant values when viewed for a long period of time. In this case, the steady-state solutions of the numerical simulation and the quasistationary calculations must be identical after a long period of time, which is the case for the presented numerical model. For an estimation of the error due to the use of axial coordinates instead of cylindrical coordinates, no analytically exact solutions could be identified by the authors. For radial coordinates, analytically exact solutions are identified only for point and line heat sources, which are not applicable to the current problem. When reducing the problem to a solidification process on an isothermal wall, the ratio between the radius of the inner isothermal wall and the radius of the outer solidification front is 0.989, assuming a layer thickness of 1 mm. Since this ratio is close to 1, corresponding to a flat wall, the influence of the axial coordinates can be neglected. The overall ratio between the inner radius passed by the HTF and the outer radius where solidification occurs is 0.935, assuming a layer thickness of the solidified PCM of 1 mm. Here, the error due to the use of axial coordinates instead of cylindrical coordinates can by estimated by comparing the presented quasistationary solution with the quasistationary solution using cylindrical coordinates, also presented in [22]. The deviation of both, the solidified layer thickness as well as the heat flux is below 1% at rotational speeds below 4 min^{-1} and is rising up to 4% at 35 min^{-1}.

Table 3
Thermophysical properties of sodium nitrate.

Description	Variable	Value	Unit	Remark	Source
Melting point	$T_{PCM,m}$	306	°C		[3]
Phase change enthalpy	L_{PCM}	178	$kJ\cdot kg^{-1}$		[3]
Thermal conductivity, liquid	$k_{PCM,l}$	0.514	$W\cdot m^{-1}\cdot K^{-1}$	at 317 °C	[35]
Thermal conductivity, solid	$k_{PCM,s}$	0.73	$W\cdot m^{-1}\cdot K^{-1}$	at 246 °C	[3]
Density, liquid	$\varrho_{PCM,l}$	1908	$kg\cdot m^{-3}$	at 306 °C	[36]
Density, solid	$\varrho_{PCM,s}$	2113	$kg\cdot m^{-3}$	at 306 °C	[36]
Viscosity	$\eta_{PCM,l}$	0.002854	Pa·s	at 317 °C	[37]
Heat capacity, liquid	$c_{p,PCM,l}$	1.655	$kJ\cdot kg^{-1}\cdot K^{-1}$	at 306 °C	[3]
Heat capacity, solid	$c_{p,PCM,s}$	1.384	$kJ\cdot kg^{-1}\cdot K^{-1}$	at 150 °C	[3]
Surface tension	$\sigma_{PCM,l}$	0.1196	$N\cdot m^{-1}$	at 316 °C	[38]

3. Comparison of the models with experimental data

In this section, the data calculated with the introduced models are compared with the experimental data from [1] and later discussed in Section 3.5. Both temperature differences, the difference between the temperature of the HTF inside the rotating drum and the melting point of the PCM ($T_{m,PCM}$-T_{HTF}) and the temperature difference between the melting point of the PCM and the temperature of the liquid PCM ($T_{l,PCM}$-$T_{m,PCM}$) affect the heat transfer. These both temperature differences are also illustrated in Figs. 4 and 5(a). The temperature setting of the presented data are given together with the total temperature difference between the temperature of the HTF and the temperature of the liquid PCM as shown in Fig. 7.

3.1. Thickness of the adhering layer

The thickness of the adhesive layer given in [1] is calculated from the measured layer thicknesses with and without adhesion. At rotational speeds above 12 min^{-1}, the measured adhesive layer was not completely solidified when scraped off the drum and was therefore not measured in detail. Therefore, only values up to 12 min^{-1} are compared. The calculation according to Landau-Levich (Equation (5)) overestimates the adhesion layer thickness by 139% on average. If the measured values are compared with the values calculated according to Gelperin (Equation (6)), the average deviation is 39% (see Fig. 8).

3.2. Convective heat transfer without solidification

In case of a HTF temperature inside the rotating drum above the melting temperature of the PCM, no solidification occurs. Convection of

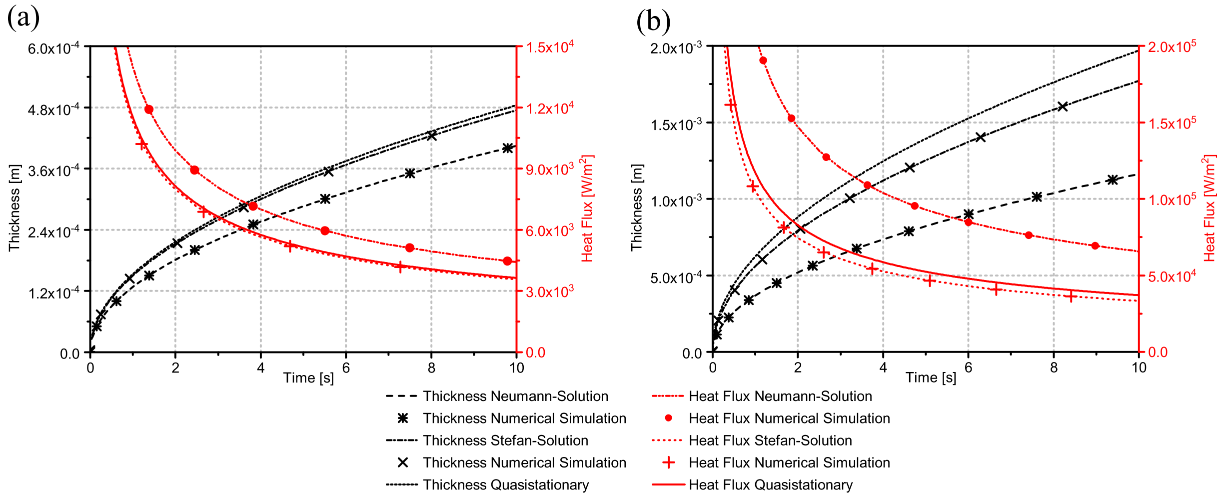

Fig. 6. Verification of the models (a) for decanoic acid with a temperature difference of 10 K between the HTF and the melting point and further 10 K between the melting point and liquid PCM (b) for sodium nitrate with a temperature difference of 100 K between the HTF and the melting point and further 100 K between the melting point and liquid PCM.

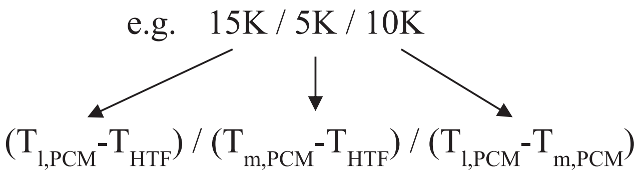

Fig. 7. Nomenclature of the temperature setting.

the liquid PCM on the rotating drum wall is dominates the heat transfer in this case. Fig. 9 compares the measured heat transfer without adhesion with the calculated heat transfers of the numerical simulation and the quasistationary calculation. While the quasistationary calculation underestimates the heat transfer by 37% on average, the numerical simulation reproduces the measured values above a rotational speed of 4 min^{-1} with an underestimation of 8% on average. At low rotational speeds below 4 min^{-1}, the experimental values exceed the numerically calculated values by 36% on average. When adhering liquid PCM is included, the increase in the heat transfer at increasing rotational speeds is more linear compared to the values without adhesion. This is also reproduced by the numerical simulation shown in Fig. 10. While the numerical simulation reproduces the measured value for rotational speeds above 4 min^{-1} with an average deviation of 11%, the measured values below 4 min^{-1} are underestimated by 31% on average. No quasistationary calculations are available for the case of convective heat transfer with adhesion, since the heat capacity of the adhering liquid PCM layer is neglected by the quasistationary calculation.

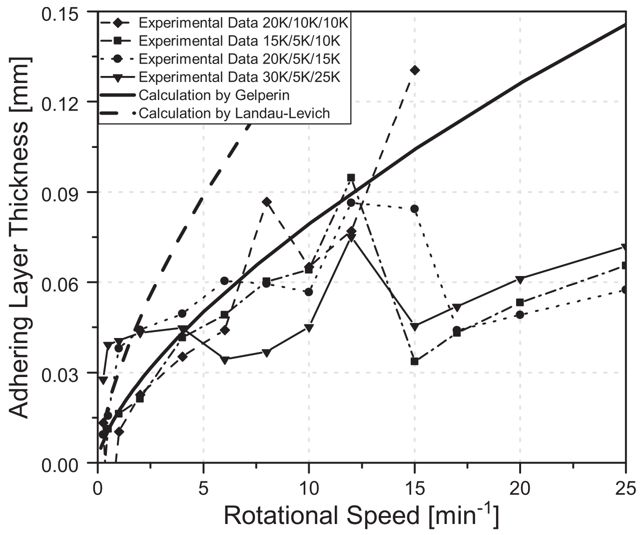

Fig. 8. Measured and calculated adhesion layer thicknesses.

3.3. Heat transfer with solidification

If the adhering liquid layer is removed by a rubber lip shortly after the surface emerges from the liquid PCM, the solidification of the PCM is limited to the immersed surface only. The convective heat transfer from the outer solidified PCM layer to the ambient air is only considered in the numerical simulation, but neglected in the quasistationary calculation. Fig. 11 compares the experimental data with the calculated values. The quasistationary calculation underestimates the experimental data by 30% on average. Focusing on the values with a temperature difference of 5 K between the temperature of the HTF inside the drum and the melting temperature of the PCM, it is noticeable that the increase in heat flux due to an increase in the temperature difference between the melting temperature of the PCM and the temperature of the liquid PCM is similar in absolute values. The numerical simulation reproduces the experimental data on average with a deviation of 17%. While the deviation for the temperature setting of 15 K/5K/10 K is below 15%, the numerical simulation underestimates the experimental values of the temperature setting of 20 K/10 K/10 K by 18% on average. Similar to purely convective heat transfer, the simulation reproduces the heat transfer at rotational speeds above 4 min^{-1} with a deviation of 11%, while the deviation is 22% on average at rotational speeds below 4 min^{-1}.

If the adhering layer of liquid PCM is not removed by a rubber lip, the adhering layer of liquid PCM solidify after the surface has left the liquid PCM. This increases the surface where solidification takes place and thus increases the effective heat flux. Fig. 12 shows the calculated and the experimental data. The data of the numerical simulation and the quasistationary calculation show an almost linear growth of the heat flux with increasing rotational speeds up to a significant point where the growth flattens out. At this point, the adhering layer is not yet fully solidified when it reaches the scraper. At a temperature difference of 5 K between the temperature of the HTF and the melting point of the PCM the point of flattening calculated by the numerical simulation is at a rotational speed of 11 min^{-1}, while the quasistationary calculation determinates the point of flattening at 14 min^{-1}. The point of flattening is

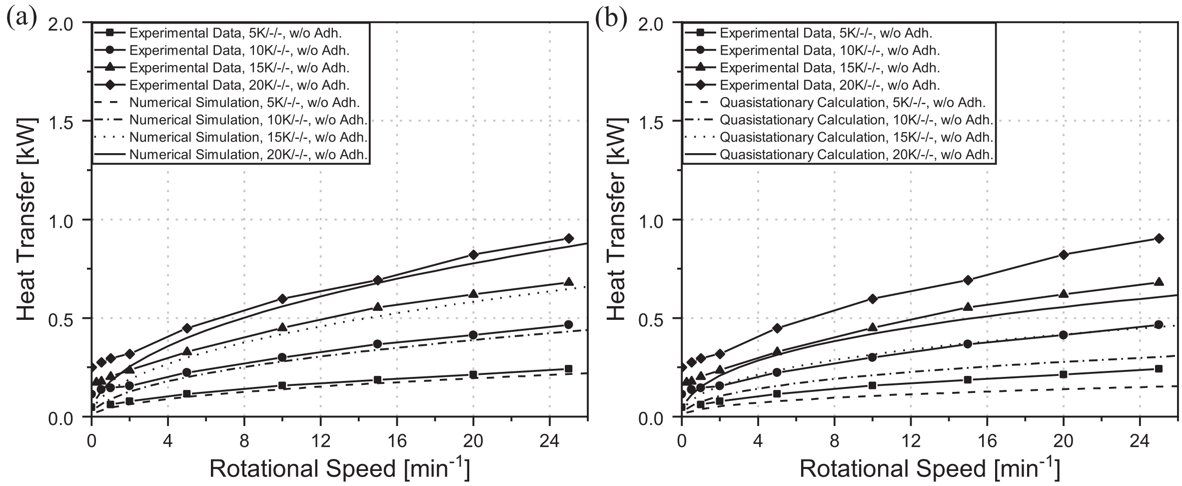

Fig. 9. Comparison of the measured convective heat transfer without solidification and without adhesion at the rotating drum (a) with the numerical simulation (b) with the quasistationary calculation.

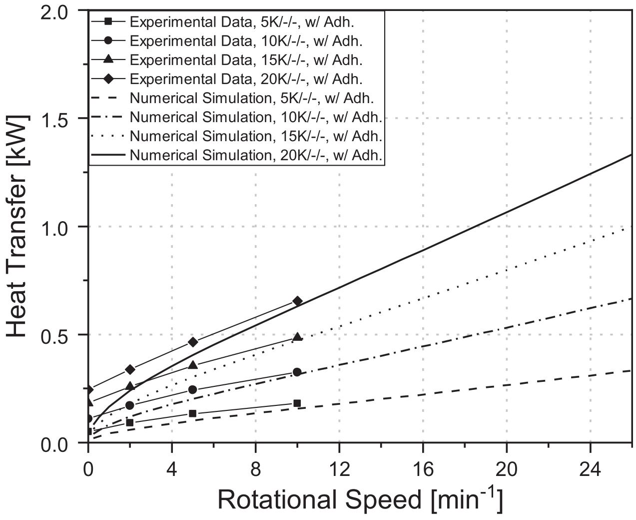

Fig. 10. Comparison of the measured convective heat transfer without solidification with adhesion at the rotating drum with the numerical simulation.

more significant in the data of the quasistationary calculation. For the temperature configuration 20 K/10 K/10 K, the point of flattening is above the range shown. The quasistationary calculation underestimates the experimental data by 37% on average. Contrary to the results of the heat flux without adhesion, the increase of the heat flux due to the increase of the temperature of the liquid PCM is not reproduced by the quasistationary calculation. The numerical simulation reproduces the experimental data with an accuracy of 14% on average. Again, the deviation is 6% on average at rotational speeds above 4 min^{-1} while the deviation is 20% for rotational speeds below 4 min^{-1}.

3.4. *Thicknesses of the solidified PCM layer*

The calculation methods presented can also be used to calculate the solidified layer thickness at the rotating drum. The results of the calculations are compared with the measured values in Fig. 13 for the case with adhesion and in Fig. 14 for the case without adhesion. The layer thickness is reproduced qualitatively correct by both calculation approaches. In the case of adhering liquid PCM, as already mentioned in Section 3.1, the layer was not completely solidified when reaching the scraper at high rotational speeds. This can be seen in the experimental data and is also reproduced by the models. At a temperature difference of 5 K between the HTF and the

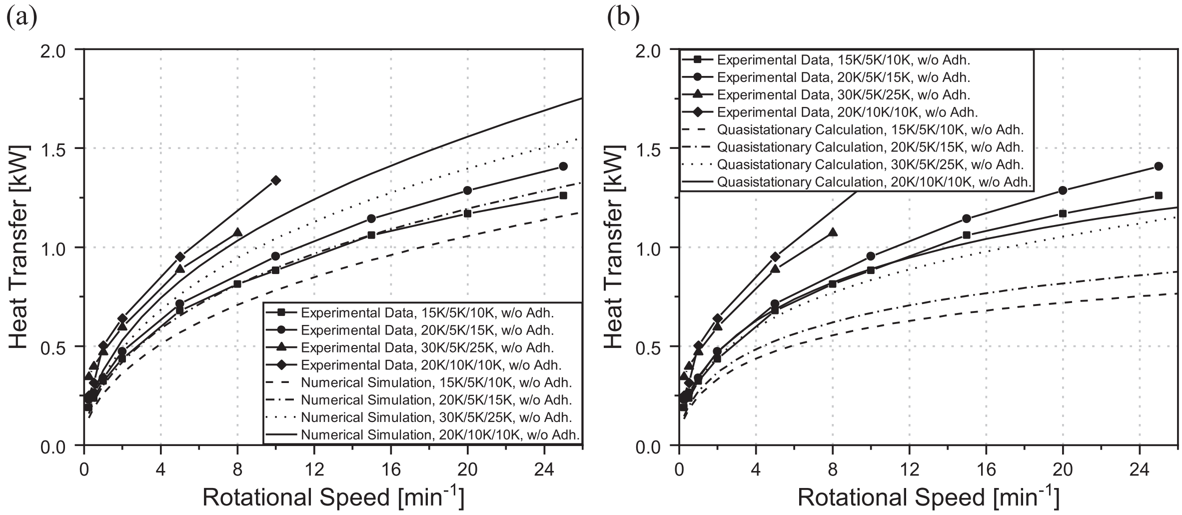

Fig. 11. Comparison of the measured heat transfer during solidification and without adhesion at the rotating drum (a) with the numerical simulation (b) with the quasistationary calculation.

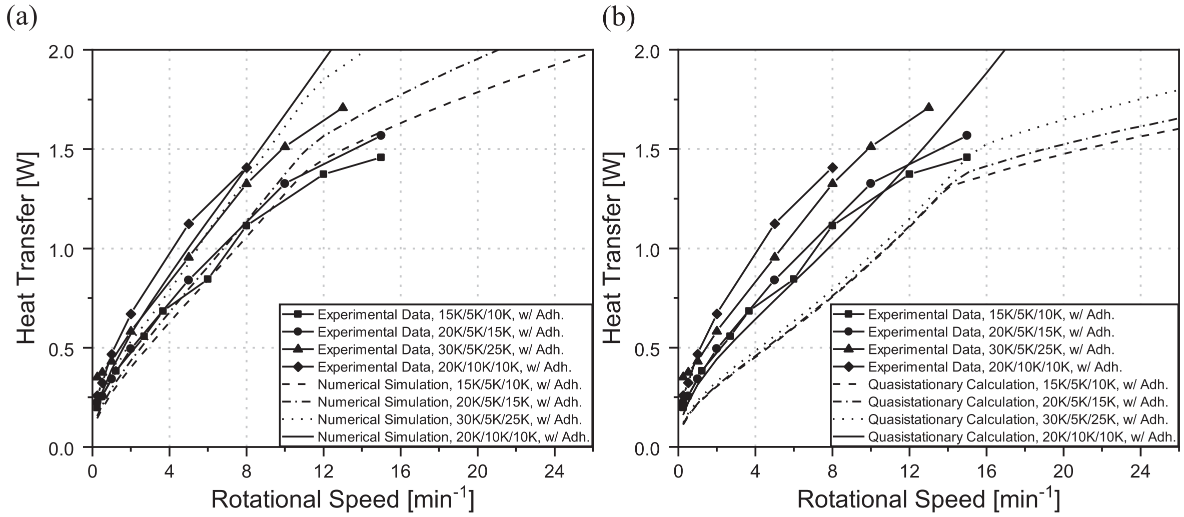

Fig. 12. Comparison of the measured heat transfer during solidification with adhesion at the rotating drum (a) with the numerical simulation (b) with the quasistationary calculation.

melting point of the PCM, the significant bend in the layer thickness is found in the experimental data at a rotational speed of 12 min^{-1}, which is reproduced by the transient numerical simulation correctly. The data calculated by the quasistationary approach shows this bend at a rotational speed of 16 min^{-1}. In case of a temperature difference of 10 K between the HTF and the melting temperature of the PCM, the experimentally measured layer thickness is reproduced by the transient numerical simulation with a deviation of 6% on average and is underestimated by the quasistationary calculation by 12% on average. The experimentally measured layer thickness at a temperature difference of 5 K between the HTF and the melting temperature of the PCM is underestimated by both calculation methods. While the transient numerical simulation underestimates the measured values by 110% on average, the quasistationary calculation underestimates the measured values by 71% on average. The deviation of the calculation from the experimental data is higher with an increased temperature difference between the melting temperature of the PCM and the temperature of the liquid PCM. Thus, the average deviation of the calculated data obtained by the numerical simulation is increased from 59% to 178% when the temperature difference between the melting temperature of the PCM and the temperature of the liquid PCM is increased from 10 K to 25 K, with a common temperature difference of 5 K between the HTF and the melting point of the PCM.

3.5. Discussion of the deviations and the influence of the material properties

When comparing the deviation of the heat flux calculated by the quasistationary calculation and the transient numerical simulation, the results of the quasistationary calculation are always and on average 22% lower instead of the data calculated by the numerical simulation. Since the quasistationary calculation shows a slightly increased heat flux of 2% on average in the verification (Section 0), this may be unexpected. To explanation this behaviour, the unsteady effects during the rotation of the one–dimensional solidification line have to be considered. So, the solidified layer grows when immersed in liquid PCM, while the temperature inside the solidified PCM layer and the steel wall is almost constant due to the isothermal solidification front. The same behaviour continues when adhering PCM solidifies but the temperature of the liquid adhering layer decreases. When the adhesion layer is completely solidified, the temperature inside the steel wall and the solidified PCM layer decreases since there is still a temperature difference to the temperature of the inner HTF. This is also continued within the steel wall after the solidified PCM layer is scraped off. At the point of immersion, the steel wall heats up, resulting in increased heat transfer and an increased growth rate of the PCM layer.

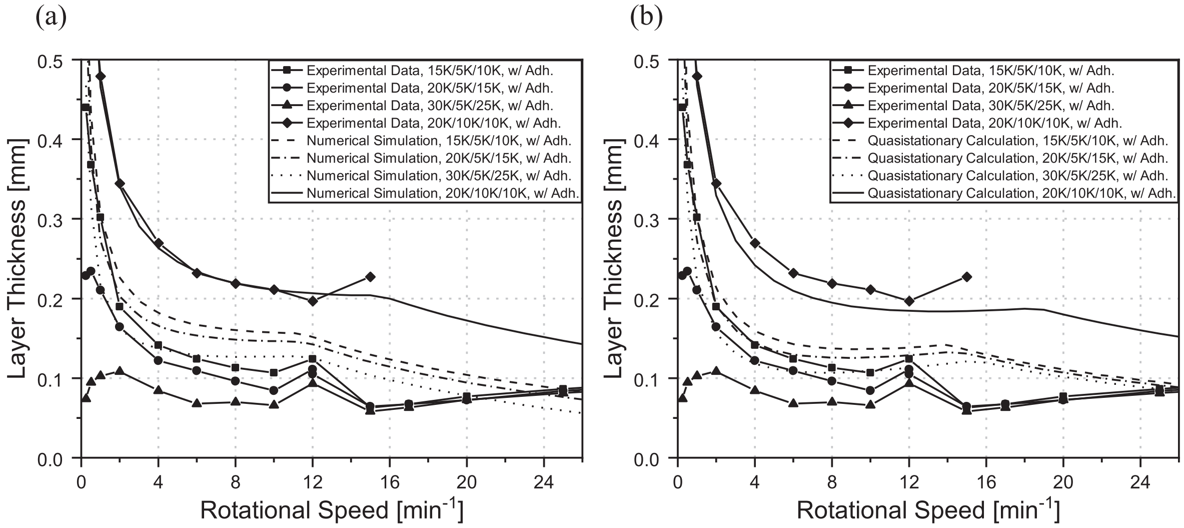

Fig. 13. Comparison of the measured layer thicknesses with adhesion at the rotating drum (a) with the numerical simulation (b) with the Quasi-Steady calculation.

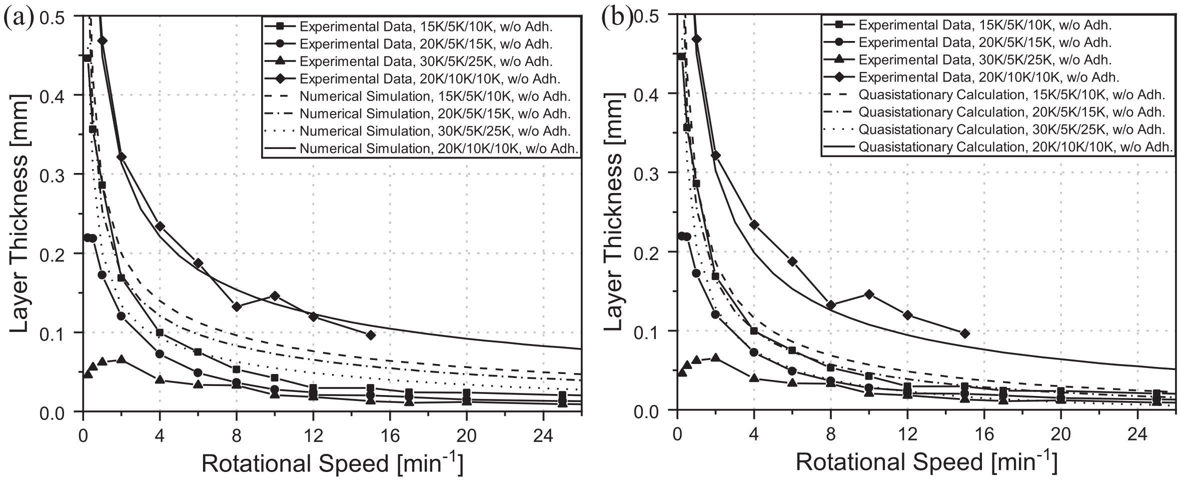

Fig. 14. Comparison of the measured layer thicknesses without adhesion at the rotating drum (a) with the numerical simulation (b) with the Quasi-Steady calculation.

The results of the calculation of the adhesive layer thickness presented in Section 3.1 show that the backflow of liquid adherent PCM has to be considered, which agrees with visual observations during the experiments. Contrary to this, the simulation tool assumes a constant thickness of the adhesion layer thickness in which only heat conduction is considered. Since the backflow of the adhering liquid PCM is only gravimetrically driven and therefore assumed to be laminar, the assumption of radial heat conduction is correct in a first approximation. Nevertheless, the thickness of the adhering liquid PCM layer is underestimated on average by the numerical simulation. This results in faster cool-out of the adhering layer, which can be a reason for the overestimation of the solidified layer thickness in the numerical simulation. The change of the boundary condition at the point of emersion leads to a slight local reduction of the solidified layer thickness due to melting. While a convective boundary condition is assumed within the liquid PCM, this is immediately changed to adhering liquid PCM with uniform temperature at the point of emersion. At this moment, the high temperature gradient at the solidification point leads to a reduction of the layer thickness, followed by further solidification after the adhering liquid PCM layer is cooled down.

For rotational speeds below 2 min^{-1}, the numerical simulation underestimates the experimental data of the heat transfer more compared to higher rotational speeds. In the same way, the layer thickness determinate by the numerical simulation overestimates the experimental data in this range. This is assumed to be an effect of natural convection within the liquid PCM, which exceeds the forced convection at these rotational speeds. Natural convection is not considered in the current models. The research shows the limitations of neglecting natural convection, which becomes dominant for low rotational speeds. The experimental data of fully immersed rotating cylinders given in [8] supports this assumption.

The heat transfer and layer thicknesses are affected by several geometrical and material-specific properties. Especially the material-specific properties of the PCM used are essential and difficult to determine due to the proximity of the melting point. Fig. 15 shows the effect of a change in key properties on heat transfer and the layer thickness. One can see a high influence of the density and the phase change enthalpy of the PCM, followed by the thermal conductivity and the viscosity of the PCM. The temperatures of the rotating drum, namely the temperature of the HTF, the melting temperature of the PCM, the ambient temperature and the temperature of the liquid PCM, also have an influence on the heat transfer and the layer thickness. The influence of a change in these temperatures is shown correspondingly in Fig. 16. A change in the ambient temperature and the temperature of the liquid PCM has comparatively little effect on the heat transfer and the layer thickness, while the influence of a change in the HTF temperature and the melting point of the PCM is much higher. For the melting temperature, which is considered to be 31.5 °C in this work, values between 30.1 °C [41] and 32.15 °C [42] can be identified in the literature. Furthermore, both calculation tools introduced assume a sharp melting point without supercooling.

4. Potential of the rotating drum heat exchanger using a high-temperature PCM

With the introduced numerical simulation, a heat exchanger based on the rotating drum can be calculated for the generation of steam. Thereby, sodium nitrate ($NaNO_3$), whose melting point is 306 °C, is assumed to be the PCM, while the geometrical properties of the rotating drum presented in [1] remain unchanged. The evaporation of the HTF inside the drum significantly increases the internal surface–specific heat transfer coefficient as mentioned in Section 2.2. The use of a high temperature PCM allows an increased temperature difference between both the melting point of the PCM and the evaporating HTF and between the melting point of the PCM and the liquid PCM. The resulting surface-specific heat flux based on the entire surface of the drum is shown in Fig. 17. It is increased for higher temperature differences and for higher rotational speeds and is exceeding 400 $kW \cdot m^{-2}$ for a total temperature difference of 160 K and a rotational speed of 150 min^{-1}. For a comparison of the heat transfer potential of different heat transfer techniques, the coefficient of heat transfer in $W \cdot m^{-2} \cdot K^{-1}$ is given in Fig. 18. The coefficient of heat transfer is strongly nonlinear for different rotational speeds and temperature differences. The nonlinear behavior is mainly based on the nonlinearity of the solidification process. At low temperature differences the coefficient of heat transfer is highest reaching values higher than 5000 $W \cdot m^{-2} \cdot K^{-1}$. With increasing temperature difference, the coefficient of heat transfer decreases regressively. At a temperature difference of 150 K, the coefficient of heat transfer is still exceeding 3000 $W \cdot m^{-2} \cdot K^{-1}$. Compared to values of typical evaporators, which range from 900 $Wm^{-2} \cdot K^{-1}$ to 3000 $W \cdot m^{-2} \cdot K^{-1}$ [43], the rotating drum is competitive, considering that the authors of the study did not perform any optimization with respect to the geometrical characteristics and the design of the rotating drum within the scope of this study. While the high surface–specific heat fluxes at increased temperature differences are well suited for the generation of process steam with high power density, the high coefficients of heat transfer at low temperature differences illustrates the high potential for exergetically efficient heat transfer.

5. Summary and outlook

With the rotating drum heat exchanger, thermal energy from latent heat as well as thermal energy from sensible heat can be transferred with high surface–specific heat flux densities. Thereby, a horizontally rotating

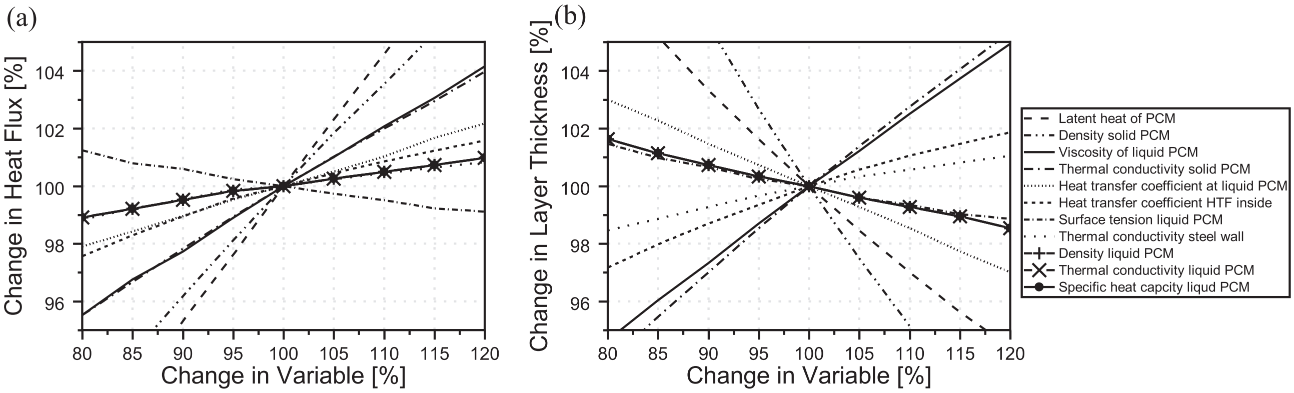

Fig. 15. Sensitivity of the material properties and heat transfer coefficients (a) on the heat flux (b) on the layer thickness.

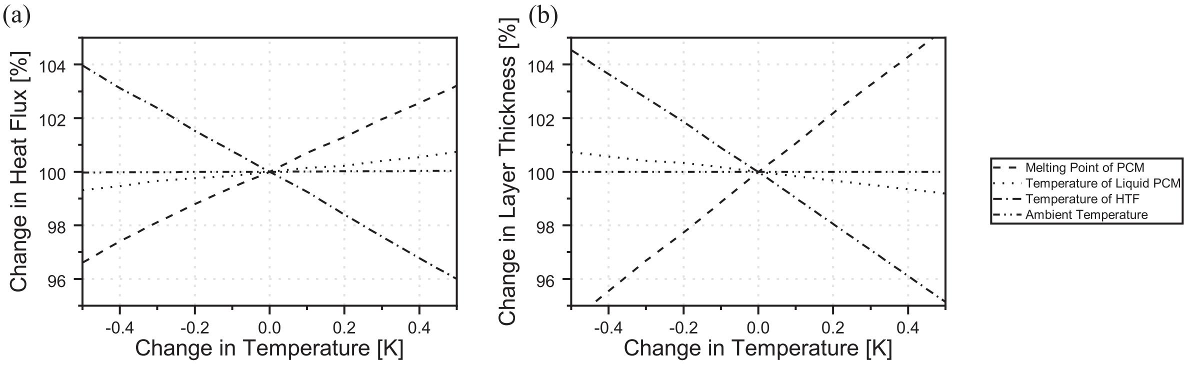

Fig. 16. Sensitivity of the temperatures (a) on the heat flux (b) on the layer thickness.

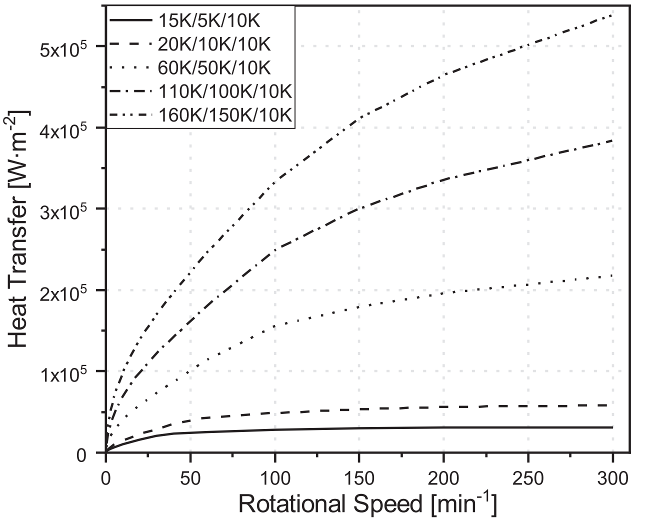

Fig. 17. Heat transfer from the liquid PCM to the HTF at the rotating drum.

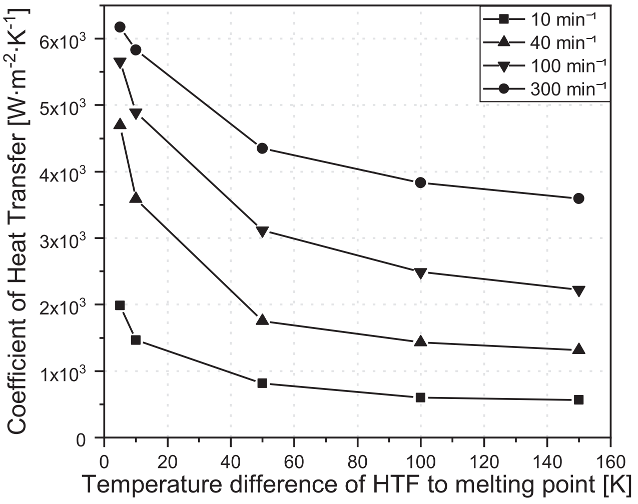

Fig. 18. Total heat transfer coefficient from the liquid PCM to the HTC at the rotating drum.

drum is partially immersed in liquid PCM while a HTF passing through the drum is heated up. At a HTF temperature below the melting point of the PCM, the PCM is solidified on the outer side of the rotating drum. In this case, the solidified PCM layer is removed by a fixed scraper with each rotation. At a HTF temperature above the melting point of the PCM, no solidification occurs and the heat transfer is based on forced convection only. In both cases, liquid PCM adheres to the surface when it is released from the tub, which increases the effective heat transfer surface.

Within this research, two novel calculation approaches for the calculation of the heat transfer as well as the layer thickness of the rotating drum heat exchanger are introduced, with the objective of obtaining a calculation tool for large–scale high–temperature rotating drum heat exchanger for latent heat storage. The first is based on the quasistationary solution of the Stefan-problem. The second is a transient numerical simulation based on the Finite-Differences-Method. For both calculation approaches, a surface coefficient of heat transfer on the outer side of the rotating drum is required. Since this heat transfer problem is similar to a moving surface in a quiescent medium, the correlation of Tsou could be identified, which is also verified for partially immersed cylinders. For the thickness of the liquid PCM adhering to the solidified surface after the drum surfaces emerge from the liquid PCM, a calculation of Landau and Levich could be identified.

The calculation approaches are verified by mathematically exact solutions. For the validation of the calculations, experimental data are available for a temperature difference of up to 10 K between the HTF inside the rotating drum and the melting point of the PCM, and a temperature difference of up to 25 K between the melting point of the PCM and the liquid PCM. The experiments were performed in previously published research on a rotating drum with a diameter of 184 mm at rotational speeds of up to 25 min^{-1} using decanoic acid with a melting temperature of 31.5 K as PCM.

The transferred heat can be calculated qualitatively correctly with both calculation approaches in the case of solidification and in the case of no solidification. Thereby, the transferred heat increases with higher rotational speeds. Furthermore, adhering PCM increases the heat transfer. In case of no solidification, the heat transfer through the heat exchanger wall is mainly affected by the surface coefficient of heat transfer on the outer surface of the rotating drum. When solidification occurs, the released phase change enthalpy of the solidifying PCM affects the heat transfer the most. But also, increasing the external surface coefficient of heat transfer between the moving solidified PCM layer and the liquid PCM increases the heat transfer, while the thickness of the solidified PCM layer decreases in this case. The research shows that the correlation of the surface coefficient of heat transfer of the outer surface identified for no solidification might also be valid in the case of simultaneous solidification. The quasistationary calculation underestimates the heat transfer on average by 37% in case of no solidification and 33% in case of solidification and is therefore only suitable for a rough calculation of a rotating drum heat exchanger. The transient numerical simulation reproduces the heat transfer on average with an accuracy of 9% in case of no solidification and 8% in case of solidification at rotational speeds above 4 min^{-1}. For rotational speeds below 4 min^{-1}, the numerical simulation underestimates the experimental data by 24% on average. For an accurate calculation at low rotational speeds, natural convection has to be included into the model.

Assuming $NaNO_3$ as PCM with a temperature difference of 150 K between an evaporating HTF inside the rotating drum and the melting point of the PCM, a surface-specific heat flux density of up to 500 $\text{kW}\cdot\text{m}^{-2}$ for a rotational speed of 300 min^{-1} can be assumed based on the numerical simulation.

In a next step, the numerical tool will be used for the identification of an optimized design of the rotating drum heat exchanger for latent heat thermal energy storage in an industrial-scale application. For the validation of the numerical simulation of a high-temperature system, an experimental test rig using a high-temperature PCM and direct evaporation within the rotating drum is in planning.

Funding

This research did not receive any specific grant from funding agencies in the public, commercial, or not-for-profit sectors.

CRediT authorship contribution statement

Jonas Tombrink: Conceptualization, Methodology, Investigation, Validation, Visualization, Writing - original draft. **Dan Bauer:** Conceptualization, Funding acquisition, Supervision, Writing - review & editing.

Declaration of Competing Interest

The authors declare that they have no known competing financial interests or personal relationships that could have appeared to influence the work reported in this paper.

References

[1] J. Tombrink, H. Jockenhöfer, D. Bauer, Experimental investigation of a rotating drum heat exchanger for latent heat storage, Appl. Therm. Eng. 183 (2021), 116221, https://doi.org/10.1016/j.applthermaleng.2020.116221.
[2] J. Tombrink, H. Jockenhöfer, D. Bauer, Examination of the heat transfer potential of an active latent heat storage concept, in: Eurotherm Seminar n°112 - Advances in Thermal Energy Storage, Lleida, Spain, 2019.
[3] T. Bauer, D. Laing, R. Tamme, Characterization of Sodium Nitrate as Phase Change Material, Int. J. Thermophys. 33 (2012) 91–104, https://doi.org/10.1007/s10765-011-1113-9.
[4] W.D. Steinmann, The CHEST (Compressed Heat Energy STorage) concept for facility scale thermo mechanical energy storage, Energy 69 (2014) 543–552, https://doi.org/10.1016/j.energy.2014.03.049.
[5] H. Jockenhöfer, W.-D. Steinmann, D. Bauer, Detailed numerical investigation of a pumped thermal energy storage with low temperature heat integration, Energy 145 (2018) 665–676, https://doi.org/10.1016/j.energy.2017.12.087.
[6] T. Naegler, S. Simon, M. Klein, H.C. Gils, Quantification of the European industrial heat demand by branch and temperature level, Int. J. Energ. Res. 39 (2015) 2019–2030, https://doi.org/10.1002/er.3436.
[7] M. Rehfeldt, T. Fleiter, F. Toro, A bottom-up estimation of the heating and cooling demand in European industry, Energy Effic. 11 (2017) 1057–1082, https://doi.org/10.1007/s12053-017-9571-y.
[8] J.T. Anderson, O.A. Saunders, Convection from an isolated heated horizontal cylinder rotating about its axis, Proc. R. Soc. Lond. A 217 (1953) 555–562, https://doi.org/10.1098/rspa.1953.0080.
[9] B. Özerdem, Measurement of convective heat transfer coefficient for a horizontal cylinder rotating in quiescent air, Int. Commun. Heat. Mass. Transf. 27 (2000) 389–395, https://doi.org/10.1016/S0735-1933(00)00119-6.
[10] K.M. Becker, Measurements of convective heat transfer from a horizontal cylinder rotating in a tank of water, Int. J. Heat Mass Transf. 6 (1963) 1053–1062, https://doi.org/10.1016/0017-9310(63)90006-1.
[11] R.I. Elghnam, Experimental and numerical investigation of heat transfer from a heated horizontal cylinder rotating in still air around its axis, Ain Shams Eng. J. 5 (2014) 177–185, https://doi.org/10.1016/j.asej.2013.09.008.
[12] F.K. Tsou, E.M. Sparrow, R.J. Goldstein, Flow and heat transfer in the boundary layer on a continuous moving surface, Int. J. Heat Mass Transf. 10 (1967) 219–235, https://doi.org/10.1016/0017-9310(67)90100-7.
[13] K. Gauler, Wärme- und Stoffübertragung an eine mitbewegte Grenzfläche bei Grenzschichtströmung, Dissertation, Universitaet Karlsruhe, 1972.
[14] H. Martin, B. Gampert, G5 Heat Transfer to Single Cylinders, Wires, and Fibers in Longitudinal Flow, in: VDI e.V. (Eds.), VDI Heat Atlas, Springer, Berlin, Heidelberg, 2010. doi:10.1007/978-3-540-77877-6_38.
[15] V. Gnielinski, G2 Heat Transfer in Concentric Annular and Parallel Plate Ducts, in: VDI e.V. (Eds.), VDI Heat Atlas, Springer, Berlin, Heidelberg, 2010. doi:10.1007/978-3-540-77877-6_35.
[16] M. Kind, D. Steiner, J.M. Chawla, J.-J. Schröder, Y. Saito, H. Auracher, O. Herbst, A. Katsaounis, H3 Flow Boiling, in: VDI e.V. (Eds.), VDI Heat Atlas, Springer, Berlin, Heidelberg, 2010. doi:10.1007/978-3-540-77877-6_124.
[17] W. Wagner, H.-J. Kretzschmar, International Steam Tables - Properties of Water and Steam based on the Industrial Formulation IAPWS-IF97, Springer, Berlin, Heidelberg, 2008. doi:10.1007/978-3-540-74234-0.
[18] L. Landau, B. Levich, Dragging of a Liquid by a Moving Plate, Acta Physicochim URSS 17 (1942) 42–54.
[19] N.I. Gel'perin, G.A. Nosov, A.V. Makotkin, Determinating the thickness of liquid film holdup on a rotating drum surface, Chem. Pet. Eng. 11 (1975) 230–233, https://doi.org/10.1007/BF01146631.
[20] N. Hasan, J. Naser, Determining the thickness of liquid film in laminar condition on a rotating drum surface using CFD, Chem. Eng. Sci. 64 (2009) 919–924, https://doi.org/10.18086/swc.2015.02.05.
[21] Y. Yener, S. Kakaç, Heat Conduction, fourth ed., Taylor & Francis, New York, Abingdon, 2018. doi:10.1201/9780203752166.
[22] H.D. Baehr, K. Stephan, Heat and Mass Transfer, Springer, Berlin, Heidelberg, 2011. doi:10.1007/978-3-642-20021-2.
[23] V. Alexiades, A.D. Solomon, Mathematical Modeling of Melting and Freezing Processes, Hemisphere Publishing Corperation, Washington, London, 1993. doi:10.1201/9780203749449.
[24] M.E. Nakhchi, J.A. Esfahani, Improving the melting performance of PCM thermal energy storage with novel stepped fins, J. Energy Storage 30 (2020), https://doi.org/10.1016/j.est.2020.101424.
[25] G. Xiaohong, L. Bin, G. Yongxian, Y. Xiugan, Two-dimensional transient thermal analysis of PCM canister of a heat pipe receiver under microgravity, Appl. Therm. Eng. 31 (2011) 735–741, https://doi.org/10.1016/j.applthermaleng.2010.10.016.
[26] W.-B. Ye, H.-J. Guo, S.-M. Huang, Y.-X. Hong, Research on melting and solidification processes for enhanced double tubes with constant wall temperature/wall heat flux, Heat Transf. Asian Res. 47 (2018) 583–599, https://doi.org/10.1002/htj.21328.
[27] Y. Hong, W.-B. Ye, S.-M. Huang, J. Du, Can the melting behaviors of solid-liquid phase change be improved by inverting the partially thermal-active rectangular cavity? Int. J. Heat Mass Transf. 126 (2018) 571–578, https://doi.org/10.1016/j.ijheatmasstransfer.2018.06.012.
[28] C. Zhang, J. Li, Y. Chen, Improving the energy discharging performance of a latent heat storage (LHS) unit using fractal-tree-shaped fins, Appl. Energy 259 (2020), 114102, https://doi.org/10.1016/j.apenergy.2019.114102.
[29] X. Zhang, M. Sheikholeslami, W.-M. Yan, A. Shafee, F. Selimefendigil, H. Babazadeh, Energy storage analysis for discharging of nanoparticle enhanced

phase change material within a triplex-tube thermal storage, J. Energy Storage 31 (2020), 101640, https://doi.org/10.1016/j.est.2020.101640.

[30] M. Sheikholeslami, S. Lohrasbi, D.D. Ganji, Numerical analysis of discharging process acceleration in LHTESS by immersing innovative fin configuration using finite element method, Appl. Therm. Eng. 107 (2016) 154–166, https://doi.org/10.1016/j.applthermaleng.2016.06.158.

[31] A. Abhat, Low temperature latent heat thermal energy storage: Heat storage materials, Sol. Energy 30 (1983) 313–332, https://doi.org/10.1016/0038-092X(83)90186-X.

[32] H. Noureddini, B.C. Teoh, L. Davis Clements, Densities of vegetable oils and fatty acids, J. Am. Oil Chem. Soc. 69 (1992) 1184–1188, https://doi.org/10.1007/BF02637677.

[33] D. Rozanna, T.G. Chuah, A. Salmiah, T.S.Y. Choong, M. Sa'ari, Fatty Acids as Phase Change Materials (PCMs) for Thermal Energy Storage: A Review, Int. J. Green Energy 1 (2005) 495–513, https://doi.org/10.1081/GE-200038722.

[34] K.W. Hunten, O. Maass, Investigation of Surface Tension Constants in an Homologous Series from the Point of View of Surface Orientation, J. Am. Chem. Soc. 51 (1929) 153–165, https://doi.org/10.1021/ja01376a018.

[35] Y. Nagasaka, A. Nagashima, The thermal conductivity of molten NaNO3 and KNO3, Int. J. Thermophys. 12 (1991) 769–781, https://doi.org/10.1007/BF00502404.

[36] H. Schinke, F. Sauerwald, Dichtemessungen. Über die Volumenänderung beim Schmelzen und den Schmelzprozeß bei anorganischen Salzen, J. Inorg. Gen. Chem., 304 (1960) 25–36. doi:10.1002/zaac.19603040104.

[37] V.M.B. Nunes, M.J.V. Lourenço, F.J.V. Santos, C.A.N. de Castro, Viscosity of Molten Sodium Nitrate, Int. J. Thermophys. 27 (2006) 1638–1649, https://doi.org/10.1007/s10765-006-0119-1.

[38] J.L. Dahl, F.R. Duke, Surface Tensions of the AgNO3–NaNO3and AgNO3–KNO3Systems, The J. Phys. Chem. 62 (1958) 1142–1143, https://doi.org/10.1021/j150567a034.

[39] J. Stefan, Ueber die Theorie der Eisbildung, insbesondere über die Eisbildung im Polarmeere, Annalen der Physik 278 (1891) 269–286, https://doi.org/10.1016/j.rser.2006.05.005.

[40] H.S. Carlsaw, J.C. Jaeger, Conduction of Heat in Solids, Oxford University Press, Oxford, 1959.

[41] M. Kenisarin, K. Mahkamov, Solar energy storage using phase change materials, Renew. Sustain. Energy Rev. 11 (2007) 1913–1965, https://doi.org/10.1016/j.rser.2006.05.005.

[42] M.C. Costa, M.P. Rolemberg, L.A.D. Boros, M.A. Krähenbühl, M.G. de Oliveira, A.J. A. Meirelles, Solid−Liquid Equilibrium of Binary Fatty Acid Mixtures, J. Chem. Eng. Data 52 (2007) 30–36, https://doi.org/10.1021/je060146z.

[43] W. Roetzel, B. Spang, C3 Typical Values of Overall Heat Transfer Coefficients, in: VDI e.V. (Eds.), VDI Heat Atlas, Springer, Berlin, Heidelberg, 2010. doi:10.1007/978-3-540-77877-6_6.

3.3 Paper III: Design and Application

This article was published in *Applied Energy*, 321, 119325, Copyright Elsevier (2022)

https://doi.org/10.1016/j.apenergy.2022.119325

Applied Energy 321 (2022) 119325

Contents lists available at ScienceDirect

Applied Energy

journal homepage: www.elsevier.com/locate/apenergy

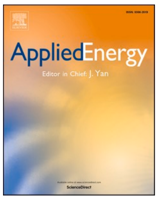

Demand-based process steam from renewable energy: Implementation and sizing of a latent heat thermal energy storage system based on the Rotating Drum Heat Exchanger

Jonas Tombrink *, Dan Bauer

German Aerospace Center (DLR), Institute of Engineering Thermodynamics, Pfaffenwaldring 38-40, 70569 Stuttgart, Germany

HIGHLIGHTS

- Novel, freely scalable design of a Rotating Drum Heat Exchanger for latent heat storage.
- Separation of power and capacity with innovative thermal energy storage system.
- Steam generation with high surface-specific heat transfer above 300 kW·m$^{-2.}$
- Storage density of up to 330 KWh·m^{-3} by using nitrate salts as storage material.

ARTICLE INFO

Keywords:
Rotating Drum Heat Exchanger
Latent heat thermal energy storage
Phase change material
Renewable process steam
Power to heat

ABSTRACT

Today's heat demand of industrial processes is mainly supplied by the combustion of fossil fuels. Within this paper, a thermal energy storage system using the Rotating Drum Heat Exchanger is proposed for a carbon-neutral steam generation and additional co-generation of electricity. At the Rotating Drum Heat Exchanger, a phase change material (PCM) solidifies on the outer surface of a drum, which is partially immersed into liquid PCM, while water evaporates on the inner surface of the drum. With this design, the storage density of the proposed nitrate salts as storage material can be increased up to 330 kW·m^{-3} by utilizing the energy stored within the phase change and the energy stored due to the temperature change of the liquid and solid storage material. The storage system is sized for the generation of 20 000 kg·h^{-1} of saturated steam at 2.5 bar, 8 bar, 20 bars and 75 bar of steam pressure. During the discharge process, a surface-specific heat transfer of above 300 kW·m^{-2} and a share of electricity generation of up to 24 % can be achieved, which shows the high potential of the Rotating Drum Heat Exchanger. The thermal energy storage system can either be charged by fluctuating renewable energy or can be used to decouple the steam and electricity production of today's cogeneration plants. The presented storage system can thus make a decisive contribution to decarbonization and flexibilization of the industrial process steam supply.

1. Introduction

For the transition of today's energy system towards a carbon-neutral and sustainable energy supply, scalable renewable energy sources such as solar and wind needs to be expanded. Since these energy sources fluctuate depending on the availability of solar radiation or wind speed, the energy availability needs to be decoupled of energy demand. This can be achieved by suitable energy storage systems. While today the political and medial focus is on the storage of electricity, 44 % of the energy demand in Europe is thermal energy. The demand of thermal energy in the temperature range between 100 and 400 °C for industrial processes, mainly in form of process steam, amounts to 5 % of the total final energy demand [1]. Storing energy in the form of the required thermal energy offers advantages over electrical storage e.g. in terms of availability of critical resources as rare-earth elements and high purity lithium and cost savings. State-of-the-art large-scale thermal energy storages are two-tank molten salt storages, utilizing the thermal energy stored within the temperature increase of a liquid storage material. These large-scale thermal energy storages were originally developed and commercially used in Concentrated Solar Power Plants (CSP-Plants). While the maximum temperature of such thermal energy storages is

---

* Corresponding author.
E-mail address: jonas.tombrink@dlr.de (J. Tombrink).

https://doi.org/10.1016/j.apenergy.2022.119325
Received 2 February 2022; Received in revised form 31 March 2022; Accepted 22 May 2022

Nomenclature

Latin

a	distance, $[a] = \text{m}$
c	heat capacity, $[c] = \text{J}\cdot\text{kg}^{-1}\cdot\text{K}^{-1}$
c_p	heat capacity at constant pressure, $[c_\text{p}] = \text{J}\cdot\text{kg}^{-1}\cdot\text{K}^{-1}$
D	(drum)diameter, $[D] = \text{m}$
d	(channel)diameter, $[d] = \text{m}$
g	gravimetrical acceleration, $[g] = \text{m}\cdot\text{s}^{-2}$
h	surface coefficient of heat transfer, $[h] = \text{W}\cdot\text{m}^{-2}\cdot\text{K}^{-1}$
k	thermal conductivity, $[k] = \text{W}\cdot\text{m}^{-1}\cdot\text{K}^{-1}$
L	length $[L] = \text{m}$, phase changer enthalpy, $[L] = \text{J}\cdot\text{kg}^{-1}$
$\dot{m}$	mass flow, $[\dot{m}] = \text{kg}\cdot\text{s}^{-1}$
n	rotational speed, $[n] = \text{s}^{-1}$
P	power, $[P] = \text{W}$
p	pressure, $[p] = \text{pa}$
$\dot{q}$	surface-specific heat flux, $[\dot{q}] = \text{W}\cdot\text{m}^{-2}$
R_a	surface roughness, $[R_\text{a}] = \text{m}$
r	radius, $[r] = \text{m}$
s	(wall) thickness, $[s] = \text{m}$
T	temperature, $[T] = {}^\circ\text{C}$
u	(flow-) velocity, $[u] = \text{m}\cdot\text{s}^{-1}$
x	distance, $[x] = \text{m}$
y	distance, $[y] = \text{m}$

Greek

δ	(adhering) layer thickness, $[\delta] = \text{m}$
η	dynamic viscosity, $[\eta] = \text{Pa}\cdot\text{s}$, efficiency, $[\eta] = \%$
ϱ	density, $[\varrho] = \text{kg}\cdot\text{m}^{-3}$
σ	yield strength, $[\sigma] = \text{N}\cdot\text{m}^{-1}$, surface tension, $[\sigma] = \text{N}\cdot\text{m}^{-1}$
Φ	factor of heat transfer surface compared to a flat wall, $[\Phi] = -$
φ	immersion angle, $[\varphi] = {}^\circ$ Deg
ψ	location of scraper, $[\psi] = {}^\circ$ Deg

Mathematical Symbols

d	differential
f	function
$\log_{10}$	logarithm base 10
π	mathematical constant π

Dimensionless Numbers

Re	Reynolds number, $\text{Re} = \varrho\cdot v\cdot x\cdot\eta^{-1}$
Pr	Prandtl number, $\text{Pr} = \eta\cdot c_p\cdot k^{-1}$
Nu	Nusselt number, $\text{Nu} = h\cdot x\cdot k^{-1}$
p^*	reduced pressure, $p^* = p/p_\text{crit}$
x^*	vapor quality, $x^* = m_\text{vapour}/m_\text{total}$

Sub-/Superscripts

0	initial value
$\bar{}$	mean
$'$	saturated liquid
$''$	saturated gas
B	boiling
C	convection
crit	critical
el.gen.	electrical generator
g	gas
HTF	Heat Transfer Fluid
l	liquid
m	melting
max	maximum
min	minimum
PCM	Phase Change Material
res	resulting
s	solid, isentropic
t	tangentially
x	local

limited by the construction material and the decomposition temperature of the storage material, the lower temperature is limited by the solidification temperature of the storage material. Today's commercial CSP plants typically use a non-eutectic mixture of 60 wt% sodium nitrate ($NaNO_3$) and 40 wt% potassium nitrate (KNO_3) as storage material, called Solar Salt. The operating temperature limit is typically between 290 °C and 560 °C [2]. While there is a safety temperature difference to the melting point of about 250 °C that must be maintained to prevent unintentional solidification in the system, the upper temperature limit results from the specific corrosion behavior of the steel used in contact with the high-temperature molten salt [3]. In addition, the Solar Salt used decomposes to nitrites at a temperature above 560 °C, which intensifies the corrosion mechanisms [4].

Latent heat thermal energy storages utilize the phase change enthalpy of a Phase Change Material (PCM) during its phase transition from the solid to the liquid state. Since the phase change of a pure or eutectic mixture of a storage material occurs at a constant temperature, thermal energy can be charged and discharged at a constant temperature close to the melting point. By combining a latent heat thermal energy storage with an additional increase or decrease of the temperature of the liquid or solid phase of the storage material, the thermal energy storage density of the storage material can be optimized. The current focus of the research on latent heat thermal energy storages is to improve the heat transfer within the solid phase of the storage material. Since cost-effective storage materials usually have a low thermal conductivity in the solid state of below 2 $\text{W}\cdot\text{m}^{-1}\cdot\text{K}^{-1}$, nitrate salts even below 0.6 $\text{W}\cdot\text{m}^{-1}\cdot\text{K}^{-1}$ [5], the heat transfer is limited by the growing solid layer of the storage material during the discharge process. Promising and extensively studied solutions for enhancing the heat transfer are the integration of a highly conductive heat transfer structure, e.g. in form of aluminum fins, the encapsulation of the storage material or the enhancement of the thermophysical properties of the storage material, e.g. by the incorporating of nanoparticles [6,7].

The recently developed Rotating Drum Heat Exchanger overcomes the limitation due to the low thermal conductivity of cost-effective storage materials by a continuously scraped surface. The principal of the Rotating Drum Heat Exchanger as the key component of the

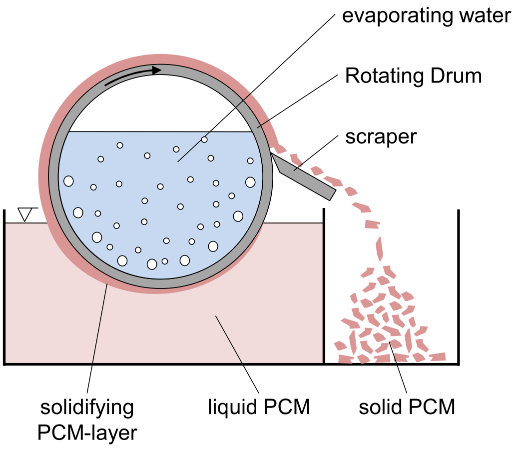

Fig. 1. Principle of the Rotating Drum Heat Exchanger.

proposed thermal energy storage system is shown in Fig. 1. A horizontal drum is partially immersed into liquid PCM. While a fluid evaporates inside the Rotating Drum, the PCM solidifies on the outer side of the drum. The solidified PCM layer is separated from the liquid PCM by the rotation of the drum and removed from the surface of the drum by a stationary scraper just before the surface is re-immersed into the liquid PCM. At the point of emersion, liquid PCM adheres to the solidified PCM-layer, which solidifies after the surface has left the liquid PCM. The solidified PCM can be stored in a separate tank, which provides the possibility of a complete separation of power and capacity of a thermal energy storage system based on the Rotating Drum Heat Exchanger. Therefore, the size of the storage tanks for the storage material and thus the storage capacity of the storage system can be selected independently of the size of the heat exchanger surface, which corresponds to the thermal power of the storage system. The Rotating Drum Heat Exchanger is initially introduced in [8]. There are no general limitations regarding the type of fluid evaporated inside the Rotating Drum and the type of PCM solidified at the outer side of the drum. A detailed description and an experimental investigation of the heat transfer is given in [9]. In [10] a calculation based on the quasi-stationary solution and a detailed transient numerical simulation of the heat transfer is described. The Rotating Drum Heat Exchanger will be integrated into a thermal energy storage system consisting of an electrical or thermal heater and two storage tanks for the cold and hot storage material for the demand-based supply of process steam to industrial processes. These concepts combine the advantages of molten salt thermal energy storages and latent heat thermal energy storages in a unique way. Thus, both the total thermal energy stored in the temperature rise of the liquid storage material and the thermal energy stored in the phase change of the storage material can be transferred to an evaporating liquid with high surface-specific heat density. The lower temperature limit of the storage system can be extended further into the solid state of the storage material. Therefore, also the heat capacity of the solid phase of the storage material can be used, resulting in a higher thermal energy storage density. The ability to store the storage material in the solid state also offers advantages over molten salt storages in terms of downtime and for maintenance of the energy storage system, as unintentional solidification within the cold storage tank is non-critical.

Since carbon-neutral renewable energy will be available mainly in the form of electrical energy, electrical charging is proposed to archive complete decarbonization of the supplied process steam. The electrical energy can be either charged by simple resistive heating or by using high temperature heat pumps. The price of renewable energy generation, especially electricity from photovoltaics, will continue to decrease due to technological progress and scaling effects in the future and become the most cost-effective renewable energy source [11]. In addition, electricity prices fluctuate over time in the liberalized electricity markets of many countries. Prices are lower during periods of low electricity demand or high availability of fluctuating electricity sources, while prices are highest during periods of low availability of fluctuating sources or high demand. Table 1 shows the average 60-minute day-ahead exchange prices of the European Power Exchange (EPEX SPOT) for Germany as an example. While the average price for 2018, 2019 and 2020 was 37.54 € per MWh, the price of electricity could be reduced by 62 % to an average of 14.35 € per MWh if electricity was purchased only in the 20 % of hours with the lowest prices. On the other hand, the revenue from the provision of electrical energy can be increased to an average of 58.94 € per MWh if it is generated only in 20 % of hours with the highest exchange prices. Therefore, the thermal energy storage can be also combined with a conventional steam boiler, a steam turbine and an electrical generator for the demand-based generation of process steam and the provision of electricity only during periods of high electrical energy prices. Further research on the technical feasibility and economic benefits of making industrial steam supply systems more flexible by using electrical energy at different prices and thermal energy storage systems has recently been conducted by Borst et al. [13] and Beck et al. [14]. Thereby, both investigations refer mainly to the system level of the steam supply.

Within this paper, a thermal energy storage system based on the Rotating Drum Heat Exchanger is proposed for the provision of process steam in industry. Thereby, fluctuating electrical energy is charged in form of thermal energy into the thermal storage. The stored thermal energy is discharged on demand in form of process steam. In a first step, the known design of the Rotating Drum Heat Exchanger is adapted to achieve free scalability and to increase the power of the heat exchanger up to the megawatt scale. The mentioned simulation is adopted for the calculation of the novel design. The new design of the Rotating Drum Heat Exchanger, which is presented for the first time, is studied in detail using the introduced simulation to gain specific knowledge regarding the heat transfer characteristic and the influence of certain changes in the characteristics of the design. The Rotating Drum Heat Exchanger serves as the main component of an entire thermal energy storage system, which is presented for the first time in the second part. The possibilities, advantages and limitations of the technology of the Rotating Drum Heat Exchanger and a thermal energy storage system for the (co-) generation of process steam are investigated in detail and concrete findings for further research and commercialization are derived.

2. Optimization of the design and calculation of the Rotating Drum Heat Exchanger

For the use of the Rotating Drum Heat Exchanger for high pressure applications and large scalability, the design has to be modified due to the limitations of Barlow's formula described in the following chapters. Afterwards, the numerical simulation scheme presented and verified in [10] for the calculation of the transferred heat at a Rotating Drum Heat Exchanger is adopted and correlations are identified to determine the surface coefficient of heat transfer inside the drum.

2.1. Simulation of the heat transfer of the Rotating Drum Heat Exchanger

The heat transfer and layer thickness of the Rotating Drum Heat Exchanger is calculated by a transient numerical simulation, introduced in a previous work [10]. The simulation is described in the following section in a short way. All simulation details can be found in the reference. At the simulation, a 1-dimensional section from the Heat Transfer Fluid (HTF) through the steel heat exchanger wall and the solidifying PCM layer towards the liquid PCM is calculated and virtually rotated. Fig. 2 shows the temperature profile within this 1-dimensional cut. While Fig. 2 (a) shows the case at the time when the section is immersed in liquid PCM, Fig. 2 (b) shows the case at the time when liquid PCM adhering to the surface shortly after the surface is emerged from the liquid PCM. Table 2 describes the different heat transfer phenomena shown in Fig. 2. In case of adhering liquid PCM, an additional liquid

Table 1
Day-ahead stock electricity prices in Germany in €/MWh, averaged over the entire years and the average of the highest and lowest 10 %, 20 % and 30 % of the hours [12].

	Mean	Lowest 10 %	Lowest 20 %	Lowest 30 %	Highest 10 %	Highest 20 %	Highest 30 %
2020	30.47	−2.12	6.70	11.70	59.79	52.74	48.60
2019	37.67	6.52	16.85	21.60	61.47	56.04	52.79
2018	44.47	10.65	19.51	24.54	74.67	68.04	63.63

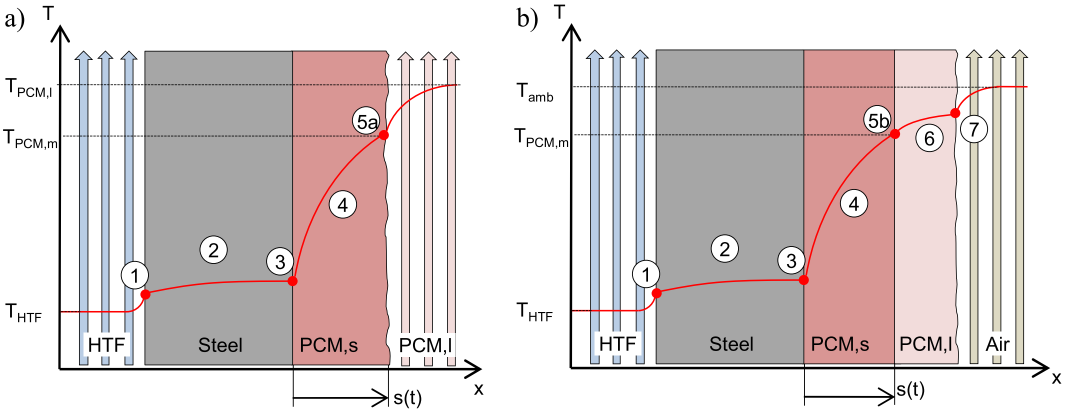

Fig. 2. Temperature profile of the heat transfer (a) during the submersion of the drum surface in liquid PCM (b) during the solidification of adhering liquid PCM while the drum surface is rotating in ambient air (compare Table 2) [10].

Table 2
Description of the heat transfer phenomena at the different locations in Fig. 2.

Location	Heat transfer phenomena
(1)	Convective heat transfer from HTF to steel wall
(2)	Heat conduction within steel wall
(3)	Heat conduction from steel wall to solid PCM
(4)	Heat conduction within solid PCM
(5a)	Point of solidification, equilibrium of heat conduction in steel wall, convective heat transfer from liquid PCM and solidification of PCM
(5b)	Point of solidification, equilibrium of heat conduction in steel wall, heat conduction of liquid PCM and solidification of PCM
(6)	Heat conduction in adhering liquid PCM
(7)	Convective heat transfer from adhering liquid PCM to ambient air

layer whose thickness is calculated according to an equation developed by Gelperin [15],

$$\delta = 0.94 \cdot \left(\frac{\pi \cdot D \cdot n \cdot \eta}{\sigma}\right)^{\frac{1}{6}} \left(\frac{3 \cdot n \cdot D \cdot \eta}{4 \cdot \varrho_l \cdot g \cdot \left(1 - \frac{\varphi}{360}\right)}\right)^{\frac{1}{2}}, \tag{1}$$

is assumed. While the inner boundary condition is convection of evaporating water discussed in Section 2.4, a correlation of the coefficient of heat transfer according to Tsou et al. [16] is used for the outer boundary condition. Thereby, the local Nusselt-Number is calculated as a function of the Prandtl-Number of the liquid fluid

$$\frac{\mathrm{Nu}_x}{\sqrt{\mathrm{Re}_x \cdot \mathrm{Pr}}} = f(\mathrm{Pr}) \tag{2}$$

with the local Reynolds-Number

$$Re_x = \frac{\varrho \cdot u \cdot x}{\eta}. \tag{3}$$

Values for $f(\mathrm{Pr})$ can be found in [16]. The local coefficient of heat transfer can be calculated by rearranging the definition of the Nusselt-Number

$$\mathrm{Nu}_x = \frac{h_x \cdot x}{k}. \tag{4}$$

An implicit finite difference method with a varied time step is used for the discretization. For the virtual rotation of the 1-dimensional section, the outer boundary condition is changed several times per rotation, depending on its position in liquid PCM, adhering PCM or pure heat transfer without solidification, after the adhering layer is completely solidified or scraped off. The simulation, governing equations, and discretization are described in detail in [10] and verified with experimental data at low temperatures published in [8]. The simulation reproduces the experimental data with an accuracy of 8 % on average.

2.2. *Limitations in scaling due to the Barlow's formula*

For a pressurized hollow drum, the Barlow's formula

$$s_{\min} = \frac{p_{\max} \cdot D}{2 \cdot \sigma_{t,\max}} \tag{5}$$

has to be satisfied, which limits the scalability of the Rotating Drum Heat Exchanger due to a required increase in the minimum drum shell thickness with an increased diameter of the drum. Fig. 3 (a) shows the internal pressure in case of a hollow drum. Fig. 4 (a) shows the required wall thickness $s_{\min}$ with increasing diameter of the drum D at different internal pressures $p_{\max}$ according to the Barlow's formula. The assumed yield strength $\sigma_{t,\max}$ of the material is assumed to be 118 $\mathrm{N \cdot mm^2}$ (compare Section 2.6), while an additional required safety factor is neglected for a first estimation. As can be seen, the required wall thickness of the drum increases linearly with the diameter. Fig. 4 (b) shows the resulting specific weight of the drum shell, which increases quadratically with the diameter.

The influence of increasing shell thickness on the heat transfer capability is shown in Fig. 5 for an internal pressure of 75 bar. The material properties of $\mathrm{NaNO_3}$ are assumed for the storage material while the temperature difference between the evaporating water inside the drum and the melting temperature of the PCM, as well as the temperature difference between the melting temperature and the temperature of the liquid storage material, are both assumed to be 100 K. This refers to an average value which is only used for the illustration of the effect of the Barlow's formula on the heat transfer. It is assumed that the entire drum is filled with evaporating water and the surface coefficient of heat transfer of the boiling water is 15 000 $\mathrm{W \cdot m^{-2} \cdot k^{-1}}$, independent of the heat flux. As one can see, the surface-specific heat transfer is highest for small diameters. At a rotational speed of 200 $\mathrm{min^{-1}}$, doubling the diameter from 0.125 m to 0.25 m reduces the surface-specific heat transfer by 40 %. Doubling the diameter from 1 m to 2 m reduces the surface-specific heat transfer by 49 %. A hollow barrel is therefore not freely scalable and is limited in its geometric size.

2.3. *Multiple channels inside the drum shell*

For a free scalability of the Rotating Drum Heat Exchanger, the design of the Rotating Drum needs to be decoupled from the Barlow's formula. This can be achieved by several small holes in the drum shell, whose diameter can be chosen independently of the overall diameter of the drum. Therefore, the overall diameter can be chosen with respect to the required total solidification surface, while the diameter of the channels in the drum shell can be chosen based on the Barlow's formula

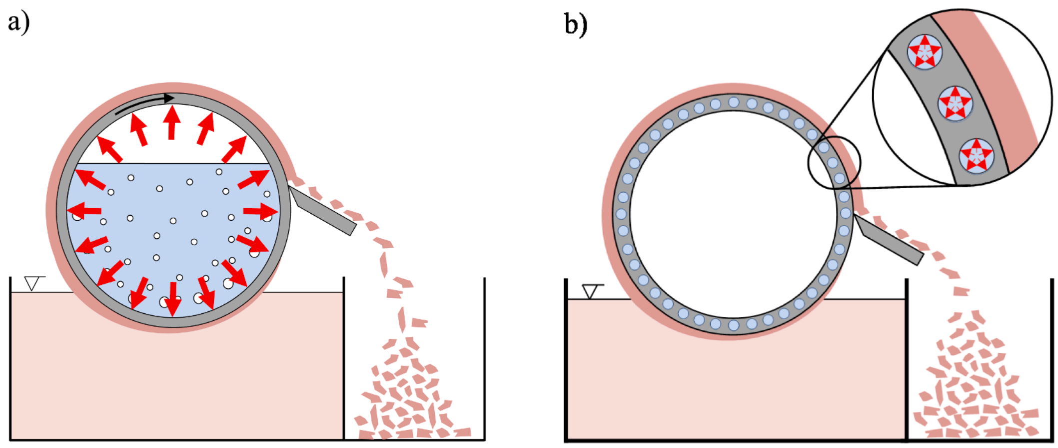

Fig. 3. Internal pressure (a) within a hollow drum and (b) within the channels of the multiple–channel drum.

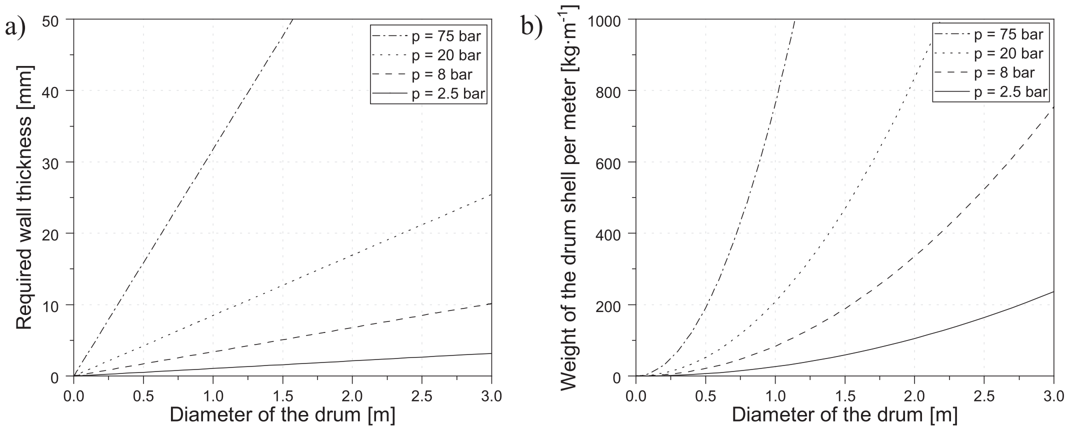

Fig. 4. a) Required wall thickness for different diameter according to the Barlow's formula for different pressure levels, b) specific weight of the drum shell per meter of drum length.

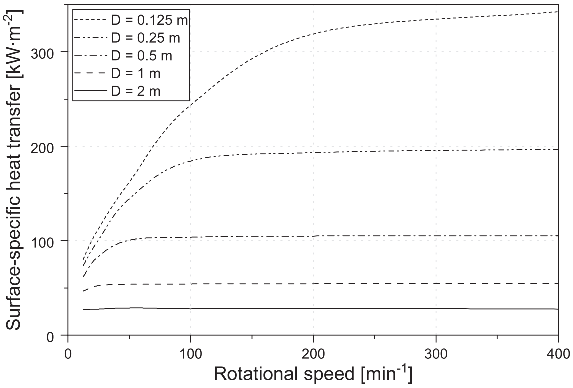

Fig. 5. Surface-specific heat transfer of a hollow drum with a wall thickness according to the Barlow's formula (eq. (1)) with an internal pressure of 75 bar at different diameters D.

with respect to the required wall thickness. Fig. 3 (b) shows an illustration of the so-called multiple-channel drum as well as the internal pressure within the multiple channels of the drums shell. According to equation (5), the required wall thickness of the single channels is in the range of a few millimeters for channels with a feasible diameter and an internal pressure of up to 75 bar. The required wall thickness is therefore not dependent on Barlow's formula, but on manufacturing aspects such as tolerances and technical limitations during the drilling process. While the radial forces of the Rotating Drum are eliminated with the multiple-channel drum, the axial forces remain unchanged compared to a hollow drum. Since the axial force is only half of the radial force of a pressurized cylinder, the required material thickness of the used head can be reduced. In addition, no heat is transferred at the head of the drum, so it can be designed without concerns about heat transfer.

The numerical simulation has to be adapted for the calculation of the multiple-channel drum. Fig. 6 a) shows the ideal arrangement of multiple channels within the shell of the drum. Here, the channels are tangentially in contact with each other. In this theoretical case, the heat transfer surface is increased by a factor of

$$\Phi = \frac{\pi}{2} \tag{6}$$

compared to a flat wall. The thickness of the steel wall of the heat exchanger is adjusted to the mean value of the distance to the heat transfer surface. This can be calculated by the mean value of the equation of the circle by

$$\bar{y} = \frac{1}{r}\int_0^r \sqrt{r^2 - x^2}dx. \tag{7}$$

With $x = r$ and $r = d/2$ one gets.

$$\bar{y} = d\cdot\frac{\pi}{8}. \tag{8}$$

The resulting mean thickness of the heat exchanger wall is calculated by.

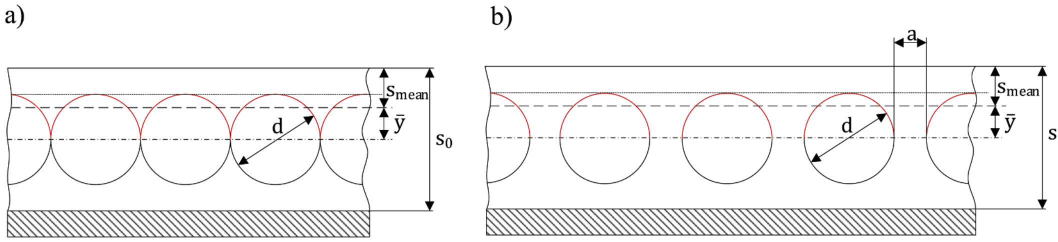

Fig. 6. a) Ideal arrangement and b) Real arrangement of the multiple channels within the drum shell.

$$s_{\text{mean}} = \frac{s_0}{2} - \bar{y}. \tag{9}$$

In case of a real arrangement, the single channels are arranged with a certain distance a between each other, as shown in Fig. 6 b). When only the upper side of the channels is assumed as the active heat transfer surface, the heat transfer surface is changed by the factor calculated by

$$\Phi = \frac{\pi \cdot d}{2 \cdot (d + a)}, \tag{10}$$

while the thickness of the heat exchanger wall is calculated equally to equation (9). Within this study, the distance a between the channels is always chosen to meet $\Phi = 1$ to ensure a feasible distance between the channels, while the total heat transferring surface is that of a plane wall.

2.4. Correlations for the surface coefficient of heat transfer of boiling water

For an accurate simulation of the heat transfer of the Rotating Drum Heat Exchanger, suitable correlations are required for the calculation of the inner heat transfer coefficient of boiling water, which are identified within this section.

2.4.1. Pool boiling for the hollow drum

No specific correlation could be identified for the heat transfer coefficient of boiling water under free convection in a hollow rotating cylinder. Therefore, the correlation of Gorenflo [17], also described in [18], is used for pool boiling of saturated water.

The surface coefficient of heat transfer can be calculated by

$$\frac{h_B}{5580\frac{\mathrm{W}}{\mathrm{m^2K}}} = \left(\frac{\dot{q}}{\frac{20000\mathrm{W}}{\mathrm{m^2}}}\right)^{0,9-0,3p^{*0,15}} \cdot \left(1.73p^{*0,27} + \left(6.1 + \frac{0.68}{1 - p^{*2}}\right)p^{*2}\right) \cdot \left(\frac{R_a}{0.4 \cdot 10^{-6}\mathrm{m}}\right)^{\frac{2}{15}} \cdot \left(\frac{\sqrt{k\varrho c}}{35350\frac{\mathrm{J}}{\mathrm{s^{0.5}m^2K}}}\right)^{\frac{1}{2}} \tag{11}$$

with the surface-specific heat flux $\dot{q}$, the reduced pressure $p^* = p/p_{\text{crit}}$, the surface roughness R_a of the heat transfer surface and the thermal conductivity k, density ϱ and heat capacity c of the heat exchanges material. As applies.

$$h = f(\dot{q}), \tag{12}$$

the surface coefficient of heat transfer has to be found by iteration. Since the rotation of the drum is neglected, the surface coefficient of heat transfer tends to be underestimated.

2.4.2. Forced convection boiling within multiple channel shell drum

If the multiple channels in the shell of the drums are considered individually, they correspond to a rotating pipe on which a centrifugal force acts. Since no correlation could be identified for the estimation of the surface coefficient of heat transfer in this case, the heat transfer problem is reduced to stationary horizontal pipes. The rotation of the channels and the centrifugal forces are therefore neglected, which tends to an underestimation of the calculated surface coefficient of heat transfer. The estimation of the surface coefficient of heat transfer is done according to [19]. The surface coefficient of heat transfer can be calculated for the whole range of saturated boiling, convective boiling and the transition region by.

$$h = \sqrt[3]{h_C^3 + h_B^3}. \tag{13}$$

Thereby, h_B is calculated according to equation (11) and h_C is calculated by the correlation of Steiner

$$\frac{h_C}{h_l} = \left\{(1 - x^*)^{0.01}\left[(1 - x^*) + 1.2x^{*0.4}\left(\frac{\varrho'}{\varrho''}\right)^{0.37}\right]^{-2.2} + x^{*0.01}\left[\frac{h_g}{h_l}\left(1 + 8(1 - x^*)^{0.7}\left(\frac{\varrho'}{\varrho''}\right)^{0.67}\right)\right]^{-2}\right\}^{-0.5} \tag{14}$$

with the surface coefficient of heat transfer h_l and h_g of pure liquid or gaseous flow. In case of turbulent flow, which is the case for high Reynolds-Numbers

$Re > 2300$

h_l and h_g are calculated out of the Nusselt-number

$$Nu = \frac{h_l \cdot d}{k} \tag{15}$$

by

$$Nu = \frac{(\xi/8)(Re - 1000)Pr}{1 + 12.7\sqrt{(\xi/8)}\left(Pr^{\frac{2}{3}} - 1\right)} \tag{16}$$

with

$$\xi = (1.82\log_{10}Re - 1.64)^{-2}. \tag{17}$$

In case of laminar flow, the Nusselt-number is calculated by

$$Nu = \sqrt[3]{3,66^3 + 1,077^3 \cdot Re \cdot Pr}. \tag{18}$$

For short pipes with

$d/L > 1$

and within the transition area from laminar to turbulent flow

$2300 \leq Re \leq 5 \cdot 10^4$

the highest value of equation (16) or equation (18) has to be used for the calculation of the surface coefficient of heat transfer.

2.5. Choose of the storage materials

The selection of a suitable storage material depends on several material-specific and economic properties. First of all, an ideal storage material has to have a suitable melting point in the range between 150 °C and 400 °C. In addition, the storage material should have a high storage density, which includes a high phase change enthalpy and a high specific heat capacity. The storage material should be non-toxic and non-corrosive, available in large quantities, and economically favorable. A large number of possible storage material have been proposed within the literature for high temperature thermal energy storage, among others nitrate-, chloride- and carbonate salts but also metals and mixtures of the materials [20–22]. In this study, sodium nitrate ($NaNO_3$) with a melting point of 306 °C and the eutectic mixture of sodium nitrate and potassium nitrate ($NaNO_3/KNO_3$) with a melting point of 222 °C are proposed as storage material. The liquid phase behavior of these materials is already known from industrial size two-tank molten salt storages [31]. The use of nitrate salts as PCM is already known from several laboratory scale heat storages [23,28,32,33]. The well-known behavior and the cost-effective availability qualifies the use of pure $NaNO_3$ and the eutectic mixture of $NaNO_3/KNO_3$ for the use as storage material within the Rotating Drum heat storage system. The material properties of $NaNO_3$ are given in Table 3 and the material properties of the eutectic mixture of $NaNO_3/KNO_3$ are given in Table 4.

Table 3
Thermophysical properties of sodium nitrate ($NaNO_3$) [10].

Description	Variable	Value	Unit	Remark	Source
Melting point	$T_{PCM,m}$	306	°C		[23]
Phase change enthalpy	L_{PCM}	178	$kJ \cdot kg^{-1}$		[23]
Thermal conductivity, liquid	$k_{PCM,l}$	0.514	$W \cdot m^{-1} \cdot K^{-1}$	at 317 °C	[24]
Thermal conductivity, solid	$k_{PCM,s}$	0.73	$W \cdot m^{-1} \cdot K^{-1}$	at 246 °C	[23]
Density, liquid	$\varrho_{PCM,l}$	1908	$kg \cdot m^{-3}$	at 306 °C	[25]
Density, solid	$\varrho_{PCM,s}$	2113	$kg \cdot m^{-3}$	at 306 °C	[25]
Viscosity	$\eta_{PCM,l}$	0.00285	Pa·s	at 317 °C	[26]
Heat capacity, liquid	$c_{p,PCM,l}$	1.655	$kJ \cdot kg^{-1} \cdot K^{-1}$	at 306 °C	[23]
Heat capacity, solid	$c_{p,PCM,s}$	1.384	$kJ \cdot kg^{-1} \cdot K^{-1}$	at 150 °C	[23]
Surface tension	$\sigma_{PCM,l}$	0.1196	$N \cdot m^{-1}$	at 316 °C	[27]

Table 4
Thermophysical properties of the eutectic mixture of sodium nitrate and potassium nitrate (NaNO3/KNO3).

Description	Variable	Value	Unit	Remark	Source
Melting point	$T_{PCM,m}$	222	°C		[28]
Phase change enthalpy	L_{PCM}	108	$kJ \cdot kg^{-1}$		[28]
Thermal conductivity, liquid	$k_{PCM,l}$	0.4574	$W \cdot m^{-1} \cdot K^{-1}$	222–400 °C	[28]
Thermal conductivity, solid	$k_{PCM,s}$	0.3835	$W \cdot m^{-1} \cdot K^{-1}$	at 100 °C	[28]
Density, liquid	$\varrho_{PCM,l}$	1965	$kg \cdot m^{-3}$	at 222 °C	[25]
Density, solid	$\varrho_{PCM,s}$	2055	$kg \cdot m^{-3}$	at 222 °C	[25]
Viscosity	$\eta_{PCM,l}$	0.00472	Pa·s	at 247 °C	[29]
Heat capacity, liquid	$c_{p,PCM,l}$	1.492	$kJ \cdot kg^{-1} \cdot K^{-1}$	222–350 °C	[28]
Heat capacity, solid	$c_{p,PCM,s}$	1.355	$kJ \cdot kg^{-1} \cdot K^{-1}$	at 202 °C	[30]
Surface tension	$\sigma_{PCM,l}$	0.1222	$N \cdot m^{-1}$	at 237 °C	[29]

Table 5
Reference case of the Rotating Drum Heat Exchanger.

Description	Variable	Value	Unit	Remark
Diameter	D	1	m	see Fig. 7
Length	L	1	m	
Total shell thickness	s_0	0.02	m	see Fig. 7
Diameter of channels	d	0.01	m	see Fig. 7
Mean thickness of wall	s_{mean}	0.006073	m	equation (9)
Immersion angle	φ	90	°	see Fig. 7
Location of scraper	ψ	270	°	see Fig. 7
Storage material		$NaNO_3$		
HTF		Water		
Saturation temperature of HTF	$T_{s,HTF}$	127.4	° C	
Saturation pressure of HTF	$P_{s,HTF}$	2.5	bar	
Temp. of liquid storage material	$T_{l,PCM}$	350	°C	

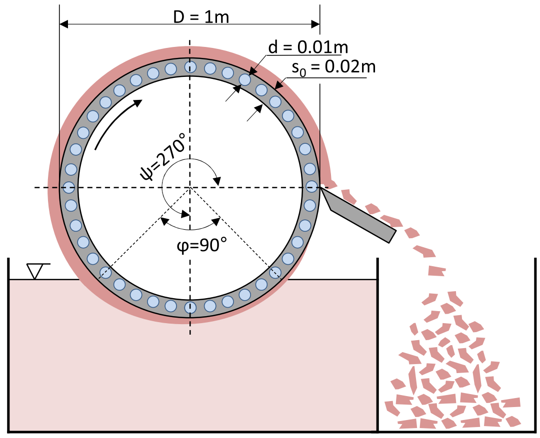

Fig. 7. Principle of the multiple-channel drum and properties of the reference case given in Table 5.

2.6. Choose of a construction material

The construction material of the Rotating Drum Heat Exchangers has to be selected with respect to possible corrosion mechanisms and mechanical stress at a temperature of up to 560 °C. In general, common austenitic stainless steel, e.g. 304, 316 L, 321 and 347 h shows satisfactory corrosion resistance for molten salts applications at temperatures up to 570 °C, but impurities, the atmosphere and thermal cycling can affect the corrosion resistance [34–38]. The scrapping of the solid PCM may also affect the surface, as potential protective layers of the material could also be removed. Therefore, further research has to be carried out in this regard while higher grad materials such as IN625 are also available as an alternative [39]. In this study, the thermophysical properties of AISI 321, similar to EN 1.4541 are used [40,41]. Its minimum 0.2 % proof strength at 550 °C is 118 $\mathrm{N{\cdot}mm^{-2}}$ [42].

2.7. Discussion of the design parameters of the Rotating Drum Heat Exchanger

The design of the multiple-channel drum is discussed in this section. For this purpose, a base case of a drum is defined in Table 5 and a change in the design properties and its effect on the heat transfer is discussed. The properties of the data given in Table 5 are visualized in Fig. 7. The surface-specific heat transfer given in the following sections is always averaged over the entire outer surface and therefore refers to the entire outer surface of the Rotating Drum.

2.7.1. Length of the drum, diameter of the multiple channels and Reynolds-Number inside the multiple channels

The Reynolds-Number in the channels within the drum shell affects the surface coefficient of heat transfer according to the correlations presented in Section 2.4. Besides the specific properties of the fluid, such as density and viscosity, the Reynolds-Number is affected by the diameter of the channels and the mass flow through the channels. Assuming a mass flow through the drum that is always controlled to just achieve a complete phase change, the mass flow through the drum increases as the length of the drum increases. The effect of changing the drum length on the Reynolds-Number of saturated water and saturated liquid in this case is shown in Fig. 8. For the reference drum with a length of 1 m, the Reynolds-Number of the liquid ranges around 1000 and that of the steam around 20 000. Increasing the length to 8 m increases the Reynolds-Numbers by a factor of around 8.5. Reynolds-Numbers of less than 200 for liquid water and less than 3000 for steam are possible at a drum length of 0.25 m. The resulting surface coefficients of heat transfer, calculated according to the equations given in Section 2.4, are shown in Fig. 9. While the surface coefficient of heat transfer increases with higher Reynolds-Numbers at a drum length of 8 m up to 40 000 $\mathrm{W{\cdot}m^{-2}{\cdot}K^{-1}}$, the surface coefficient of heat transfer does not decrease to below 10 000 $\mathrm{W{\cdot}m^{-2}{\cdot}K^{-1}}$ for small drum length and Reynolds-Numbers even at higher rotational speeds. This results from the combination of pool boiling and forced convection boiling according to equation (13). Since the pool boiling term in equation (13) is not affected by the mass flow, the surface coefficient of heat transfer does not decrease further at small drum length. The effect on the total heat transfer of the Rotating Drum is shown in Fig. 10. Here, the resulting surface-specific heat transfer of the Rotating Drum is given in $\mathrm{kW{\cdot}m^{-2}}$. The heat transfer varies by a maximum of 12 % between a drum length of 0.25 m and 8 m, which shows that the Reynolds-Number within the Rotating Drum has a minor effect on the heat transfer at the Rotating Drum.

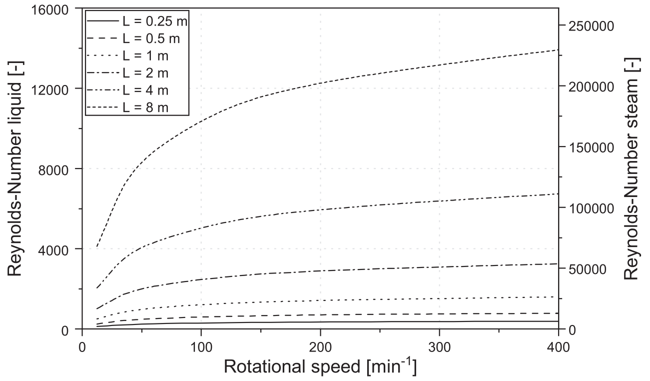

Fig. 8. Reynolds-Number of saturated water and saturated steam within the multiple–channel drum in the reference case for different drum lengths L.

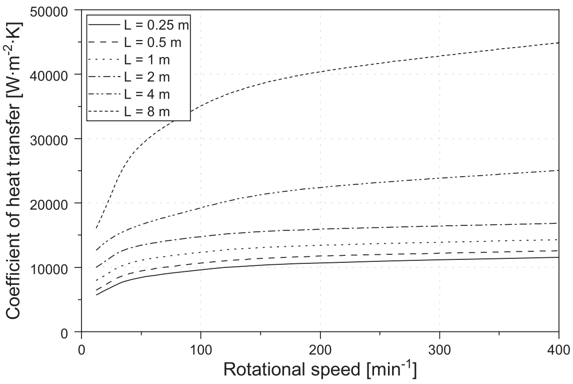

Fig. 9. Surface–specific coefficient of heat transfer of evaporating water within the multiple–channel drum in the reference case for different drum lengths L.

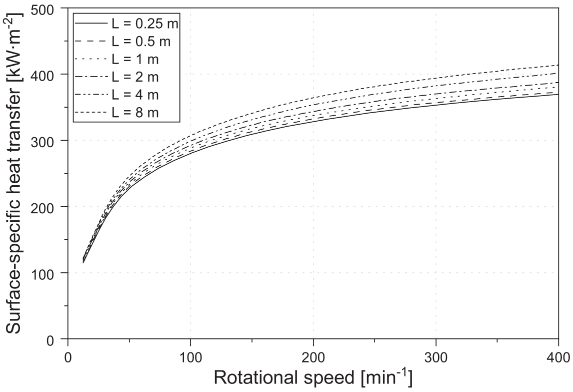

Fig. 10. Surface–specific heat transfer for the multiple–channel drum in the reference case for different drum lengths L.

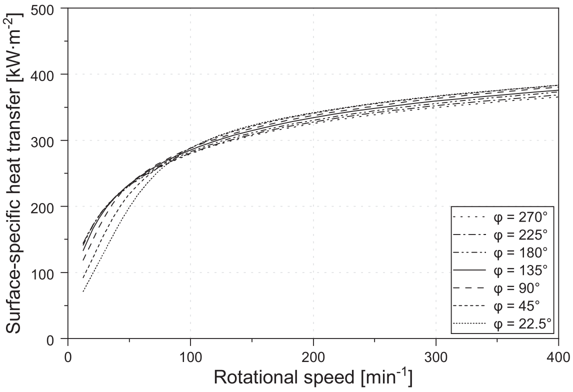

Fig. 11. Surface–specific heat transfer for the reference case when varying the immersion angle φ.

2.7.2. Immersion depth of the drum

In order to achieve a separation of the solidified PCM from the liquid PCM and thus a complete separation of power and capacity, the scraper needs to be located outside of the liquid PCM. Therefore, the drum can only be partially immersed in liquid PCM. Fig. 11 shows the surface-specific heat transfer of the reference case for different immersion depths. The position of the scraper is always adjusted to ensure that an area of 45° of free surface remains after the PCM has been scraped off the drum surface before the surface is immersed in the liquid PCM again. For high rotational speeds above 100 $\mathrm{min^{-1}}$, the influence of the different

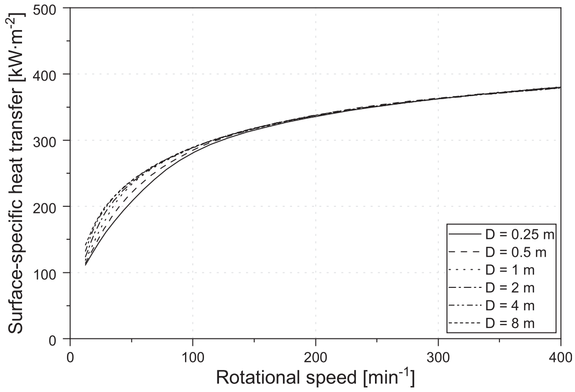

Fig. 12. Surface-specific heat transfer of the Rotating Drum when varying the total diameter D of the multiple–channel drum.

immersion depth is well below 10 % and thus negligible, since adhering liquid PCM covers the drums surface up to the scraper. At low immersion angles of 45° and lower, the adhering liquid PCM has more time for solidification, since the main part of the surface is not immersed in liquid PCM. In case of an immersion angle of 180°, a surface part of the drum is immersed half of the time of one rotation in liquid PCM and 37.5 % of the time of on rotation remain for the solidification of the adhering liquid PCM. In case of a decreased immersion angle of 45°, a surface element is immersed in liquid PCM for only 12.5 % of the time of one rotation and 75 % of the time of one rotation remains for the solidification of adhering liquid PCM. If the adhering liquid PCM has completely solidified by the time it reaches the scrapper, the heat transferred is decreased, since no solidification occurs at this surface. When only solid PCM reaches the scraper, the scraped-off solid PCM can be transferred directly into the cold storage tank. If liquid PCM is also scraped off by the scraper, the solid PCM has to be separated from the liquid PCM to ensure a high utilization of the storage material. In general, the influence of the immersion depth can be controlled by changing the rotational speed. The immersion depth is therefore of secondary interest for the heat transfer capability of the Rotating Drum Heat Exchanger and can be selected with regard to other design parameters, e.g. the design of the scraper and the sealing.

2.7.3. Diameter of the drum

An increase in the drum diameter affects the heat transfer mainly due to an increased speed of movement of the drum surface and thus an increased adhesion layer thickness. As can be seen in Fig. 12, a change of the drum diameter at rotational speeds above 150 min^{-1} results in a minor change of the heat transfer of less than 1 %. In this range, the entire surface is wetted by adhering liquid PCM. An increased adhering layer thickness therefore does not lead to an increased heat transfer. At lower rotational speeds, the specific heat transfer at the surface changes slightly, since the adhering layer thicknesses decreases for lower drum diameter. Thus, the adhering layer of liquid PCM solidifies completely before it reaches the scrapper. At a rotational speed of 25 min^{-1}, the surface-specific heat transfer increases by 7 % when the diameter of the drum is doubled from 1 m to 2 m due to the additional amount of adhering PCM, which adheres and therefore solidifies at the surface. In general, changing the diameter of the multiple-channel drum has only a minor effect on the heat transfer. Therefore, the diameter can be selected with minor regards to the surface-specific heat transfer, resulting in a free scalability.

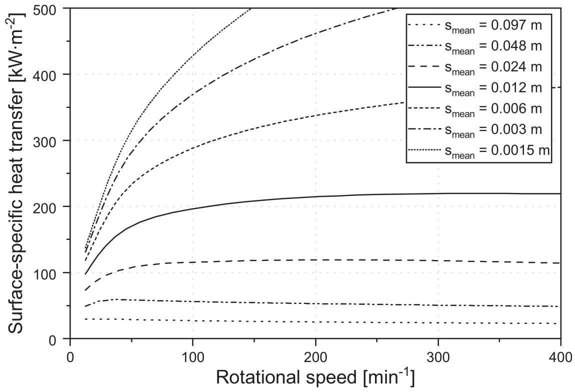

Fig. 13. Surface-specific heat transfer for the reference case when varying the heat transferring wall thickness s_{mean} of the drum.

2.7.4. Mean thickness of the heat exchanger wall

The thickness of the drum's heat transfer wall according to equation (9) depends mainly on the technical possibilities during manufacture as mentioned in Section 2.3, since the wall thickness required to withstand the drum's internal pressure can be controlled by the channel's diameter according to equation (5) as well. Although steel has a high thermal conductivity compared to the solid PCM used, the thermal resistance of the heat exchanger wall still dominates the heat transfer due to the very low thicknesses of the solid PCM. Therefore, increasing the thickness of the heat exchanger wall results in a reduced heat transfer at the Rotating Drum, as shown in Fig. 13. Doubling the mean thickness of the reference case from 0.006 m to 0.012 m decreases the heat flux by 31 % at a rotational speed of 100 min^{-1}. Halving the mean thickness to 0.003 m increases the heat transfer by 21 %. Thus, a variation of the thickness of the heat exchanger wall has a major effect on the heat transfer of the Rotating Drum Heat Exchanger. This significant dependence of the wall thickness on the heat transfer illustrates the dominating part of the steel wall on the total heat transfer resistances. The heat transfer resistances of the thin solid PCM-layer at the outer side and the evaporating water at the inner side of the drum are comparatively low. At very low mean thicknesses of the steel wall, a change in the rotational speed affects the heat transfer significant more compared to higher values of the mean thickness. Since the thermal resistance of the steel wall is decreased at low mean thicknesses of the steel wall, the solid PCM layer becomes the dominating part of the heat transfer resistances. Thus, a decreased average solid PCM layer thickness due to higher rotational speeds has a larger effect on the heat transfer.

2.8. Influence of the temperature differences on the heat transfer of the Rotating Drum Heat Exchanger

The total temperature difference at the Rotating Drum Heat Exchanger can be divided into the temperature difference between the melting point of the PCM and the saturation temperature of the HTF

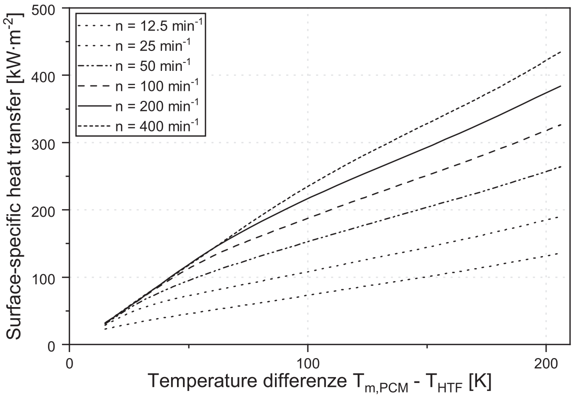

Fig. 14. Surface–specific heat transfer for the reference case when varying the temperature difference between the saturation temperature of the HTF and the melting point of the PCM.

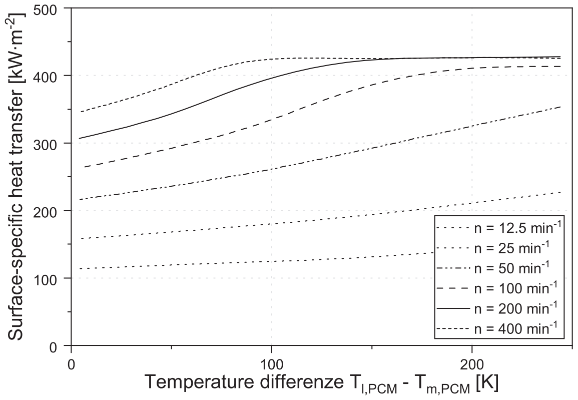

Fig. 15. Surface–specific heat transfer for the reference case when varying the temperature difference between the melting point of the PCM and the temperature of the liquid PCM.

$\Delta T_{m,PCM\text{-}HTF}$ and the temperature difference between the melting point of the PCM and the temperature of the liquid PCM $\Delta T_{l,PCM\text{-}m,PCM}$. While only the total temperature difference is crucial for the exegetic losses of a thermodynamic cycle, the heat transfer at the Rotating Drum Heat Exchanger is clearly dominated by the temperature difference between the melting point of the PCM and the saturation temperature of the HTF. Fig. 14 shows the surface-specific heat transfer of the reference case of the Rotating Drum Heat Exchanger in dependence of the temperature difference $\Delta T_{m,PCM\text{-}HTF}$ for different rotational speeds. For high temperature differences and low rotational speeds, the increase of the heat transfer is almost linear with the increase of the temperature difference. At low temperature differences, an increase in the rotational speed of the Rotating Drum does not result in a further increase of the heat transfer. Thus, an increase of the rotational speed from 100 min^{-1} to 400 min^{-1} at a temperature difference of 60 K increases the heat transfer by only 8 %, while the same increase of the rotational speed increases the heat transfer at a temperature difference of 180 K by 32 %. The rotational speed mainly affects the average layer thickness of the solidified PCM and thus the heat transfer within solid PCM layer. At low temperature differences, the steel wall of the heat exchanger becomes the dominant part of the heat transfer resistances at lower rotational speeds. This explains the nonlinear behavior of the heat transfer. The influence of the temperature difference between the melting point of the PCM and the temperature of the overheated liquid PCM $\Delta T_{l,PCM\text{-}m,PCM}$ is shown in Fig. 15. Since $NaNO_3$ with a melting point of 306 °C is assumed as PCM, the temperature difference shown refer to an absolute temperature of the liquid PCM between 310 °C and 550 °C. At a rotational speed of 12.5 min^{-1}, the heat transfer increases by 30 % when the temperature difference is increased from 4 K to 244 K. The increase of the heat transfer with the same increase of the temperature difference is highest for a rotational speed of 50 min^{-1} with 63 %. At high rotational speeds, the increase of the heat transfer with increased temperature differences approaches a limit value of around 425 kW·m^{-2}. This is due to the increased heat transfer from the overheated liquid PCM towards the outer solidification surface. Since the heat transfer from the overheated liquid PCM dominates the heat transfer at the moving surface, no further solidification takes place, resulting in a purely convective heat transfer.

3. Novel concepts for the generation of process steam and the cogeneration of electricity

The introduced Rotating Drum Heat Exchanger can be used for the conception of an innovative latent heat thermal energy storage system, which is predestined for the generation of process steam and the cogeneration of process steam and electricity. For this purpose, four different pressure levels are defined, which are widely used in the industry:

- Saturated steam at a pressure of 2.5 bar (abs), corresponding to a saturation temperature of 127.4 °C, is required for the food industry e.g. the sugar production and the dairy industry [43,44].
- Saturated steam at a pressure of 8 bar (abs), corresponding to a saturation temperature of 170 °C, is required primarily in the paper industry [44–46].
- Saturated steam at a pressure of 20 bar (abs), corresponding to a saturation temperature of 215 °C, is defined for use in the chemical industry [47].
- Saturated steam at a pressure of 75 bar (abs), corresponding to a saturation temperature of 290 °C, is defined as the maximum available steam pressure when using sodium nitrate as a storage material for the (co-)generation of electricity.

The power of a reference thermal energy storage system discussed in this paper is defined to generate 20 000 kg·h^{-1} of saturated steam, which would be sufficient to replace about a quarter of the steam generator used in the United States [48]. This results in a required thermal power for the evaporation of the saturated water depending on the pressure level between 12.1 MW in case of 2.5 bar and 8.2 MW in case of 75 bar. The thermal capacity of the storage system is defined to meet at least 24 h of demand, resulting in a capacity of 360 MWh. Depending on the renewable energy sources used and the geographical location of the storage system, this would be sufficient to achieve an availability of the storage system of 90 % if the storage system is charged only with renewable energy. A higher availability of the storage system would exponentially increase the cost of the storage system [49,50]. Therefore, this paper also discusses the integration of a backup boiler fueled by fossil fuel or hydrogen to meet 100% availability of process steam. Pure sodium nitrate with a melting point of 306 °C and the eutectic mixture of sodium nitrate and potassium nitrate with a melting point of 222 °C are selected as the storage materials, as discussed in Section 2.5. While the focus of this research lies on the discharge process of the thermal energy storage system in form of process steam, an electrical charging mainly by resistive heaters is proposed and described in the following section.

3.1. Pure generation of process steam from stored renewable energy

The basic thermal energy storage system, including a hot and a cold storage tank for the storage material, an electrical heater for charging and a Rotating Drum Heat Exchanger for the discharging process, is shown in Fig. 16. When renewable electricity is available, liquid PCM is pumped from the cold storage tank to an electrical heater. In this heater, the liquid PCM is heated up to the maximum possible temperature, which is in general the decomposition temperature of the storage material or the maximum temperatures of the components of the storage system. The majority of the heated PCM is pumped into the hot storage tank. To ensure a pumpable liquid fraction in the generally solid cold storage tank, a minor part of the heated PCM is pumped back into the cold storage tank to melt parts of the solid PCM. For the provision of steam, liquid PCM is pumped from the hot storage tank into the Rotating Drum Heat Exchanger. While water evaporates in the drum, the liquid PCM solidifies on the outer surface of the drum. The solidified PCM is scraped off the drum and transported into the cold storage tank. This can be done by gravity or by a suitable transport system, e.g. a belt conveyor or screw conveyor.

The required heat transfer surface of the Rotating Drum Heat Exchanger depends mainly on the temperature difference between the melting point of the PCM and the saturation temperature of the evaporating water. Table 6 and Table 7 show the values of the achievable surface-specific heat transfer for a drum at the reference case defined in Section 2.7 for different saturation pressures when using $NaNO_3$ and $NaNO_3/KNO_3$ as storage material. The required size of the heat transfer surface for the generation of the defined 20 000 kg·h^{-1} of process steam is given in Table 8 for $NaNO_3$ as PCM and in Table 9 for the eutectic

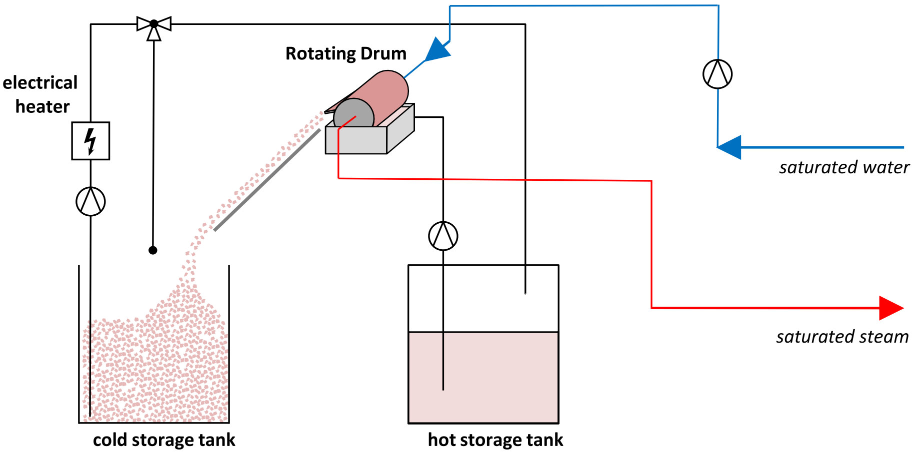

Fig. 16. Thermal energy storage system based on the Rotating Drum Heat Exchanger for the generation of process steam.

Table 6
Surface–specific heat transfer potential using $NaNO_3$ as PCM at different saturation pressures and rotational speeds.

		Saturation Pressure / Temperature			
		2.5 bar / 127.4 °C	8 bar / 170 °C	20 bar / 212 °C	75 bar / 291 °C
Rotational Speed [min^{-1}]	12.5	118.2 $kW{\cdot}m^{-2}$	92.5 $kW{\cdot}m^{-2}$	69.6 $kW{\cdot}m^{-2}$	23.5 $kW{\cdot}m^{-2}$
	25	166.9 $kW{\cdot}m^{-2}$	134.3 $kW{\cdot}m^{-2}$	103.7 $kW{\cdot}m^{-2}$	29.6 $kW{\cdot}m^{-2}$
	50	233.4 $kW{\cdot}m^{-2}$	189.7 $kW{\cdot}m^{-2}$	146.6 $kW{\cdot}m^{-2}$	31.6 $kW{\cdot}m^{-2}$
	100	288.3 $kW{\cdot}m^{-2}$	233.7 $kW{\cdot}m^{-2}$	179.6 $kW{\cdot}m^{-2}$	33.0 $kW{\cdot}m^{-2}$
	200	338.4 $kW{\cdot}m^{-2}$	272.3 $kW{\cdot}m^{-2}$	206.0 $kW{\cdot}m^{-2}$	33.0 $kW{\cdot}m^{-2}$
	400	380.6 $kW{\cdot}m^{-2}$	302.5 $kW{\cdot}m^{-2}$	222.2 $kW{\cdot}m^{-2}$	33.2 $kW{\cdot}m^{-2}$

Table 7
Surface–specific heat transfer potential using $NaNO_3/KNO_3$ as PCM at different saturation pressures and rotational speeds.

		Saturation Pressure / Temperature			
		2.5 bar / 127.4 °C	8 bar / 170 °C	20 bar / 212 °C	75 bar / 291 °C
Rotational Speed [min^{-1}]	12.5	55.8 $kW{\cdot}m^{-2}$	36.4 $kW{\cdot}m^{-2}$	9.9 $kW{\cdot}m^{-2}$	–
	25	83.6 $kW{\cdot}m^{-2}$	57.4 $kW{\cdot}m^{-2}$	10.7 $kW{\cdot}m^{-2}$	–
	50	112.7 $kW{\cdot}m^{-2}$	75.8 $kW{\cdot}m^{-2}$	11.1 $kW{\cdot}m^{-2}$	–
	100	142.7 $kW{\cdot}m^{-2}$	93.1 $kW{\cdot}m^{-2}$	11.1 $kW{\cdot}m^{-2}$	–
	200	170.0 $kW{\cdot}m^{-2}$	97.8 $kW{\cdot}m^{-2}$	11.2 $kW{\cdot}m^{-2}$	–
	400	193.3 $kW{\cdot}m^{-2}$	98.2 $kW{\cdot}m^{-2}$	11.2 $kW{\cdot}m^{-2}$	–

mixture of $NaNO_3/KNO_3$ as PCM. As an example, a required size of 50 m^2 can be met by two parallel drums with a diameter of 2 m and a length of 4 m each. 75 m^2 can be achieved if the length of the drums is increased to 6 m, resulting in a required base area of 24 m^2 for the heat exchanger. To supply of high-pressure steam at 75 bar using $NaNO_3$ as PCM, a heat exchanger surface of about 250 m^2 is required. This can be met, for example, by three drums with a diameter of 3 m and a length of 9 m each, resulting in a base area of 81 m^2.

Table 8
Required heat transfer surface for the generation of 20 000 $kg{\cdot}h^{-1}$ of steam at different saturation pressures and rotational speeds using $NaNO_3$ as PCM.

		Saturation Pressure / Temperature			
		2.5 bar / 127.4 °C	8 bar / 170 °C	20 bar / 212 °C	75 bar / 291 °C
Rotational Speed [min^{-1}]	12.5	102.5 m^2	123.0 m^2	150.8 m^2	348.3 m^2
	25	72.6 m^2	84.7 m^2	101.2 m^2	276.5 m^2
	50	51.9 m^2	60.0 m^2	71.6 m^2	259.0 m^2
	100	42.0 m^2	48.7 m^2	58.5 m^2	248.0 m^2
	200	35.8 m^2	41.8 m^2	51.0 m^2	248.0 m^2
	400	31.8 m^2	37.6 m^2	47.2 m^2	246.5 m^2

Table 9
Required heat transfer surface for the generation of 20 000 $kg{\cdot}h^{-1}$ of steam at different saturation pressures and rotational speeds using $NaNO_3/KNO_3$ as PCM.

		Saturation Pressure / Temperature			
		2.5 bar / 127.4 °C	8 bar / 170 °C	20 bar / 212 °C	75 bar / 291 °C
Rotational Speed [min^{-1}]	12.5	221.1 m^2	312.5 m^2	1060.5 m^2	–
	25	144.9 m^2	198.2 m^2	981.2 m^2	–
	50	107.5 m^2	150.1 m^2	945.8 m^2	–
	100	84.9 m^2	122.2 m^2	945.8 m^2	–
	200	71.3 m^2	116.3 m^2	937.4 m^2	–
	400	62.7 m^2	115.8 m^2	937.4 m^2	–

3.2. Cogeneration of process steam and electricity from stored renewable energy

While the Rotating Drum Heat Exchanger is predestined for the generation of saturated steam, an additional heat exchanger can be integrated for the generation of superheated steam. This possibility arises from the total separation of the liquid and solid storage material. By expanding the superheated steam in a steam turbine up to the saturation temperature, mechanical energy can be generated additionally to the required process steam. By converting the mechanical energy into electricity by using an electrical generator, the thermal energy stored within the thermal energy storage system can be used for the demand-based cogeneration of steam and electricity. The main process design is shown in Fig. 17. Liquid water at its saturation temperature is evaporated within the Rotating Drum and afterwards superheated in the additional heat exchanger, which is fed by the liquid PCM from the hot storage tank. The temperature of the hot PCM is decreased in the heat exchanger, while a temperature well above the solidification temperature has to be ensured. Since process steam at a pressure well above the

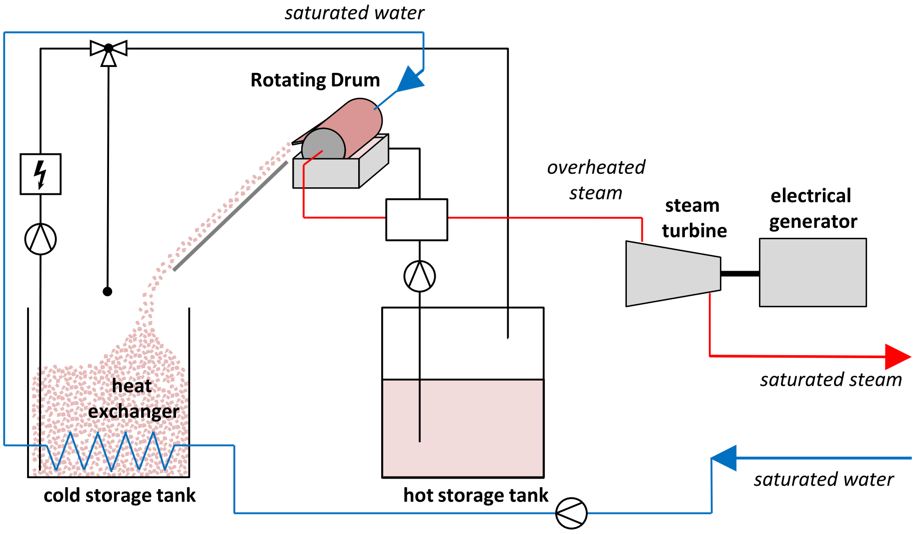

Fig. 17. Thermal energy storage system for the cogeneration of process steam and electricity.

Table 10
Maximum percentage of electricity output and turbine inlet temperature for the cogeneration of electricity at different process steam pressure levels.

		high pressure					
		75 bar		**20 bar**		**8 bar**	
		max. turbine inlet temperature	electricity output	max. turbine inlet temperature	electricity output	max. turbine inlet temperature	electricity output
low pressure	**20 bar**	364 °C	11.6 %	–	–	–	–
	8 bar	421 °C	17.6 %	260 °C	7.3 %	–	–
	2.5 bar	497 °C	23.8 %	330 °C	14.7 %	232 °C	8 %

atmospheric pressure is required as process steam, a backpressure steam turbine is assumed for the expansion of the superheated steam. Assuming an isentropic efficiency of the turbine of $\eta_s = 0.85$ and an ideal electric generator with an efficiency of $\eta_{el.gen.} = 1$, the gainable percentage of electricity output for different pressure levels is shown in Table 10. The figure therefore shows, how much parts of the stored thermal energy are transferable into electricity for the given inlet and outlet temperatures and pressures of the steam. The remaining parts of stored thermal energy are used for the generation of process steam. The specified maximum steam temperature at the steam turbine inlet results from the definition of reaching saturated steam at the turbines outlet. Increasing the temperature would result in superheated steam at the turbines outlet. While a share of electricity output of up to 24 % can be achieved at a steam turbine inlet pressure of 75 bar and a saturated steam pressure of 2.5 bar required for the process steam, the share of electricity output is reduced at lower inlet pressures at the turbine or higher required steam pressures for the process steam. This results from the lower difference in the specific enthalpy of the steam, which can be

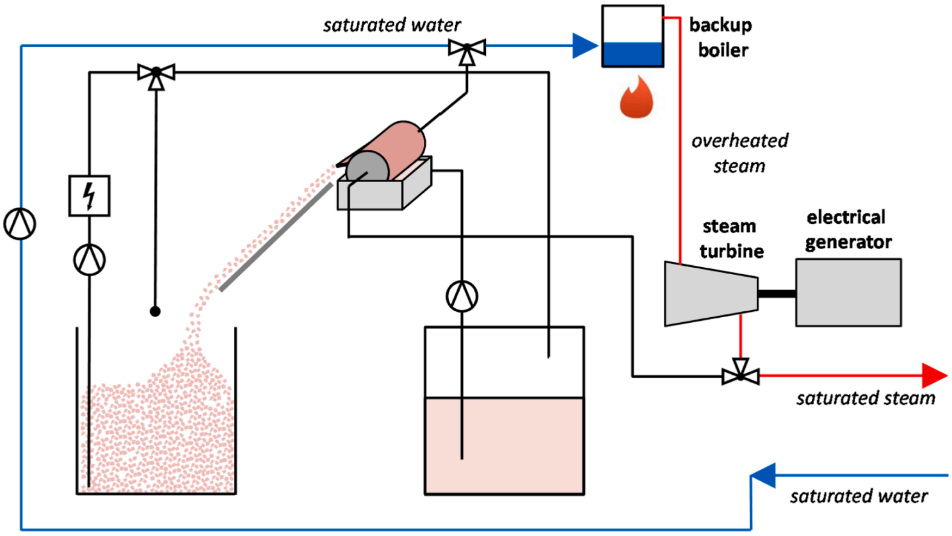

Fig. 18. Basic setting of a cogenerating backup boiler.

converted into electricity in this case. The storage density of the system can be further increased by installing a heat exchanger inside the cold storage tank to preheat the feed water into the Rotating Drum. For this purpose, the returning liquid water from the steam process, which is assumed to be saturated liquid, is heated up in the cold storage tank after a pump increased the pressure again.

3.3. Cogenerating backup boiler

The state-of-the-art for large-scale process steam generation is a cogeneration plant with a fossil burner and a steam turbine for the cogeneration of electricity and process steam, as shown in Fig. 18. While a backup boiler is also useful for meeting 100 % process steam availability (compare the introduction of Section 3), the thermal energy storage system introduced can decouple the electrical power and process steam supply of state-of-the-art cogeneration plants without direct efficiency losses. In times when the electricity demand is low or fluctuating renewable energies are available, the power of the burner and thus the power of the steam turbine can be reduced or shut off and the storage system guarantees a stable process steam supply. When the electricity demand is high or no fluctuating renewable energies are available, the power of the burner and the turbine can be increased. In this case, the additional thermal energy not directly required can be stored within the heat storage system. The cold storage tank thus serves as the heat sink of the Rankine cycle. This can be done either by directly implementing a heat exchanger within the cold storage tank or by using a separate heat exchanger, which is located between the cold and hot storage tank in a similar way to the electrical heater. By doing so, no excess heat has to be removed from the system and the overall efficiency is 100 %, assuming an ideal thermal insulation. Fig. 19 shows an example of a combined process steam supply system using the eutectic mixture of $NaNO_3$ and KNO_3 as storage material. Assuming a backup-boiler supplies superheated steam at a pressure of 180 bar and a temperature of 550 °C, which is expanded in an assumed backpressure steam turbine with an isentropic efficiency of 85 % to the required process steam at a pressure of 8 bar and saturation temperature. In this case, the electricity output can be increased by 65 % when the power of the backup-boiler is doubled. The excess steam supplied by the backup-boiler is extracted from the turbine at a pressure of 30 bar and a temperature of 300 °C and condensed in the cold storage tank. The amount of heat charged into the storage system is almost equal to the energy supplied to the industrial process in the form of process steam.

3.4. Integration of high temperature heat pumps

In case of an available low-temperature heat source, which can be either the ambient air, a water reservoir or waste heat, the separation of the cold and hot storage material allows the integration of a heat pump in a unique and efficient way. While the coefficient of performance (COP) of a heat pump is directly affected by the temperature difference between the heat source and the heat output, an essential part of the thermal energy can be charged at the constant temperature of the phase change of the storage material or below this temperature. In the case of $NaNO_3$ used as storage material, 38 % of the energy storable within the total possible temperature range between 200 °C and 560 °C can be charged at a temperature slightly above its melting point of 306 °C. In case of a eutectic mixture of $KNO_3 – NaNO_3$, operated in the same total temperature range, 21 % can be charged at a constant temperature of slightly above its melting point of 222 °C (compare Section 3.5). The thermal energy delivered by the heat pump can either be integrated directly into the cold storage tank by an internal heat exchanger or by an external heat exchanger arranged similar to the introduced electrical heater. The remaining thermal energy for charging the storage up to 560 °C can be provided by an ordinary resistance heater.

3.5. Storage density and size of the storage tanks

The proposed storage material consists of the same components as Solar Salt, which is commonly used in state-of-the-art molten salt thermal energy storage systems, mainly used in CSP-Plants. Compared to the state-of-the-art, the storage density of the material can be significantly increased by utilizing the phase change enthalpy as well as the thermal energy that can be stored by changing the temperature of the storage material. As a reference for the storage density of state-of-the-art molten salt storage systems, the storage density of Solar Salt within the typical temperature range between 290 °C and 560 °C is used. For the specific heat capacity and density of Solar Salt, the correlations given in [51] are used. While the minimum density is 1730 $kg·m^{-3}$ at a temperature of 560 °C, the heat capacity in the mentioned temperature range is 419 $kJ·kg^{-1}$. The volumetric heat storage capacity is thus 201 $kWh·m^{-3}$, a value which is also given for the volumetric storage density of state-of-the-art molten salt thermal energy storage systems in the work of Bauer et al. [2].

When using $NaNO_3$ as storage material in the overall temperature range from 200 °C in the solid state up to 560 °C in the liquid state, the heat capacity increases as mentioned. The solid-liquid phase change enthalpy is 178 $kJ·kg^{-1}$ [23]. The specific heat capacity of the liquid

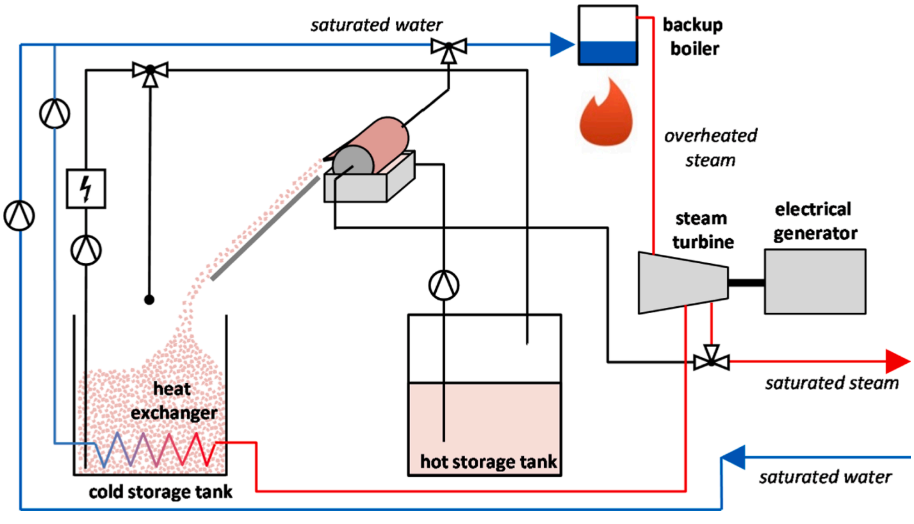

Fig. 19. Extended backup boiler with the integration of excess heat into the storage system.

phase is almost constant in the whole temperature range from 306 °C to 560 °C and amounts to 1.67 kJ·kg^{-1}·K^{-1} [23,52,53], resulting in a specific heat storage capacity of 424 kJ·kg^{-1}. When the temperature of the solidified $NaNO_3$ is further reduced , there is a solid-solid transition at a temperature of 276 °C [52–54]. The values of the heat of transition of the solid-solid transition ranges between 43 kJ·kg^{-1} and 52 kJ·kg^{-1} in the three references given above, while the average value is 47 kJ·kg^{-1}. Due to the proximity of the point of transition to the melting point, it is difficult to determine a certain value for the specific heat capacity in the temperature region between 220 °C and 306 °C. For the heat capacity in the temperature range from 200 °C to 220 °C, the polynomial equation given in [53] is used, resulting in a storable heat of 33 kJ·kg^{-1}. Further research is required to accurately quantify the storable heat in the temperature range of the solid-solid transition. Adding the solid-liquid phase change enthalpy, the enthalpy of the solid-solid transition and the heat capacity of the liquid and solid phase, at least 682 kJ·kg^{-1} can be stored within $NaNO_3$ in the temperature limit mentioned above. The minimum density at 560 °C can be determined by linear extrapolation with the values collected in [23] to 1750 kg·m^{-3}, resulting in a volumetric heat storage capacity of 332 kWh·m^{-3}. For the eutectic mixture of $NaNO_3$ and KNO_3, a constant specific heat capacity of 1.492 kJ·kg^{-1}·K^{-1} is reported for the liquid phase between the melting temperature of 222 °C and 560 °C, resulting in a heat storage capacity of 504 kJ·kg^{-1}. The phase change enthalpy amounts to 107 kJ·kg^{-1} [28]. For the heat capacity of the solid phase, the values shown in the figure in [30] are linearized, resulting in a linear decrease of the specific heat capacity of 1.38 kJ·kg^{-1}·K^{-1} at 222 °C and 1.35 kJ·kg^{-1}·K^{-1} at 200 °C. This results in an additional heat capacity of 30 kJ·kg^{-1} within the temperature range from 200 °C to 222 °C. The sum of the three heat capacities amounts to a total heat storage capacity of 641 kJ·kg^{-1}. The minimum density at 560 °C can be found by linear extrapolation of the values for ambient air given in [30] to 1730 kg·m^{-3}, resulting in a volumetric heat storage capacity of 308 kWh·m^{-3}.

In summary, compared to two-tanks molten salt storages, the volumetric storage density of the storage system presented in this paper can be increased by 65 % when $NaNO_3$ is used as storage material and by 53 % when the eutectic mixture of $NaNO_3$ and KNO_3 is used as storage material. While an increased storage density reduces the amount of storage material required, also the size of the storage tanks can be reduced, resulting in additional cost savings. For the proposed storage of 360 MWh (15 MW for 24 h), in case of $NaNO_3$ as storage material, two tanks with 1084 m^3 are required, which is equivalent to cylindrical tanks with a diameter of 12 m and a height of 10 m each. The selection of pure $NaNO_3$ or the eutectic mixture of $NaNO_3$ and KNO_3 as storage material is mainly based on the main industrial use of the storage system based on the different melting points of the two materials.

4. Conclusion

This paper presents the potential of a thermal energy storage system using the Rotating Drum Heat Exchanger as the key component for the generation of process steam for industrial application.

Compared to state-of-the-art passive latent heat thermal energy storages, the solid storage material can be stored separately from the liquid storage material when using the Rotating Drum Heat Exchanger. The thermal power is therefore completely independent of the storage capacity of the thermal energy storage system. This results in the possibility of choosing the size of the storage tanks, and thus the storage capacity of the thermal energy storage system, independently of the size of the heat transfer surface and thus the thermal power of the storage system. This might lead to cost savings particularly in case of large required storage capacities in storage systems with a storage duration of 10 h – 100 h.

Since the required wall thickness for a given internal pressure increases with the diameter of a hollow drum, a hollow drum cannot be designed freely in its diameter. In order achieve a freely scalable design, the so-called multiple-channel drum is introduced within this research. A previously introduced simulation is adopted for the calculation of the multiple-channel drum and used to identify the influence of different design parameters on the resulting heat transfer. It can be concluded, that only the mean thickness of the heat exchanger wall, commonly made out of steel, has a major effect on the heat transfer of the heat exchanger. As an example, doubling the average heat transferring wall thickness from 6 mm to 12 mm reduces the heat transfer by 31 % on average. The steel wall therefore becomes the dominating part of the heat transfer resistances, while the evaporation inside the drum and the solidification at the outer side of the drum are comparable effective. The required wall thickness to withstand the internal pressure is in the range of a few millimeters and thus not limiting the heat transfer. The minimum feasible wall thickness depends mainly on manufacturing aspects, which limits have to be identified in further research. Further design parameters, as the length of the drum, the diameter of the channels in the drum shell, the immersion depth of the Rotating Drum in liquid PCM but also the total diameter of the drum has only a minor affect on the heat transfer. Its effect on the heat transfer in general well below 10 % in case of doubling or halving these parameters. The Rotating Drum Heat Exchanger is therefore freely scalable which predestines the design for the industrial usage.

The concept of the Rotating Drum Heat Exchanger allows the transfer of the phase change enthalpy released during the phase change of the storage material from the liquid to the solid state, in addition to the thermal energy that can be stored by changing the temperature of the solid and liquid storage material. As a result, the volumetric storage density of the storage material used can be significantly increased to up to 332 kWh·m^{-3} when using $NaNO_3$ as storage material, which is an increase of up to 65 % compared to state-of-the-art two-tank molten salt storages. For the industrial application of such a thermal energy storage system a reduction of the required storage material and the size of the storage tanks – both results in cost-advantages compared to the state-of-the-art can be concluded.

For the generation of process steam, a reference drum with a diameter of 1 m has been defined. The achievable surface-specific heat transfer exceeds 300 kW·m^{-2} for the generation of saturated steam at 2.5 bar, 250 kW·m^{-2} at 8 bar, 200 kW·m^{-2} at 20 bar and 30 kW·m^{-2} at 75 bar when using $NaNO_3$ with a melting point of 306 °C as heat storage material. Using the eutectic mixture of $NaNO_3$ and KNO_3 with a melting point of 222 °C, the achievable surface-specific heat transfer exceeds 150 kW·m^{-2} at 2.5 bar, 90 kW·m^{-2} at 8 bar and 10 kW·m^{-2} at 20 bar. The unique separation of the solid PCM from the liquid PCM allows the integration of a cross-flow heat exchanger for the generation of superheated steam, which can be used either directly for industrial processes or for the co-generation of saturated steam and electricity. When combining the thermal energy storage system with a conventional fossil or regenerative burner for the co-generation of electricity and steam, the amount of electricity supplied can be decoupled from the amount of steam supplied. When no electricity is needed, the storage system provides the required steam. In case of large demand of electricity, the power of the burner and thus the generation of electricity can be increased, while the excess heat of the cycle can be used to charge the storage system. It can be concluded, that the proposed thermal energy storage system is therefore predestined for the (co-) generation of process steam. If the large-scale implementation succeeds accordingly, the presented storage system for thermal energy can contribute a decisive advantage to the decarbonization and flexibilization of process steam supply.

In a next step, the authors are planning a high-temperature test rig to generate saturated steam from thermal energy stored within a nitrate salt.

Funding

This research did not receive any specific grant from funding

agencies in the public, commercial, or not-for-profit sectors.

CRediT authorship contribution statement

Jonas Tombrink: Conceptualization, Methodology, Investigation, Validation, Visualization, Writing – original draft. **Dan Bauer:** Conceptualization, Funding acquisition, Supervision, Writing – review & editing.

Declaration of Competing Interest

The authors declare that they have no known competing financial interests or personal relationships that could have appeared to influence the work reported in this paper.

References

[1] Naegler T, Simon S, Klein M, Gils HC. Quantification of the European industrial heat demand by branch and temperature level. Int J Energ Res 2015;39:2019–30. https://doi.org/10.1002/er.3436.

[2] Bauer T, Odenthal C, Bonk A. Molten Salt Storage for Power Generation. Chem Ing Tech 2021;93:534–46. https://doi.org/10.1002/cite.202000137.

[3] Patel NS, Pavlík V, Boča M. High-Temperature Corrosion Behavior of Superalloys in Molten Salts – A Review. Crit Rev Solid State Mater Sci 2016;42:83–97. https://doi.org/10.1080/10408436.2016.1243090.

[4] Sötz VA, Bonk A, Bauer T. With a view to elevated operating temperatures in thermal energy storage - Reaction chemistry of solar salt up to 630°C. Sol Energy Mater Sol Cells 2020;212:110577. https://doi.org/10.1016/j.solmat.2020.110577.

[5] Kenisarin MM. High-temperature phase change materials for thermal energy storage. Renew Sust Energ Rev 2010;14:955–70. https://doi.org/10.1016/j.rser.2009.11.011.

[6] Tao YB, He Y-L. A review of phase change material and performance enhancement method for latent heat storage system. 93 (2018) 245-259 https://doi.org/10.1016/j.rser.2018.05.028.

[7] Lin Y, Jia Y, Alva G, Fang G. Review on thermal conductivity enhancement, thermal properties and applications of phase change materials in thermal energy storage. Renew Sust Energ Rev 2018;82:2730–42. https://doi.org/10.1016/j.rser.2017.10.002.

[8] Tombrink J, Jockenhöfer H, Bauer D. Examination of the heat transfer potential of an active latent heat storage concept, Eurotherm Seminar n°112 - Advances in Thermal Energy Storage; Lleida, Spain (2019).

[9] Tombrink J, Jockenhöfer H, Bauer D. Experimental investigation of a rotating drum heat exchanger for latent heat storage. Appl Therm Eng 2021;183:116221. https://doi.org/10.1016/j.applthermaleng.2020.116221.

[10] Tombrink J, Bauer D. Simulation of a rotating drum heat exchanger for latent heat storage using a quasistationary analytical approach and a numerical transient finite difference scheme. Appl Therm Eng 2021;194:117029. https://doi.org/10.1016/j.applthermaleng.2021.117029.

[11] Kost C, Shammugam S, Fluri V, Peper D, Memar AD, Schlegl T. Levelized cost of electricity renewable energy technologies. Fraunhofer Institute for Solar Energy Systems; 2021.

[12] E.-E. AISBL, ENTSO-E Transparency Platform, https://transparency.entsoe.eu/, Last Access: 19.08.2021.

[13] Borst F, Strobel N, Kohne T, Weigold M. Investigating the electrical demand-side management potential of industrial steam supply systems using dynamic simulation. Energies 2021;14(6):1533. https://doi.org/10.3390/en14061533.

[14] Beck A, Sevault A, Drexler-Schmid G, Schöny M, Kauko H. Optimal selection of thermal energy storage technology for fossil-free steam production in the processing industry. Appl Sci 2021;11(3):1063. https://doi.org/10.3390/app11031063.

[15] Gel'perin NI, Nosov GA, Makotkin AV. Determinating the thickness of liquid film holdup on a rotating drum surface. Chem Pet Eng 1975;11:230–3. https://doi.org/10.1007/BF01146631.

[16] Tsou FK, Sparrow EM, Goldstein RJ. Flow and heat transfer in the boundary layer on a continuous moving surface. Int J Heat Mass Transf 1967;10:219–35. https://doi.org/10.1016/0017-9310(67)90100-7.

[17] Gorenflo D, Kenning D. H_2 pool boiling. In: VDI, editor. VDI heat atlas. Berlin, Heidelberg: Springer; 2009. https://doi.org/10.1007/978-3-540-77877-6_45.

[18] Baehr HD, Stephan K. Heat and mass transfer. Berlin, Heidelberg: Springer; 2011. https://doi.org/10.1007/978-3-642-20021-2.

[19] Kind M, Steiner D, Chawla JM, Schröder J-J, Saito Y, Auracher H, et al. H_3 flow boiling. In: VDI, editor. VDI Heat Atlas. Berlin, Heidelberg: Springer; 2010. https://doi.org/10.1007/978-3-540-77877-6_124.

[20] Wei G, Wang G, Xu C, Ju X, Xing L, Du X, et al. Selection principles and thermophysical properties of high temperature phase change materials for thermal energy storage: A review. Renew Sust Energ Rev 2018;81:1771–86. https://doi.org/10.1016/j.rser.2017.05.271.

[21] Lin Y, Alva G, Fang G. Review on thermal performances and applications of thermal energy storage systems with inorganic phase change materials. Energy 2018;165:685–708. https://doi.org/10.1016/j.energy.2018.09.128.

[22] Mohamed SA, Al-Sulaiman FA, Ibrahim NI, Zahir MH, Al-Ahmed A, Saidur R, et al. A review on current status and challenges of inorganic phase change materials for thermal energy storage systems. Renew Sust Energ Rev 2017;70:1072–89. https://doi.org/10.1016/j.rser.2016.12.012.

[23] Bauer T, Laing D, Tamme R. Characterization of Sodium Nitrate as Phase Change Material. Int J Thermophys 2012;33:91–104. https://doi.org/10.1007/s10765-011-1113-9.

[24] Nagasaka Y, Nagashima A. The thermal conductivity of molten $NaNO_3$ and KNO_3. Int J Thermophys 1991;12:769–81. https://doi.org/10.1007/BF00502404.

[25] Schinke H, Sauerwald F. Dichtemessungen Über die Volumenänderung beim Schmelzen und den Schmelzprozeß bei anorganischen Salzen. J. Inorg. Gen. Chem. 1960;304:25–36. https://doi.org/10.1002/zaac.19603040104.

[26] Nunes VMB, Lourenço MJV, Santos FJV, de Castro CAN. Viscosity of Molten Sodium Nitrate. Int J Thermophys 2006;27:1638–49. https://doi.org/10.1007/s10765-006-0119-1.

[27] Dahl JL, Duke FR. Surface Tensions of the $AgNO_3$–$NaNO_3$ and $AgNO_3$–KNO_3Systems, The. J Phys Chem 1958;62:1142–3. https://doi.org/10.1021/j150567a034.

[28] Bauer T, Laing D, Tamme R. Overview of PCMs for Concentrated Solar Power in the Temperature Range 200 to 350°C. AST 2010;74:272–7. https://doi.org/10.4028/www.scientific.net/AST.74.272.

[29] Janz GJ, Krebs U, Siegenthaler HF, Tomkins RPT. Molten Salts: Volume 3 Nitrates, Nitrites, and Mixtures: Electrical Conductance, Density, Viscosity, and Surface Tension Data. J Phys Chem Ref Data 1972;1:581–746. https://doi.org/10.1063/1.3253103.

[30] Carling RW, Kramer CM, Bradshaw RW, Nissen DA, Goods SH, Mar RW, et al. Molten nitrate salt technology development status report SAND80- 8052, Sandia Laboratory; 1981.

[31] Rodríguez-García M-M, Herrador-Moreno M, Zarza Moya E. Lessons learnt during the design, construction and start-up phase of a molten salt testing facility. Appl Therm Eng 2014;62:520–8. https://doi.org/10.1016/j.applthermaleng.2013.09.040.

[32] Steinmann WD, Laing D, Tamme R. Latent Heat Storage Systems for Solar Thermal Power Plants and Process Heat Applications. J Sol Energ -T Asme 2010;132. https://doi.org/10.1115/1.4001405.

[33] Tamme R, Bauer T, Buschle J, Laing D, Müller-Steinhagen H, Steinmann W-D. Latent heat storage above 120°C for applications in the industrial process heat sector and solar power generation. Int J Energy Res 2008;32:264–71. https://doi.org/10.1002/er.1346.

[34] Bell S, Steinberg T, Will G. Corrosion mechanisms in molten salt thermal energy storage for concentrating solar power. Renew Sust Energ Rev 2019;114:109328. https://doi.org/10.1016/j.rser.2019.109328.

[35] Trent MC, Goods SH, Bradshaw RW. Comparison of Corrosion Performance of Grade 316 and Grade 347H Stainless Steels in Molten Nitrate Salt. Aip Conf Proc 2016;1734. https://doi.org/10.1063/1.4949258.

[36] Goods S, Bradshaw R, Prairie M, Chavez J. Corrosion of stainless and carbon steels in molten mixtures of industrial nitrates. Sandia National Lab. 1994. https://doi.org/10.2172/10141843.

[37] Kruizenga AM, Gill DD, LaFord ME. Corrosion of high temperature alloys in solar salt at 400, 500, and 680 °C. Sandia National Lab. SAND2013-8256 2013. https://doi.org/10.2172/1104752.

[38] Bonk A, Rückle D, Kaesche S, Braun M, Bauer T. Impact of Solar Salt aging on corrosion of martensitic and austenitic steel for concentrating solar power plants. Sol Energy Mater Sol Cells 2019;203:110162. https://doi.org/10.1016/j.solmat.2019.110162.

[39] Soleimani Dorcheh A, Durham RN, Galetz MC. Corrosion behavior of stainless and low-chromium steels and IN625 in molten nitrate salts at 600 °C. Sol Energy Mater Sol Cells 2016;144:109–16. https://doi.org/10.1016/j.solmat.2015.08.011.

[40] Chu TK, Ho CY. Thermal conductivity and electrical resistivity of eight selected AISI stainless steels. In: Mirkovich VV, editor. Thermal conductivity 15. Boston, MA: Springer; 1978. https://doi.org/10.1007/978-1-4615-9083-5_12.

[41] Perovic NL, Maglic KD, Stanimirovic AM, Vukovic GS. Transport and calorimetric properties of AISI 321 by pulse thermal diffusivity and calorimetric techniques. High Temp - High Pressures 1995;27:53–8.

[42] E.C.f. Standardization, Stainless steels - Part 3. Technical delivery conditions for semi-finished products, bars, rods and sections for general purposes, EN 10088-3, (2014).

[43] Ensinas AV, Nebra SA, Lozano MA, Serra LM. Analysis of process steam demand reduction and electricity generation in sugar and ethanol production from sugarcane. Energy Convers Manag 2007;48:2978–87. https://doi.org/10.1016/j.enconman.2007.06.038.

[44] Ravi Kumar K, Krishna Chaitanya NVV, Sendhil Kumar N. Solar thermal energy technologies and its applications for process heating and power generation – A review. J Clean Prod 2021;282:125296. https://doi.org/10.1016/j.jclepro.2020.125296.

[45] Gambini M, Vellini M, Stilo T, Manno M, Bellocchi S. High-efficiency cogeneration systems: The case of the paper industry in Italy. Energies 2019;12(3):335. https://doi.org/10.3390/en12030335.

[46] Shabbir I, Mirzaeian M. Feasibility analysis of different cogeneration systems for a paper mill to improve its energy efficiency. Int J Hydrog Energy 2016;41:16535–48. https://doi.org/10.1016/j.ijhydene.2016.05.215.

[47] Wang L, Yu S, Kong F, Sun X, Zhou Y, Zhong W, et al. A study on energy storage characteristics of industrial steam heating system based on dynamic modeling. Energy Rep 2020;6:190–8. https://doi.org/10.1016/j.egyr.2020.07.001.

[48] Einstein D, Worrell E, Khrushch M. Steam systems in industry: Energy use and energy efficiency improvement potentials. In: 2001 ACEEE Summer Study on Energy Efficiency in Industry; Tarrytown, NY, USA; 2001.

[49] Solomon AA, Child M, Caldera U, Breyer C. How much energy storage is needed to incorporate very large intermittent renewables? Energy Procedia 2017;135: 283–93. https://doi.org/10.1016/j.egypro.2017.09.520.

[50] Ziegler MS, Mueller JM, Pereira GD, Song J, Ferrara M, Chiang Y-M, et al. Storage Requirements and Costs of Shaping Renewable Energy Toward Grid Decarbonization. Joule 2019;3:2134–53. https://doi.org/10.1016/j.joule.2019.06.012.

[51] Bauer T, Pfleger N, Breidenbach N, Eck M, Laing D, Kaesche S. Material aspects of Solar Salt for sensible heat storage. Appl Energy 2013;111:1114–9. https://doi.org/10.1016/j.apenergy.2013.04.072.

[52] Carling RW. Heat capacities of $NaNO_3$ and KNO_3 from 350 to 800 K. Thermochim Acta 1983;60:265–75. https://doi.org/10.1016/0040-6031(83)80248-2.

[53] Takahashi Y, Sakamoto R, Kamimoto M. Heat capacities and latent heats of $LiNO_3$, $NaNO_3$, and KNO_3. Int J Thermophys 1988;9:1081–90. https://doi.org/10.1007/bf01133275.

[54] Jriri T, Rogez J, Bergman C, Mathieu JC. Thermodynamic study of the condensed phases of NaNO3, KNO3 and CsNO3 and their transitions. Thermochim Acta 1995; 266:147–61. https://doi.org/10.1016/0040-6031(95)02337-2.

4 Discussion

The publications on which this thesis is based are directly connected to each other. Starting from an experimental investigation in the first publication, a suitable numerical simulation for the heat transfer of a Rotating Drum Heat Exchanger is developed in the second publication. In the third publication, the design of the Rotating Drum Heat Exchanger is adapted to obtain a freely scalable high-temperature thermal energy storage system. Therefore, the numerical simulation is partially modified in the third publication. In this section, the scientific contribution of the three papers and thus of the whole dissertation as a whole is discussed.

With the experimental test rig, which is presented in detail in the first publication, a heat transfer of above 1.5 kW has been achieved during the solidification of a phase change material. A drum with a diameter of 0.184 m and a length of 0.4 m was used, resulting in a total heat-transferring drum shell surface of 0.23 m^2. This results in a maximum demonstrated surface specific heat transfer density of 6.5 kW·m^{-2}, while only 24 % of the drum surface was immersed in the liquid PCM. In contrast to other heat exchange technologies that do not involve a phase change of the heat transferring material, the total temperature difference between the liquid PCM and the fluid inside the drum $\Delta T_{\mathrm{HTF\text{-}PCM,l}}$ has to be devided into two parts: The temperature difference between the HTF in the drum and the melting point of the PCM $\Delta T_{\mathrm{HTF\text{-}PCM,m}}$ and the temperature difference between the melting point of the PCM and the temperature of the liquid PCM $\Delta T_{\mathrm{PCM,m\text{-}PCM,l}}$. Thereby, an increase in $\Delta T_{\mathrm{HTF\text{-}PCM,m}}$ has a significantly larger effect on the heat transfer than an increase in $\Delta T_{\mathrm{PCM,m\text{-}PCM,l}}$. For instance, for a total temperature difference $\Delta T_{\mathrm{HTF\text{-}PCM,l}}$ of 20 K, the heat transfer is increased by 31 % on average if $\Delta T_{\mathrm{HTF\text{-}PCM,m}}$ is increased by 5 K and $\Delta T_{\mathrm{PCM,m\text{-}PCM,l}}$ is decreased by 5 K at the same time. Compared to a purely convective heat transfer without solidification at a total temperature difference $\Delta T_{\mathrm{HTF\text{-}PCM,l}}$ of 20 K, the heat transfer is increased by 77 % when solidification occurs at the same total temperature difference $\Delta T_{\mathrm{HTF\text{-}PCM,l}}$. In this case, the total temperature difference is divided into 10 K each, the temperature difference between the HTF and the melting temperature of the PCM $\Delta T_{HTF\text{-}PCM,m}$ and the melting temperature of the PCM and the temperature of the liquid PCM $\Delta T_{PCM,m\text{-}PCM,l}$. Referring the maximum measured surface-specific heat transfer of 6.5 $kW{\cdot}m^{-2}$ to a temperature difference of 20 K, a maximum overall heat transfer coefficient of the experimental test rig of 325 $W{\cdot}m^{-2}{\cdot}K^{-1}$ is obtained. Compared to other heat exchanger technologies listed in [77], this value is in the medium range. Since this value depends on the ratio of the two temperature differences mentioned, higher values can be proposed for an increased temperature difference between the melting point and the temperature of the HTF $\Delta T_{HTF\text{-}PCM,m}$. Also, the specification of a single value of the overall heat tansfer coefficient should be considered as a reference value, since it does not depend linearly on the temperature differences. Moreover, the experimental test rig is not optimized for maximized heat transfer. During all experiments, no evidence of further growth restrictions, meaning limitations of the solidification rate due to any reason other than heat transport processes, could be observed.

Although there was no separation of the solid PCM and the liquid PCM, as the solidified PCM was directly returned to the liquid PCM and re-melted by electrical heaters, there was a constant heat flow for up to several hours. The concept of the Rotating Drum Heat Exchanger is therefore suitable for the reliable transfer of heat released by the liquid - solid phase change of a phase change material.

However, compared to an industrial-scale system described in the third publication, there are some technical simplifications in the experimental test rig. First of all, only liquid water is used as HTF within the drum, while the concept of the Rotating Drum Heat Exchanger is proposed mainly for the evaporation of water. The use of liquid water simplifies the technical complexity of the experimental test rig and allows a more detailed quantification of the heat transfer and the determination of further physical effects. In this context, the temperature difference of the water between the inlet and the outlet of the drum can be almost eliminated by an increased mass flow through the drum. An increased flow velocity through an annular gap inside the drum further increases the surface-specific coefficient of heat transfer inside the drum. This makes the use of liquid water comparable to an evaporating fluid in terms of the heat transfer phenomena. The use of liquid water implies the use of a low temperature PCM with a melting point well below 100 °C. Here, decanoic acid, also referred as capric acid, meet the required specifications. It is proven as PCM in low-temperature applications with a melting point of 31.5 °C, non-toxic and even direct eye contact causes no permanent damage.

These simplifications allow the detailed measurement of the heat transfer and also the investigation of further physical effects related to the heat transfer, which are used to identify models for the simulation of the heat transfer, published in the second publication. So, the experimental setup allows the additional quantification of the thickness of a layer of liquid PCM that adheres to the solidified PCM when the surface emerges from the liquid PCM. This is possible by integrating a rubber lip that can wipe off the adhering liquid shortly after the surface leaves the liquid PCM. By a comparison of the layer thicknesses with adhesion and without adhesion, the adhering layer thicknesses are determined. It is shown that the adhering layer can be calculated by an analytical approach of Gelperin [78] with an average deviation of 39 %. Further investigations are also conducted on the surface coefficient of heat transfer for the moving drum surface in the quiescent liquid PCM. The experimental test rig is also able to measure the heat transfer when no solidification occurs, for convective heat transfer only. It is shown, that the surface coefficient of heat transfer can be estimated by a correlation given by Tsou et al. [79] and Gauler [80]. With this correlation, the numerical simulation presented in the second publication reproduces the transferred heat with an underestimation of 8 % on average.

On the other hand, decanoic acid appears to have a very low hardness compared to the proposed nitrate salts for high temperature storage. While the scraping of decanoic acid works smoothly in the presented test rig, further investigation is necessary for the scraping of nitrate salts. While the mechanical energy required to scrap off the decanoic acid and thus to rotate the drum was found to be in the range of 150 W with the experimental test rig, the values for nitrate salts could be higher. In addition, evaporation of water within the Rotating Drum Heat Exchanger is not possible with the current test rig.

The identified correlations for the surface coefficient of heat transfer and the layer thickness are significant for the development of an overall model of the heat transfer and its calculation, which is described in detail in the second publication. The primary focus is on a reproducible and preferable simple model. Two separate models are discussed in the second publication: a quasistationary model and a one-dimensional transient simulation based on a finite differences scheme. The quasistationary model neglects the thermal capacities of the steel wall and the solidified PCM. In turn, the model is straightforward and easy to calculate, which makes it excellent for rough estimation of the design of the Rotating Drum Heat Exchanger. A mathematical verification of the quasistationary model with an isothermal plane wall with no movement leads to an overestimation of the exact heat transfer of less than 11 %. In contrast, the quasistationary model underestimates the experimental heat transfer by 33 % on average. The main reason for this is the transient effects at the rotating drum surface, as the surface immerses and emerges with each rotation. Therefore, the drums shell is heated up and cooled down with each rotation.

The more detailed one-dimensional transient simulation reproduces the measured heat transfer with an accuracy of 8 % on average. Thereby, a one-dimensional section from the solidification surface towards the HTF is considered. The section is virtually rotated by changing the boundary conditions with the rotational speed and the virtual location of the section. The one-dimensional simulation becomes a two-dimensional simulation due to the time and location dependence of the boundary conditions, while the effectiveness of a one-dimensional simulation remains.

The calculation of the heat transfer with an average accuracy of 8 % validates the numerical simulation for calculating the heat transfer of a Rotating Drum Heat Exchanger for decanoic acid as PCM in the given temperature range. Further research can be conducted to improve the calculation of the layer thicknesses. A sensitivity analyses of the simulation shows a high influence of the material properties of the PCM used on the heat transfer as well as the layer thicknesses. Due to the temperature level close to the melting point of the PCM, the accurate measurement of the material properties is particularly difficult.

The Rotating Drum Heat Exchanger is particularly designed for the use in Carnot-Batteries and for the generation of process steam for industrial applications, as described in Section 1.2. Therefore, the drum needs to be designed to be freely scalable up to the range of several megawatts. The drum needs also be designed to withstand the internal pressure of the steam. According to the Barlaw's formula, the required thickness of the drum shell increases with the internal pressure of the drum and the diameter of the drum. A hollow drum or a drum with an annular gap is therefore not freely scalable and is limited for use at low pressure or low power applications. This is remedied by the so-called multichannel drum, which is presented in the third publication. Here, several small channels are introduced into the drum shell. The overall diameter of the rotating drum is thus decoupled by the Barlaw's formula, resulting in free scalability. The numerical simulation presented in the second paper is adapted for the calculation of the heat transfer at a multiple channel drum, which is presented in the third article.

Using sodium nitrate as PCM with a temperature difference of 178.6 °C between the melting point of the PCM and the saturation temperature of the evaporating water and an additional temperature difference of 44 °C between the melting point of the PCM and the temperature of the liquid PCM, the calculated surface-specific heat transfer exceeds 350 $\mathrm{kW{\cdot}m^{-2}}$. Referring this value to the total temperature difference of 223 °C, an overall heat transfer coefficient of over 1570 $\mathrm{W{\cdot}m^{-2}{\cdot}K^{-1}}$ is obtained, a value well comparable to the heat exchanger technologies with the highest overall heat transfer coefficients discussed in [77]. As identified and also mentioned in the experimental results, the overall heat transfer coefficient is not linear with the temperature difference. Moreover, the temperature difference between the melting point of the PCM and the saturation temperature of the evaporating water clearly dominates the heat transfer compared to the temperature difference between the melting point of the PCM and the temperature of the liquid PCM. Assuming liquid $NaNO_3$ with a temperature of 1 K above the solidification temperature, the overall heat transfer coefficient can be increased to above 2000 $W \cdot m^{-2} \cdot K^{-1}$. Highest values are calculated for small temperature differences between the saturation temperature of the evaporating water and the melting point of the PCM, since the average layer thickness of the solidified PCM is lower at small temperature differences.

A variation of the design parameters shows that the thickness of the heat-transferring steel wall has the largest influence on the heat transfer. The surface coefficient of heat transfer of the evaporating water and also the heat transfer through the solid PCM layer are therefore not limiting for the heat transfer in the concept of the Rotating Drum Heat Exchanger. A reduction of the thickness of the heat transferring steel wall leads to a significant increase of the heat transfer. However, the minimum thickness is limited by manufacturing-specific aspects.

The eutectic mixture of KNO_3 and $NaNO_3$ as well as pure $NaNO_3$ are proposed as storage material for an industrial scale storage system. Since these materials are similar to the so-called Solar Salt used in state-of-the-art industrial-scale molten salt storages, their thermophysical properties, corrosion behavior, and liquid phase temperature limits are well known. With the Rotating Drum Heat Exchanger, the lower temperature limit is extended into the solid phase of the storage material, while the upper temperature limit remains at the same level as in molten salt storages. This results in additional utilization of the phase change enthalpy of the material and the thermal energy that can be stored by changing the temperature of the solid phase of the material. As a result, the storage density of the storage material can be increased by up to 65 % towards 300 $kWh \cdot m^{-3}$ compared to state-of-the-art molten-salt storages. In addition to cost savings due to the lower demand of storage material, the size of the storage tanks can be reduced, resulting in further cost savings.

While the Rotating Drum Heat Exchanger was originally designed for the use in Carnot-Batteries, it is also predestined for the generation of process steam for industrial application. The high surface-specific heat transfer and the increased storage density simplify the local implementation of the storage system in an industrial environment. In this context, an electrical heater is proposed for the charging process. A resistive electrical heater is proposed to charge the thermal energy storage up to a temperature of 560 °C. In case high-temperature heat pumps of industrial size are availability, the use of PCM as storage material allows about one-third of the storable energy to be introduced at a constant temperature slightly above the melting point of the PCM, which is at the lower end of the temperature range of the storage. This increases the COP of the heat pump. The possibility of the co-generation of electricity and process steam combines the generation of process steam with the use as Carnot-Batterie. By generating steam at a pressure and temperature well above the required process steam parameters, the steam can be expanded in a turbine to the required steam parameter. The mechanical energy of the steam turbine can be transformed into electricity by an electrical generator. Depending on the required process steam parameter, up to one quarter of the stored energy can be converted into electricity, while three quarters is used to provide process steam.

In addition to the possibility of complete decarbonization of process steam supply of industrial plants, the technology of the Rotating Drum Heat Exchanger can also be used to decouple the process steam and electricity generation in co-generation plants commonly used today. Thus, the currently used fossil burner can be turned off when fluctuating renewable forms of energy become available. In this case, the thermal energy storage system guarantees the provision of process steam. In times of high electricity demand, the power of the fossil burner can be in increased to increase the electrical output of the co-generating steam turbine. The additional steam not required by the industrial process can be charged to the storage system via a heat exchanger. By doing so, the supply of process steam can be adapted to the availability of renewable energy.

A thermal energy storage system based on the Rotating Drum Heat Exchanger therefore offers advantages over state-of-the-art two-tank molten salt storages in terms of surface-specific heat transfer density, overall storage density, a significant amount of storable energy at the low temperature level of the phase change temperature, and the ability to store the cold storage material in its solid state, preventing unintended solidification in the system. Therefore, compared to the state-of-the-art, significant benefits regarding costs and exergetic efficiency might be achieved. While several components of an industrial-scale storage system are commercially available or can be easily adopted from two-tank molten salt storages, such as the storage tanks and pumps for liquid PCM, further technological research is necessary for an industrial deployment. This includes an proof of concept of evaporation inside the Rotating Drum as well as the development of feasible scraping methods for nitrate salts. The sealing of the Rotating Drum can be adopted from steam or gas turbines.

5 Summary

In the present thesis, the concept of the Rotating Drum Heat Exchanger for the discharge of thermal energy from a phase change material was investigated. Started with fundamental investigations on the heat transfer phenomena during solidification at the Rotating Drum Heat Exchanger, the work results in the description of an industrial-scale thermal energy storage system for the generation of process steam. The investigations started with an experimental test rig for the proof of concept of the Rotating Drum Heat Exchanger, which also served for the experimental measurement of the achievable heat transfer. By doing so, various physical effects affecting the heat transfer were identified. The experimental work is used for the development and validation of a numerical simulation, based on a transient 1-dimensional finite differences scheme. This simulation is used for the description of an industrial-scale latent heat thermal energy storage used for the (co-) generation of process steam. The comprehensive findings of these three main parts of the work in hand can be summarized as follows:

- With the experimental test rig using decanoic acid as PCM and liquid water as HTF, a proof of concept of the Rotating Drum Heat Exchanger could be obtained. Thereby, the solidified PCM was smoothly removed from the surface of the Rotating Drum using a thin metal sheet as scraper.
- With the experimental test rig, a heat transfer of above 1.5 kW could be transferred at a total temperature difference of 20 K on a drum with a drum shell surface of 0.23 m^2, while 24 % of the drums shell was immersed in liquid PCM. This results in an overall heat transfer coefficient of 325 $W \cdot m^{-2} \cdot K^{-1}$ referred to the total drums shell surface.
- The measured heat transfer is highly dependent on the temperature difference between the melting point of the PCM and the temperature of the HTF inside the drum. An additional temperature difference between the melting point of

the PCM and the liquid PCM increases the heat transfer significantly less. Thus, on average, the heat transfer is increased by 31 % when the temperature difference between the melting point of the PCM and the temperature of the HTF is increased by 5 K, while remaining a total temperature difference of 20 K between the HTF and the temperature of the liquid PCM. Compared to a purely convective heat transfer without solidification, the heat transfer in the case of solidification could be increased by 77 % for the same total temperature difference.

- Layer thicknesses of the solidified PCM of less than 0.1 mm were measured. Thereby, liquid PCM adhering to the surface solidifies after the surface has emerged from the liquid PCM. The adhesion has been quantified by comparing measurements with adhesion and measurements with a suitable rubber lip which eliminates the adhesion. An increase in heat transfer of up to 45 % due to the adhesion has been measured. A correlation of Gelperin could be identified, allowing the thickness of the adhering layer to be calculated with an average deviation of 39 %.
- A simplified quasistationary calculation approach for the heat transfer underestimates the measured heat transfer by 33 % on average. In contrast, a developed numerical simulation based on a transient 1-dimensional finite differences scheme reproduces the heat transfer with a deviation of 8 % on average. The numerical simulation is therefore validated for the calculation of the heat transfer of the Rotating Drum Heat Exchanger.
- A hollow drum is not suitable for free scalability since the required wall thickness increases with increasing internal pressure or diameter of the drum. A so-called multiple-channel-drum with several small channels in the drum shell is introduced in order to achieve free scalability up to the MW-range.
- An adoption of the simulation for the calculation of the multiple-channel-drum and the use nitrate salts as storage material shows a high surface-specific heat transfer of more than 300 $KW\cdot m^{-2}$ and an achievable overall heat transfer coefficient of more than 2000 $W\cdot m^{-2}\cdot K^{-1}$. Thereby, the design is freely scalable, in which the thickness of the heat transferring steel wall has the largest influence on the heat transfer.
- With the increased temperature difference of the storage material, the phase change enthalpy as well as the thermal energy storable by a temperature difference within the liquid and the solid phase can be utilized for thermal energy storage. This increases the thermal energy storage density by up to 65 % compared to state-of-the-art two-tank molten salt storages. The utilization of the phase change enables the charging of a considerable amount of energy at a

relatively low temperature level. In addition, the ability to store the storage material in its solid phase prevents unintended solidification.

The Rotating Drum Heat Exchanger developed within the scope of this work as the key-component of a thermal energy storage system is therefore characterized by a high surface-specific heat transfer, predestined for the evaporation of a fluid. A thermal energy storage system based on the Rotating Drum Heat Exchanger is characterized by increased storage density, the ability to charge a significant amount of thermal energy at the temperature of the phase change of the storage material, and the ability to store the cold storage material in the solid state to prevent unwanted solidification. Compared to state-of-the-art two-tank molten salt storages, there is a high potential for benefits in terms of cost and exergetic efficiency.

For the industrial-scale deployment of this technology, further technological progress might be necessary in terms of scraping off the solidified nitrate salts and the rotating bearings.

6 References

[1] IRENA, Renewable Power Generation Costs in 2020, International Renewable Energy Agency, (2021)

[2] IEA, Renewables 2019, IEA, Paris, (2019)

[3] E. Pihl, D. Kushnir, B. Sandén, F. Johnsson, Material constraints for concentrating solar thermal power, Energy, 44 (2012) 944-954 https://doi.org/10.1016/j.energy.2012.04.057

[4] A.C. Schomberg, S. Bringezu, M. Flörke, Extended life cycle assessment reveals the spatially-explicit water scarcity footprint of a lithium-ion battery storage, Commun. Earth Environ., 2 (2021) https://doi.org/10.1038/s43247-020-00080-9

[5] J. Sadhukhan, M. Christensen, An In-Depth Life Cycle Assessment (LCA) of Lithium-Ion Battery for Climate Impact Mitigation Strategies, Energies, 14 (2021) https:/doi.org/10.3390/en14175555

[6] T. Bauer, C. Odenthal, A. Bonk, Molten Salt Storage for Power Generation, Chem. Ing. Tech., 93 (2021) 534-546 https://doi.org/10.1002/cite.202000137

[7] J.G. Cordaro, N.C. Rubin, R.W. Bradshaw, Multicomponent Molten Salt Mixtures Based on Nitrate/Nitrite Anions, J. Sol. Energy, 133 (2011) https://doi.org/10.1115/1.4003418

[8] V.A. Sötz, A. Bonk, T. Bauer, With a view to elevated operating temperatures in thermal energy storage - Reaction chemistry of Solar Salt up to 630°C, Sol. Energy Mater. Sol. Cells, 212 (2020) https://doi.org/10.1016/j.solmat.2020.110577

[9] V.A. Sötz, A. Bonk, J. Steinbrecher, T. Bauer, Defined purge gas composition stabilizes molten nitrate salt - Experimental prove and thermodynamic calculations, Sol. Energy, 211 (2020) 453-462 https://doi.org/10.1016/j.solener.2020.09.041

[10] V.M.B. Nunes, M.J.V. Lourenço, F.J.V. Santos, C.A. Nieto de Castro, Molten alkali carbonates as alternative engineering fluids for high temperature applications, App. Energy, 242 (2019) 1626-1633 https://doi.org/10.1016/j.apenergy.2019.03.190

[11] Y. Zhao, J. Vidal, Potential scalability of a cost-effective purification method for MgCl2-Containing salts for next-generation concentrating solar power technologies, Sol. Energy Mater. Sol. Cells, 215 (2020) https://doi.org/10.1016/j.solmat.2020.110663

[12] C. Odenthal, F. Klasing, P. Knödler, S. Zunft, T. Bauer, Experimental and numerical investigation of a 4 MWh high temperature molten salt thermocline storage system with filler, in: SOLARPACES 2019: International Conference on Concentrating Solar Power and Chemical Energy Systems, 2020.

[13] W. Lou, L. Luo, Y. Hua, Y. Fan, Z. Du, A Review on the Performance Indicators and Influencing Factors for the Thermocline Thermal Energy Storage Systems, Energies, 14 (2021) https://doi.org/10.3390/en14248384

[14] J.M. Gordon, T. Fasquelle, E. Nadal, A. Vossier, Providing large-scale electricity demand with photovoltaics and molten-salt storage, Renew. Sust. Energ. Rev., 135 (2021) https://doi.org/10.1016/j.rser.2020.110261

[15] F. Trieb, A. Thess, Storage plants – a solution to the residual load challenge of the power sector?, J. Energy Storage, 31 (2020) https://doi.org/10.1016/j.est.2020.101626

[16] H. Nazir, M. Batool, F.J. Bolivar Osorio, M. Isaza-Ruiz, X. Xu, K. Vignarooban, P. Phelan, Inamuddin, A.M. Kannan, Recent developments in phase change materials for energy storage applications: A review, Int. J. Heat Mass Transf., 129 (2019) 491-523 https://doi.org/10.1016/j.ijheatmasstransfer.2018.09.126

[17] T. Bauer, D. Laing, R. Tamme, Overview of PCMs for Concentrated Solar Power in the Temperature Range 200 to 350°C, AST, 74 (2010) 272-277 https://doi.org/10.4028/www.scientific.net/AST.74.272

[18] T. Bauer, D. Laing, R. Tamme, Characterization of Sodium Nitrate as Phase Change Material, Int. J. Thermophys., 33 (2012) 91-104 https://doi.org/10.1007/s10765-011-1113-9

[19] L.F. Cabeza, A. Castell, C. Barreneche, A. de Gracia, A.I. Fernández, Materials used as PCM in thermal energy storage in buildings: A review, Renew. Sust. Energ. Rev., 15 (2011) 1675-1695 https://doi.org/10.1016/j.rser.2010.11.018

[20] S.R.L. da Cunha, J.L.B. de Aguiar, Phase change materials and energy efficiency of buildings: A review of knowledge, J. Energy Storage, 27 (2020) https://doi.org/10.1016/j.est.2019.101083

[21] D. Laing, C. Bahl, T. Bauer, D. Lehmann, W.-D. Steinmann, Thermal energy storage for direct steam generation, Sol. Energy, 85 (2011) 627-633 https://doi.org/10.1016/j.solener.2010.08.015

[22] W.-D. Steinmann, D. Laing, R. Tamme, Development of PCM Storage for Process Heat and Power Generation, J. Sol. Energy Eng., 131 (2009) https://doi.org/10.1115/1.3197834

[23] A. Crespo, C. Barreneche, M. Ibarra, W. Platzer, Latent thermal energy storage for solar process heat applications at medium-high temperatures – A review, Sol. Energy, 192 (2019) 3-34 https://doi.org/10.1016/j.solener.2018.06.101

[24] M. Johnson, J. Vogel, M. Hempel, A. Dengel, M. Seitz, B. Hachmann, High Temperature Latent Heat Thermal Energy Storage Integration in a Co-gen Plant, Energy Procedia, 73 (2015) 281-288 https://doi.org/10.1016/j.egypro.2015.07.689

[25] R. Elarem, T. Alqahtani, S. Mellouli, F. Askri, A. Edacherian, T. Vineet, I.A. Badruddin, J. Abdelmajid, A comprehensive review of heat transfer intensification methods for latent heat storage units, Energy Storage, 3 (2020) https://doi.org/10.1002/est2.127

[26] Y.B. Tao, Y.-L. He, A review of phase change material and performance enhancement method for latent heat storage system, 93 (2018) 245-259 https://doi.org/10.1016/j.rser.2018.05.028

[27] M.A. Kibria, M.R. Anisur, M.H. Mahfuz, R. Saidur, I.H.S.C. Metselaar, A review on thermophysical properties of nanoparticle dispersed phase change materials, Energy Convers. Manag., 95 (2015) 69-89 https://doi.org/10.1016/j.enconman.2015.02.028

[28] S.L. Tariq, H.M. Ali, M.A. Akram, M.M. Janjua, M. Ahmadlouydarab, Nanoparticles enhanced phase change materials (NePCMs)-A recent review, Appl. Therm. Eng., 176 (2020) https://doi.org/10.1016/j.applthermaleng.2020.115305

[29] X. Huang, C. Zhu, Y. Lin, G. Fang, Thermal properties and applications of microencapsulated PCM for thermal energy storage: A review, Appl. Therm. Eng., 147 (2019) 841-855 https://doi.org/10.1016/j.applthermaleng.2018.11.007

[30] J. Giro-Paloma, M. Martínez, L.F. Cabeza, A.I. Fernández, Types, methods, techniques, and applications for microencapsulated phase change materials (MPCM): A review, Renew. Sust. Energ. Rev. , 53 (2016) 1059-1075 https://doi.org/10.1016/j.rser.2015.09.040

[31] Y. Jiang, M. Liu, Y. Sun, Review on the development of high temperature phase change material composites for solar thermal energy storage, Sol. Energy Mater Sol. Cells, 203 (2019) https://doi.org/10.1016/j.solmat.2019.110164

[32] Z. Liu, Z. Yu, T. Yang, D. Qin, S. Li, G. Zhang, F. Haghighat, M.M. Joybari, A review on macro-encapsulated phase change material for building envelope applications, Build. Environ., 144 (2018) 281-294 https://doi.org/10.1016/j.buildenv.2018.08.030

[33] S. Hohlein, A. Konig-Haagen, D. Bruggemann, Macro-Encapsulation of Inorganic Phase-Change Materials (PCM) in Metal Capsules, Materials (Basel), 11 (2018) https://doi.org/10.3390/ma11091752

[34] A. Raul, M. Jain, S. Gaikwad, S.K. Saha, Modelling and experimental study of latent heat thermal energy storage with encapsulated PCMs for solar thermal applications, Appl. Therm. Eng., 143 (2018) 415-428 https://doi.org/10.1016/j.applthermaleng.2018.07.123

[35] C. Prieto, C. Rubio, L.F. Cabeza, New phase change material storage concept including metal wool as heat transfer enhancement method for solar heat use in industry, J. Energy Storage, 33 (2021) https://doi.org/10.1016/j.est.2020.101926

[36] J. Lei, Y. Tian, D. Zhou, W. Ye, Y. Huang, Y. Zhang, Heat transfer enhancement in latent heat thermal energy storage using copper foams with varying porosity, Solar Energy, 221 (2021) 75-86 https://doi.org/10.1016/j.solener.2021.04.013

[37] M. Johnson, J. Vogel, M. Hempel, B. Hachmann, A. Dengel, Design of high temperature thermal energy storage for high power levels, Sustain. Cities Soc., 35 (2017) 758-763 https://doi.org/10.1016/j.scs.2017.09.007

[38] M. Eslami, F. Khosravi, H.R. Fallah Kohan, Effects of fin parameters on performance of latent heat thermal energy storage systems: A comprehensive review, Sustain. Energy Technol. Assess., 47 (2021) https://doi.org/10.1016/j.seta.2021.101449

[39] M. Johnson, B. Hachmann, A.J. Dengel, M. Fiß, M. Hempel, D. Bauer, Design and Integration of High Temperature Latent Heat Thermal Energy Storage for High Power Levels, in: ASME IMECE Pittsburgh, PA, USA, 2018.

[40] P. Zhang, Z.W. Ma, R.Z. Wang, An overview of phase change material slurries: MPCS and CHS, Renew. Sust. Energy Rev., 14 (2010) 598-614 https://doi.org/10.1016/j.rser.2009.08.015

[41] Z. Qiu, X. Ma, P. Li, X. Zhao, A. Wright, Micro-encapsulated phase change material (MPCM) slurries: Characterization and building applications, Renew. Sust. Energ. Rev., 77 (2017) 246-262 https://doi.org/10.1016/j.rser.2017.04.001

[42] S. Niedermaier, M. Biedenbach, S. Gschwander, Characterisation and Enhancement of Phase Change Slurries, Energy Procedia, 99 (2016) 64-71 https://doi.org/10.1016/j.egypro.2016.10.098

[43] P. O'Neill, L. Fischer, R. Revellin, J. Bonjour, Phase change dispersions: A literature review on their thermo-rheological performance for cooling applications, Appl. Therm. Eng., 192 (2021) https://doi.org/10.1016/j.applthermaleng.2021.116920

[44] H. Pointner, W.-D. Steinmann, Experimental demonstration of an active latent heat storage concept, Appl. Energy, 168 (2016) 661-671 https://doi.org/10.1016/j.apenergy.2016.01.113

[45] W.-D. Steinmann, R. Tamme, Latent Heat Storage for Solar Steam Systems, J. Sol. Energy Eng., 130 (2008) https://doi.org/10.1115/1.2804624

[46] L. Hegner, S. Krimmel, R. Ravotti, D. Festini, J. Worlitschek, A. Stamatiou, Experimental Feasibility Study of a Direct Contact Latent Heat Storage Using an Ester as a Bio-Based Storage Material, Energies, 14 (2021) https://doi.org/10.3390/en14020511

[47] T. Nomura, M. Tsubota, T. Oya, N. Okinaka, T. Akiyama, Heat release performance of direct-contact heat exchanger with erythritol as phase change material, Appl. Therm. Eng., 61 (2013) 28-35 https://doi.org/10.1016/j.applthermaleng.2013.07.024

[48] R.T. Lefrois, G.R. Knowles, A.K. Mathur, J. Budimir, Active heat exchange system development for latent heat thermal energy storage, Honeywell, Inc., (1979)

[49] J. Alario, R. Kosson, R. Haslett, Active heat exchange system development for latent heat thermal energy storage, Grumman Aerospace Corp., (1980)

[50] V. Zipf, A. Neuhäuser, D. Willert, P. Nitz, S. Gschwander, W. Platzer, High temperature latent heat storage with a screw heat exchanger: Design of prototype, Appl. Energy, 109 (2013) 462-469 https://doi.org/10.1016/j.apenergy.2012.11.044

[51] U. Nepustil, D. Laing-Nepustil, D. Lodemann, R. Sivabalan, V. Hausmann, High Temperature Latent Heat Storage with Direct Electrical Charging – Second Generation Design, Energy Procedia, 99 (2016) 314-320 https://doi.org/10.1016/j.egypro.2016.10.121

[52] N. Maruoka, T. Tsutsumi, A. Ito, M. Hayasaka, H. Nogami, Heat release characteristics of a latent heat storage heat exchanger by scraping the solidified phase change material layer, Energy, 205 (2020) https://doi.org/10.1016/j.energy.2020.118055

[53] A. Egea, A. García, R. Herrero-Martín, J. Pérez-García, Preliminary thermal characterisation of an active latent thermal energy storage system using PCM, J. Phys. Conf. Ser., 2116 (2021) https://doi.org/10.1088/1742-6596/2116/1/012045

[54] O. Dumont, G.F. Frate, A. Pillai, S. Lecompte, M. De paepe, V. Lemort, Carnot battery technology: A state-of-the-art review, J. Energy Storage, 32 (2020) https://doi.org/10.1016/j.est.2020.101756

[55] R.B. Laughlin, Pumped thermal grid storage with heat exchange, J. Renew. Sustain. Energy, 9 (2017) https://doi.org/10.1063/1.4994054

[56] T. Desrues, J. Ruer, P. Marty, J.F. Fourmigué, A thermal energy storage process for large scale electric applications, Appl. Therm. Eng., 30 (2010) 425-432 https://doi.org/10.1016/j.applthermaleng.2009.10.002

[57] H. Jockenhöfer, W.-D. Steinmann, D. Bauer, Detailed numerical investigation of a pumped thermal energy storage with low temperature heat integration, Energy, 145 (2018) 665-676 https://doi.org/10.1016/j.energy.2017.12.087

[58] G.F. Frate, L. Ferrari, U. Desideri, Rankine Carnot Batteries with the Integration of Thermal Energy Sources: A Review, Energies, 13 (2020) https://doi.org/10.3390/en13184766

[59] M. Mercangöz, J. Hemrle, L. Kaufmann, A. Z'Graggen, C. Ohler, Electrothermal energy storage with transcritical CO 2 cycles, Energy, 45 (2012) 407-415 https://doi.org/10.1016/j.energy.2012.03.013

[60] Y.-M. Kim, D.-G. Shin, S.-Y. Lee, D. Favrat, Isothermal transcritical CO2 cycles with TES (thermal energy storage) for electricity storage, Energy, 49 (2013) 484-501 https://doi.org/10.1016/j.energy.2012.09.057

[61] W.D. Steinmann, The CHEST (Compressed Heat Energy STorage) concept for facility scale thermo mechanical energy storage, Energy, 69 (2014) 543-552 https://doi.org/10.1016/j.energy.2014.03.049
[62] W.-D. Steinmann, D. Bauer, H. Jockenhöfer, M. Johnson, Pumped thermal energy storage (PTES) as smart sector-coupling technology for heat and electricity, Energy, 183 (2019) 185-190 https://doi.org/10.1016/j.energy.2019.06.058
[63] B. Eppinger, L. Zigan, J. Karl, S. Will, Pumped thermal energy storage with heat pump-ORC-systems: Comparison of latent and sensible thermal storages for various fluids, Appl. Energy, 280 (2020) https://doi.org/10.1016/j.apenergy.2020.115940
[64] W.-D. Steinmann, H. Jockenhöfer, D. Bauer, Thermodynamic Analysis of High-Temperature Carnot Battery Concepts, Energy Techn., 8 (2019) https://doi.org/10.1002/ente.201900895
[65] P. Albertus, J.S. Manser, S. Litzelman, Long-Duration Electricity Storage Applications, Economics, and Technologies, Joule, 4 (2020) 21-32 https://doi.org/10.1016/j.joule.2019.11.009
[66] T.R. Davenne, B.M. Peters, An Analysis of Pumped Thermal Energy Storage With De-coupled Thermal Stores, Front. Energy Res., 8 (2020) https://doi.org/10.3389/fenrg.2020.00160
[67] V. Novotny, V. Basta, P. Smola, J. Spale, Review of Carnot Battery Technology Commercial Development, Energies, 15 (2022) https://doi.org/10.3390/en15020647
[68] F.I.e. al., Heat Roadmap Europe 4 (HRE4) (2017)
[69] F.I.f.S.a.I.R.I.e. al., Mapping and analyses of the current and future (2020 - 2030) heating/cooling fuel deployment (fossil/renewables, (2016)
[70] T. Naegler, S. Simon, M. Klein, H.C. Gils, Quantification of the European industrial heat demand by branch and temperature level, Int. J. Energ. Res., 39 (2015) 2019-2030 https://doi.org/10.1002/er.3436
[71] M. Rehfeldt, T. Fleiter, F. Toro, A bottom-up estimation of the heating and cooling demand in European industry, Energy Effic., 11 (2017) 1057-1082 https://doi.org/10.1007/s12053-017-9571-y
[72] EUROSTAT Database, in, 2021.
[73] P. Gentili, C. Landini, S. D'Ovidio, E. Lusardi, C. Rohde, A. Aydemir, S. Hirzel, B. Ostrander, S. Karellas, K. Braimakis, Ecodesign Preparatory Study on Steam Boilers (ENTR Lot 7), PricewaterhouseCoopers EEIG's consortium; Fraunhofer ISI; ICCS-NTUA (2014)
[74] A.A. Solomon, M. Child, U. Caldera, C. Breyer, How much energy storage is needed to incorporate very large intermittent renewables?, Energy Procedia, 135 (2017) 283-293 https://doi.org/10.1016/j.egypro.2017.09.520
[75] M.S. Ziegler, J.M. Mueller, G.D. Pereira, J. Song, M. Ferrara, Y.-M. Chiang, J.E. Trancik, Storage Requirements and Costs of Shaping Renewable Energy Toward Grid Decarbonization, Joule, 3 (2019) 2134-2153 https://doi.org/10.1016/j.joule.2019.06.012
[76] N. Langweg, Entwurf und Aufbau eines experimentellen Latentwärmespeichers mit bewegtem Speichermaterial, Bachelor Thesis, Hochschule Niederrhein, 2017
[77] W. Roetzel, B. Spang, C3 Typical Values of Overall Heat Transfer Coefficients, in: VDI e.V. (Eds.), VDI Heat Atlas, Springer, Berlin, Heidelberg, 2010, https://doi.org/10.1007/978-3-540-77877-6_6

[78] N.I. Gel'perin, G.A. Nosov, A.V. Makotkin, Determinating the thickness of liquid film holdup on a rotating drum surface, Chem. Pet. Eng., 11 (1975) 230-233 https://doi.org/10.1007/BF01146631

[79] F.K. Tsou, E.M. Sparrow, R.J. Goldstein, Flow and heat transfer in the boundary layer on a continuous moving surface, Int. J. Heat Mass Transf., 10 (1967) 219-235 https://doi.org/10.1016/0017-9310(67)90100-7

[80] K. Gauler, Wärme- und Stoffübertragung an eine mitbewegte Grenzfläche bei Grenzschichtströmung, Dissertation, Universitaet Karlsruhe, 1972